

Mixing in High Schmidt Number Turbulent Jets

Thesis by
Paul Lewis Miller

In Partial Fulfillment of the Requirements
for the Degree of
Doctor of Philosophy

California Institute of Technology
Pasadena, California

1991

(submitted April 25, 1991)

©1991

Paul Lewis Miller

All rights reserved

Acknowledgements

I wish to acknowledge the following people for their assistance and/or support during the time I have been at Caltech and GALCIT. First and foremost, I thank my advisor, Paul Dimotakis, for his encouragement throughout my graduate studies, and for many suggestions and contributions to this work. His scientific understanding and his personal character have made an indelible impression upon me. In collaboration with Paul, Dan Lang is responsible for a large number of accomplishments while at GALCIT that have greatly facilitated and improved this thesis. These include, among others, development of the HYDRA computer system and libraries, data acquisition support, and electronic design. His efforts have been a tremendous help. I give special thanks to Gene Broadwell, whose ideas concerning turbulent mixing have had a strong influence on this thesis. His friendship over the past several years is especially appreciated.

Several of my fellow students have contributed help. In particular I'd like to thank Cliff Frieler, who is always interested in a problem, usually has a solution, and never refuses a request for assistance, and Dave Dowling, for assistance at the onset of the experiments and the indirect influence of his impressive thesis.

Many staff members at GALCIT provided important contributions in the course of this work. Herb Gaebler offered assistance with a number of mechanical matters, Harry Hamaguchi produced the photographs of the facility and conducted the difficult printing of the jet growth-rate pictures, Pavel Svitek aided in construction of the Phase II improvements and with the jet calibration, and Phil

Wood created a piece of art with his machining of the new nozzle. Also, Earl Dahl helped on numerous occasions, and Jean Anderson and Pat Gladson offered library assistance. All of them also provided a great deal of encouragement.

Finally, I thank the following individuals: Dan Nosenchuck, for steering me toward Caltech; Larry Sverdrup, for introducing me to climbing; Annie, for her support over the years, particularly during first year, for many climbing adventures, and for taking care of me when I broke my foot; Rick, an exceptional friend, for discussions and help with my work, but more importantly, for his work on The Wall and our exploits on the rocks, such as Whodunit, Valhalla, Illusion Dweller, and Figures on a Landscape; my roommate, Jay, who has shown remarkable patience and consideration; and Lara, for her encouragement and understanding during the final phase of this work.

This work was jointly funded by the Gas Research Institute, through Contracts No. 5083-260-0878 and 5087-260-1467, and the Air Force Office of Scientific Research, through Grants No. 83-0213 and 88-0155. Additional personal financial support was provided by the California Institute of Technology. All are greatly appreciated.

Abstract

This thesis is an experimental investigation of the passive scalar (species concentration) field in the far-field of round, axisymmetric, high Schmidt number (liquid phase), turbulent jets issuing into a quiescent reservoir, by means of a quantitative laser-induced fluorescence technique. Single-point concentration measurements are made on the jet centerline, at axial locations from 100 to 305 nozzle diameters downstream, and Reynolds numbers of 3,000 to 102,000, yielding data with a resolved temporal dynamic range up to 2.5×10^5 , and capturing as many as 504 large-scale structure passages. Long-time statistics of the jet concentration are found to converge slowly. Between 100 and 300 large-scale structure passages are required to reduce the uncertainty in the mean to 1%, or so. The behavior of the jet varies with Reynolds number. The centerline concentration pdf's become taller and narrower with increasing Re , and the normalized concentration variances correspondingly decrease with Re . The concentration power spectra also evolve with Re . The behavior of the spectral slopes is examined. No constant -1 (Batchelor) spectral slope range is present. Rather, in the viscous region, the power spectra exhibit log-normal behavior, over a range of scales exceeding a factor of 40, in some cases. The frequency of the beginning of this log-normal range scales like $Re^{3/4}$ (Kolmogorov scaling). Mixing in the far-field is found to be susceptible to initial conditions. Disturbances in the jet plenum fluid and near the nozzle exit strongly influence the scalar variance, with larger disturbances causing larger variances, i.e., less homogeneous mixing. The plenum/nozzle geometry also influences the variance. These effects of initial conditions persist for hundreds of diameters from the nozzle

exit, over hundreds of large scales. Mixing in these jets differs from gas-phase, order unity Sc , jet mixing. At low to moderate Re , the higher Sc jet is less well mixed. The difference is less pronounced at higher Re . Flame length estimates imply either an increase in entrainment and/or an increase in molecular mixing, with increasing Re . Experimental considerations such as buoyancy and resolution are shown not to influence these results.

Table of contents

Copyright	ii
Acknowledgements	iii
Abstract	v
List of symbols	x
1.0 Introduction	1
1.1 Background	1
1.2 The current work	3
2.0 Experimental facility	6
2.1 Single-point measurements – Phase I	6
2.2 Single-point measurements – Phase II	10
3.0 Structure and statistics of the scalar field	15
3.1 Time traces of the concentration	16
3.2 Histograms of jet concentration	20
3.3 Behavior of the mean	27
3.4 Variance of the concentration	31
3.5 Model of large-scale structures	33
4.0 Reynolds number effects	38
4.1 Microscales and resolution	39
4.2 Behavior of the concentration pdf's	40

4.3	Scalar variance results	43
4.4	Concentration power spectra	45
5.0	Spectral slopes	50
5.1	Average slopes	51
5.2	Spectral slope behavior	54
5.3	The log-normal range and the break-point	58
5.4	The roll-off	61
6.0	The influence of disturbances	62
6.1	The scalar variance, revisited	62
6.2	Plenum/nozzle geometry	66
7.0	Discussion of Schmidt number effects	69
7.1	Scalar pdf's	70
7.2	Scalar variance	71
7.3	Power spectra	72
8.0	Estimation of flame lengths	74
8.1	Estimation method	74
8.2	Results	77
8.3	Comparison with other investigations	79
9.0	Conclusions	82
A.0	Description of flow parameters	85
A.1	Velocities and large scales	85
A.2	Buoyancy length scale	87

A.3	Attenuation considerations	89
A.4	Run parameters	91
B.0	Experimental considerations, data acquisition, and processing	95
B.1	Run preparations	95
B.2	Tank conditions	96
B.3	The laser diagnostic	98
B.4	Jet alignment	100
B.5	Signal background	101
B.6	Reynolds number calibration	102
B.7	Jet start-up	103
B.8	Signal acquisition	105
B.9	A/D converter calibration	106
B.10	Noise and Wiener filtering	106
B.11	Power spectral density estimation.....	108
C.0	Microscales and resolution	109
C.1	Description of microscales	110
C.2	Resolution	112
C.3	The extent of resolution's influence	116
C.4	A comment upon the continuum approximation	117
D.0	Jet growth rate pictures	119
	References	124

List of Symbols

English alphabet

A	half the peak-to-peak amplitude of ramp model (Chapter 3)
A	additive parameter in fits of the variance behavior with Re
B	multiplicative parameter in fits of the variance behavior with Re
c	local concentration
$c(t)$	concentration at time t
\bar{c}	local mean value of the concentration
c'	concentration rms
$c'(t)$	fluctuating component of the local concentration ($c - \bar{c}$)
$\overline{c'^2}$	concentration (scalar) variance
c_{\max}	maximum realized concentration in a pdf
c_s	stoichiometric composition (jet fluid fraction)
c_{turn}	concentration value at a local extremum of $c(t)$
c_ϵ	concentration limit for a given ϵ (Eq. 8.6)
d	jet nozzle exit diameter
d^*	jet momentum diameter
D	scalar species diffusivity
E	(fully resolved) power spectral density
E_c	concentration power spectral density
E_{meas}	(resolution limited) measured power spectral density
f	frequency
$f(c/\bar{c})$	similarity function of jet axis concentration pdf
$f\#$	f-number

g	gravitational acceleration
$H(\omega)$	transfer function
$H_1(\omega)$	transfer function for a single pole filter at τ_1
$H_2(\omega)$	transfer function for a single pole filter at τ_2
I	Phase I conditions (see Chapter 2)
I	laser intensity (Fig. B.1)
I_0	reference laser intensity (Fig. B.1)
II	Phase II conditions (see Chapter 2)
IIa	Phase IIa conditions (see Chapter 2)
IIb	Phase IIb conditions (see Chapter 2)
k	wavenumber
k_ν	viscous-scale wavenumber
L_b	buoyancy length (Eq. A.4)
L_f	flame length
N	number of trials (Eq. 3.1)
p	exponent in fits of the variance behavior with Re
p	probability of a binomial event (Eq. 3.1)
$p(c)$	probability density
$p(t)$	pressure in the plenum
$p(c, x)$	pdf on the jet axis
p_0	reference pressure (maximum attained during a run) in the plenum
Pr	Prandtl number ($\equiv \nu/\kappa$)
q	complementary probability of a binomial event ($\equiv 1 - p$)
$R_{c'c'}$	autocorrelation function of c'
Re	Reynolds number (Eq. 1.2)
Re_λ	local-scale Reynolds number (Eq. C.2)
Re_T	Taylor-scale Reynolds number (Eq. C.11)

Sc	Schmidt number (Eq. 1.1)
t	time
T	time period
u_0	calibrated jet nozzle exit velocity
u_{cl}	calculated mean jet centerline velocity (Eq. A.2)
u_λ	local-scale velocity
u'_1	rms of one component of the velocity vector
$var\{w'(T)\}$	variance of $w'(T)$
$w'(T)$	auxiliary process defined by Eq. 3.2
x	axial location in cylindrical coordinates, measured from jet nozzle exit
x_0	jet growth-rate virtual origin

Greek alphabet

α	visual jet full angle
δ	characteristic large scale
$\delta(x)$	local jet width (Eq. D.1)
$\Delta\rho/\rho$	fractional change in the density
ΔU	characteristic large-scale velocity difference
ϵ	a small nondimensional constant
ε	total mean kinetic energy dissipation rate
κ	mean concentration decay constant; thermal diffusivity
λ	local scale
λ_B	Batchelor scale (Eq. C.7)
λ_D	scalar diffusion scale (Eq. C.8)
λ_K	Kolmogorov scale (Eq. C.5)
λ_ν	viscous scale (Eq. C.6)

λ_T	Taylor scale (Eqs. C.9 and C.10)
ν	kinematic viscosity
ν_∞	reservoir fluid kinematic viscosity
π	3.14159...
ρ_j	jet fluid density
ρ_∞	reservoir fluid density
σ	standard deviation
σ_n	standard deviation for binomial process (Eq. 3.1)
$\sigma_{w'}^2(T)$	variance of $w'(T)$ (Eq. 3.3)
τ	dummy time integration variable (Eq. 3.3); passage time
τ_δ	characteristic large-scale passage time
τ_1	location of first filter pole (Eq. C.14)
τ_2	location of second filter pole (Eq. C.14)
ϕ	stoichiometric mixture ratio (equivalence ratio)
ω	circular frequency

Other Symbols

$\langle \rangle$	ensemble average
$\overline{(\)}$	time average

CHAPTER 1

Introduction

1.1 Background

This thesis investigates aspects of passive scalar (species concentration) mixing in high Schmidt number, round, axisymmetric, momentum-dominated, turbulent jets discharging into a quiescent reservoir. Of paramount interest at the outset of this work was the role of the Schmidt number,

$$Sc \equiv \nu/\mathcal{D}, \quad (1.1)$$

where ν is the kinematic viscosity of the fluid and \mathcal{D} is the molecular diffusivity of the scalar species under examination, in the mixing process. This ratio is a measure of the relative influences of the diffusion of momentum and the diffusion of species in a mixing fluid, and is analogous to the Prandtl number $Pr \equiv \nu/\kappa$, where κ , the thermal diffusion coefficient, replaces \mathcal{D} . For example, the diffusion of heat in mercury occurs much faster than the diffusion of momentum, and is a low Schmidt (Prandtl) number fluid, while the diffusion of dye in water is slower than momentum, and is an example of a high Sc fluid. For most gases, the two coefficients are approximately equal, and $Sc \sim 1$.

There is experimental evidence that the Schmidt number influences scalar mixing in turbulent flows. In particular, Koochesfahani & Dimotakis (1986) found that the product formation in a liquid shear layer was half that of gas-phase shear layers (Mungal & Dimotakis 1984) at comparable Reynolds numbers. In turbulent jets, the studies of Kristmanson & Danckwerts (1961) and Wilson & Danckwerts (1964) suggested that the “plume length,” or distance required to dilute the jet to a particular concentration, increased with Sc . Similar results are apparent in the comparison of work by Dahm (1985) and Dowling (1988) (cf. Dowling, Sec. 5.4). In conjunction with the experimental evidence, it is clear theoretically that a decrease in the mixing rate is expected with an increase in the Schmidt number. True molecular *mixing* consists of intermingling the constituents on a molecular scale, as required for chemical reactions for example. This is in contrast to pure *stirring*, in which the interfacial surface area between two or more species is increased, while not actually mixing any of them. Since the scales required to molecularly mix two fluids (i.e., typical molecular separation distances) are very much smaller than the fluid dynamical scales of most flows of interest, diffusion is necessary to mix on the smallest scales. Therefore, the mixing rate depends ultimately upon the species diffusion coefficient, i.e., Sc . For $Sc \rightarrow \infty$, the mixing rate goes to zero, with implications for the behavior of a scalar in the jet (cf. Dimotakis & Miller 1990). These considerations have led to the development of scalar mixing models that account for the influence of the Schmidt number (e.g., Broadwell & Breidenthal 1982, Broadwell 1987, and Dimotakis 1987).

In addition to the Schmidt number, another important parameter is the jet Reynolds number, defined here as

$$Re \equiv \frac{u_0 d}{\nu}, \quad (1.2)$$

where u_0 is the jet velocity at the nozzle exit and d is the nozzle diameter. The im-

pact of the Reynolds number on jet mixing has usually been considered small. While Ricou & Spalding (1961) found changes in jet entrainment rates up to Reynolds numbers of 25,000, Kristmanson & Danckwerts (1961) and Wilson & Danckwerts (1964) reported little Reynolds-number effect on mixing above $Re = 6,500$, and Weddell (in Hottel, 1953) and Dahm & Dimotakis (1990) found little change in the jet “flame lengths,” which may be interpreted as the mixing rate (Broadwell 1982), at Reynolds numbers in excess of about 3,000. Some of the best gas-phase jet concentration data available, which fully resolved the smallest scales of interest in the jet flow, were reported by Dowling & Dimotakis (1990). Their data demonstrated very little, if any, dependence of the jet variance (for example) on Re .

1.2 The current work

The present investigation complements previous work on turbulent jet mixing in several ways. The large Schmidt number sets it apart from gas-phase, order-unity Schmidt number experiments, and the range of variation of the Reynolds number has apparently not previously been explored in a single set of experiments (in which *resolved* concentration measurements were conducted). These measurements have been made in the far-field of the jet, at locations one hundred nozzle diameters or more downstream. Few previous investigations have been carried out so far from the nozzle. The present jets have negligible buoyancy, in contrast to several reported studies of buoyant plumes, and the length of the acquired data records has typically been between one and eight million points per run, providing a wide dynamic range in record length that permits small-scale features to be examined while attaining sufficient large-scale statistics. Efforts made to maximize spatial resolution, combined with the far-field measurement location (which makes the absolute sizes of the fluid-dynamical scales larger), the relatively high signal-to-noise ratio (SNR) of the

data acquisition, and the treatment of noise using Wiener-filter techniques, have resulted in some of the highest resolution concentration measurements collected from a high Schmidt number jet.

This thesis addresses a variety of issues concerning the jet fluid scalar behavior. Chapter 2 begins by describing the experimental apparatus and the several sets of experiments conducted. Chapter 3 investigates the temporal behavior of the jet concentration traces and the statistical convergence of the concentration pdf's, mean, and variance. The concentration pdf's, variance, and power spectra are then explored in some detail in Chapter 4 for Reynolds number effects. The analysis of the power spectra is continued in Chapter 5 and the power spectra slopes are examined. The influence of initial conditions on the far-field mixing behavior in the jet is investigated in Chapter 6. Chapter 7 compares the present results with previous gas-phase (order unity Sc) work, and Chapter 8 examines the behavior of flame lengths estimated from the current data. Conclusions are presented in Chapter 9.

Finally, several previous reports in the literature should be mentioned which utilized the Phase I measurements conducted in the course of this work. The scalar interface was examined for fractal behavior in Miller & Dimotakis (1991a). It was determined that the iso-scalar surfaces, over the entire range of concentrations, is *not* described by a constant fractal dimension. Rather, a simple stochastic log-normal model of the interface crossings was found to agree well with the experimental results. Reynolds number effects on the mixing behavior of these jets were investigated in Miller & Dimotakis (1991b). Many of the results of Chapter 4 first appeared there, but for a more restricted set of data. Lastly, Dimotakis & Miller (1990) addressed ramifications of the boundedness of scalar fluctuations. In particular, theoretical difficulties were raised with the proposed Batchelor (1959) spectrum

for high Schmidt number turbulence. The new finding of a log-normal range in the spectral slope at the viscous scales, presented in Chapter 5, should be viewed in the context of that previous discussion.

CHAPTER 2

Experimental facility

All experiments discussed in this thesis utilized a jet flow facility in the sub-basement of the Guggenheim Aeronautical Laboratory at Caltech, designed by Garry Brown in collaboration with Paul Dimotakis. The major components of this apparatus consist of a large water tank with windows (which acts as the jet reservoir), a jet plenum and nozzle assembly, plumbing and controls to establish the jet flow, and a large discharge tank into which the reservoir water is emptied. Much of this has been extensively documented elsewhere (cf. Dimotakis et al. 1983, Dahm 1985, and Miller & Dimotakis 1991a,b). This chapter will describe the physical apparatus used to acquire the data in this thesis, including a second set of experiments (Phase II) for which a new jet nozzle, plenum, and flow delivery system were designed and installed. For a description of the flow parameters, such as the jet velocities, *etc.*, see Appendix A. Additional experimental details are discussed in Appendix B. The issue of resolution is addressed in Appendix C. A set-up for shadowgraphy is described in Appendix D, and a sample jet growth rate picture is included.

2.1 Single-point measurements – Phase I

Fig. 2.1 is a schematic of the experimental apparatus used to conduct the first series (Phase I) of high resolution single-point measurements of the jet scalar (concentration) field.

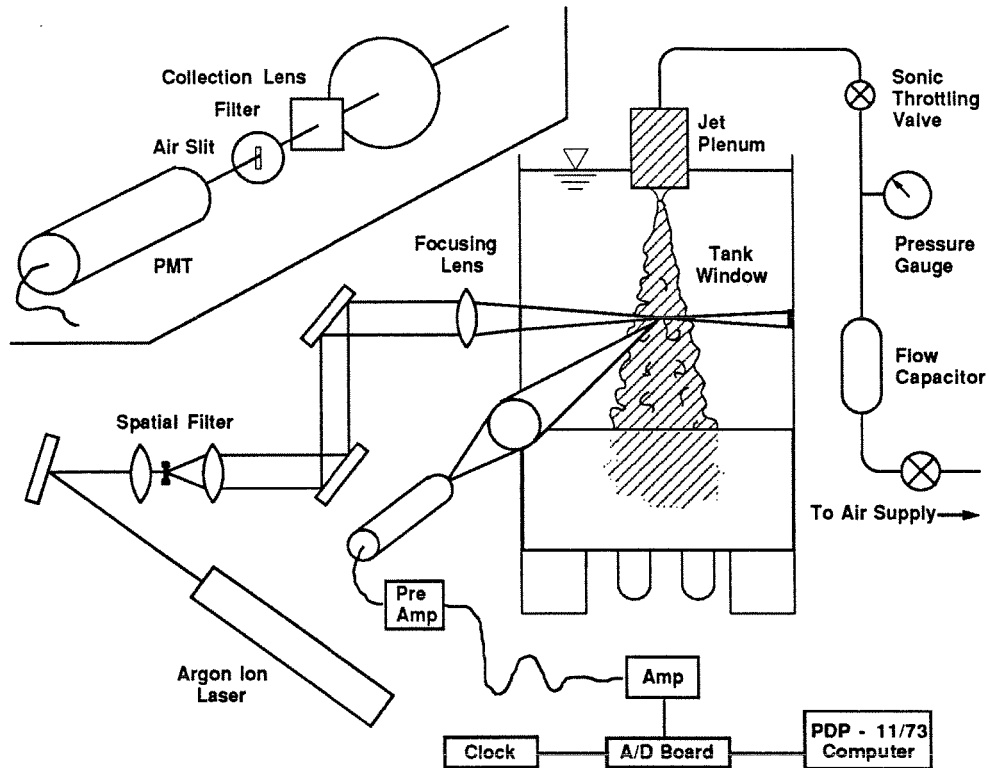


Fig. 2.1 Experimental apparatus (Phase I configuration).

The lab's pressurized air lines were regulated to 4.1×10^5 Pa (60 psi) and used to drive the jet. The jet flow was established by pressurizing a plenum containing a mixture of water and laser dye (disodium fluorescein) by means of sonically-metered air. The dye concentration used was 10^{-6} M or less. The sonic metering valve was used to regulate the mass flux of air driving the jet. The jet plenum was constructed of a cylindrical tube of transparent lucite, 20.3 cm (8 in.) long and 9.5 cm (3.75 in.) I.D., with flat circular endplates. The top endplate contained a connection to the driving air supply and had a small stoppered hole to pour the water-dye mixture in. Inside the plenum was a lucite cruciform to prevent swirl in the plenum fluid. The jet fluid discharged in a blow-down fashion into the large reservoir tank through a 2.54 mm (0.1 in.) diameter nozzle centered on the bottom endplate of the plenum. The nozzle consisted of a short lucite tube cemented into the plenum endplate. The

lip at the entrance to the nozzle from the plenum was rounded off with a radius of roughly 0.5 cm. The tube extended ~ 1.8 cm beyond the endplate of the plenum, and had about a 20° outer taper. See Fig. 2.2. The stainless steel reservoir tank is approximately 2 m in depth and 1 m square. Large plate glass windows provide optical access to the full width of the top two-thirds of the tank on all four sides, and a 25.4 cm (10 in.) circular window is centered on the tank bottom. The top of the tank is open. More details on this flow delivery system may be found in Dimotakis et al. (1983) and Dahm (1985).

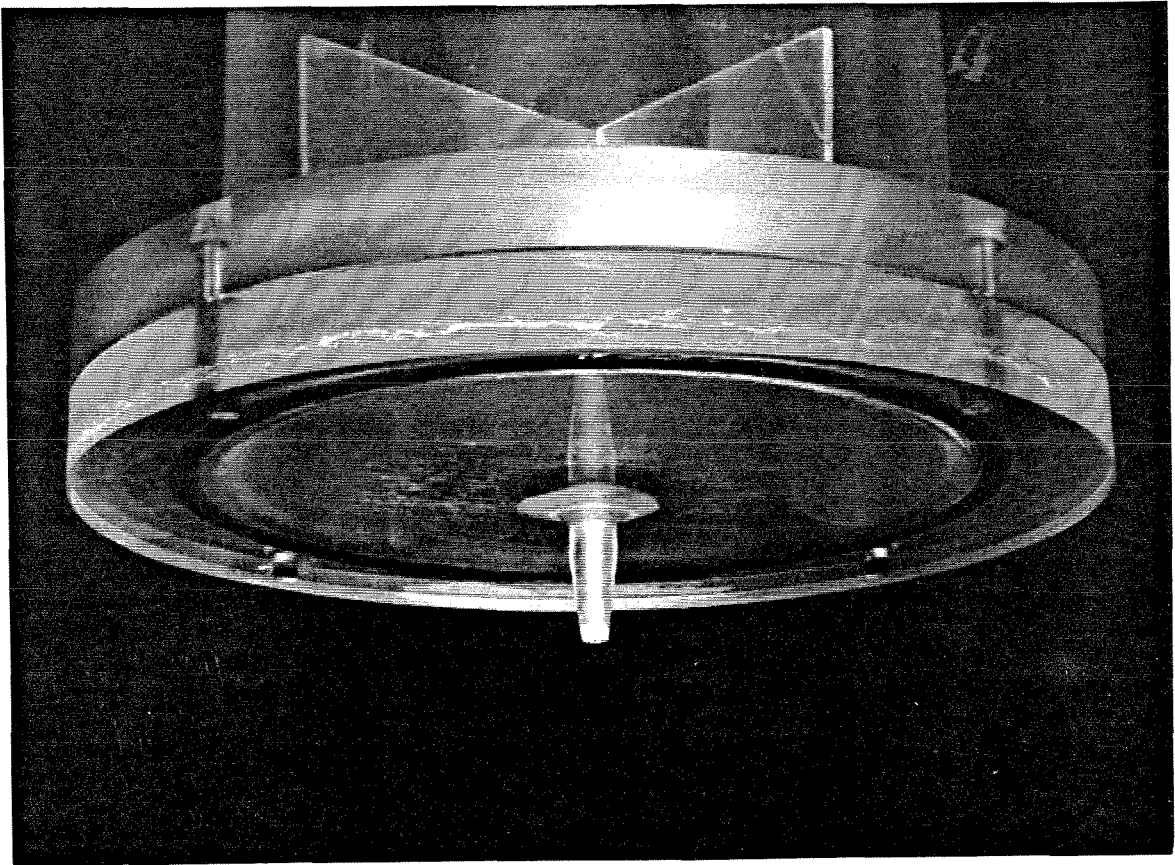


Fig. 2.2 Photograph of Phase I nozzle, with the end of the plenum and cruciform visible. The nozzle exit diameter is 2.54 mm, and the plenum endplate diameter is 14 cm. The nozzle extension protrudes about 1.8 cm from the endplate.

For the Phase I measurements, the beam from an argon ion laser (Coherent CR-3) was spatially filtered, expanded, and focused to a narrow waist on the jet centerline by a high quality achromat lens. The laser power used was 1.0 W, to minimize heating of the fluid by the laser. The visual waist diameter, as measured by a cathetometer, was $80\ \mu\text{m}$. A sheet of black neoprene attached to the inside of the far tank window acted as a beam stop, preventing internal reflections. A low $f\#$, 10 cm (4 in.) achromat lens was positioned at a side window, 90° from the laser beam propagation direction. The beam waist was imaged through a $25\ \mu\text{m}$ vertically oriented slit which determined the third sampling volume dimension (about $50\ \mu\text{m}$), and onto a photomultiplier tube (RCA 8645). A Kodak gelatin low-pass optical filter (#22) was used to eliminate background laser light.

The fluorescence intensity signal generated by the photomultiplier tube (PMT) was pre-amplified by a transimpedance amplifier designed by Dan Lang (with a $50\ \Omega$ line driver) which was mounted in the PMT housing, further amplified by a second low-noise amplifier, and digitized by a 12-bit A/D board (Data Translation 3382). All of the data in the Phase I experiments were sampled at 20 kHz. The amplifier was a derivative of amplifiers used in the HF Combustion Lab at GALCIT (originally developed by Paul Dimotakis and Dan Lang). The design provides very low noise and incorporates a three-pole, low-pass Butterworth filter (at about 8 kHz for Phase I) to satisfy the Nyquist criterion, by some margin. The data acquisition through the A/D board was controlled by an LSI PDP-11/73 CPU-based computer system. The data were transferred via an Ethernet link to a microVAX cluster for post-processing and archiving.

2.2 Single-point measurements – Phase II

A second set of measurements was conducted using many improved components in the experimental apparatus. The unchanged components included the jet reservoir tank and windows, the photomultiplier tube, and the cut-off filter. The basic geometry of the experimental configuration was also unchanged. Otherwise, almost every part of the experiment was upgraded for enhanced performance. A new jet plenum and nozzle assembly were constructed, allowing higher operating pressures and extending the Reynolds number range to 1×10^5 , or more. A larger plenum volume permitted longer run times at axial locations where recirculating dye was not a limiting factor. The jet flow delivery system was replaced with new plumbing, a new control panel, and new wiring. It was designed for driving pressures of up to 2.0×10^6 Pa (300 psi), and plenum pressures up to 1.0×10^6 Pa (150 psi). For some of the runs, a high-pressure gas cylinder replaced the laboratory pressurized air as the high pressure source, and a two-stage regulator was used to set the driving pressure. In later runs, the sonic metering valve was removed from the supply plumbing, and the jet was supplied from a manifold of two gas cylinders that were pressurized to the correct value and then opened to the jet plenum through a valve. The new plenum was constructed out of a 30.5 cm (12 in.) length of 15.2 cm (6 in.) diameter PVC tubing with matching PVC flanges (all schedule 80) on both ends. The flanges were modified to accept o-rings for a reliable seal at the high pressures. The top of the plenum was capped using a PVC blind flange, where a filling valve and driver air connection were installed. The nozzle hole was machined and polished in a large disk of lucite, 3.8 cm (1.5 in.) thick, that was attached to the bottom flange of the plenum. The nozzle consists of a circular arc contour, tangent to the top side of the disk. The radius of the circular arc was chosen such that, at the exit, the nozzle was given a slight 3° inner taper. The

nozzle exit hole has a reasonably sharp lip, and the exit diameter is 2.54 mm (0.1 in.). See Fig. 2.3. This rather formidable nozzle-machining feat was accomplished by Phil Wood of the GALCIT machine shop.

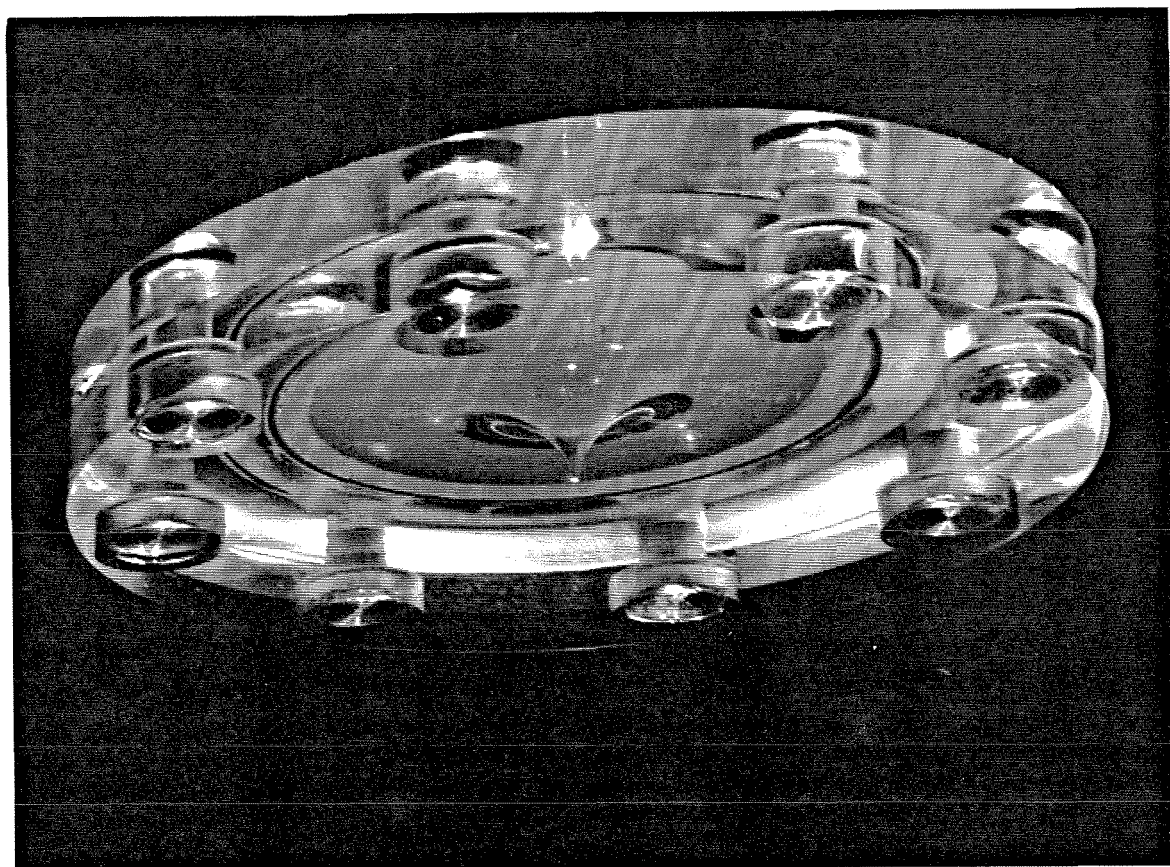


Fig. 2.3 Photograph of Phase II endplate, with the nozzle clearly visible in the center. The view is from below and to the side, through one of the large tank windows. The water surface creates a reflection around the periphery of the endplate. The nozzle exit diameter is 2.54 mm, and the plenum endplate diameter is 30 cm.

In addition to the new flow system, plenum, and nozzle, the laser, laser focusing optics, and collection optics were also upgraded, in two stages. In Phase IIa, a new Coherent Innova 90 argon-ion laser was installed, along with new focusing lenses (5 cm Melles Griot achromats) and a new spatial filter assembly (Newport

model 900). The laser was specially selected for its low-noise characteristics. The combination provided improved beam mode and spatial distribution, thereby reducing the achievable sample volume beam waist dimension and increasing spatial resolution. The lenses were later upgraded again (Phase IIb) to 100 mm (4 in.) Roly Optics achromats, two for the focusing optics, and two for the collection. The typical signal path for the Phase II measurements is shown schematically in Fig. 2.5.

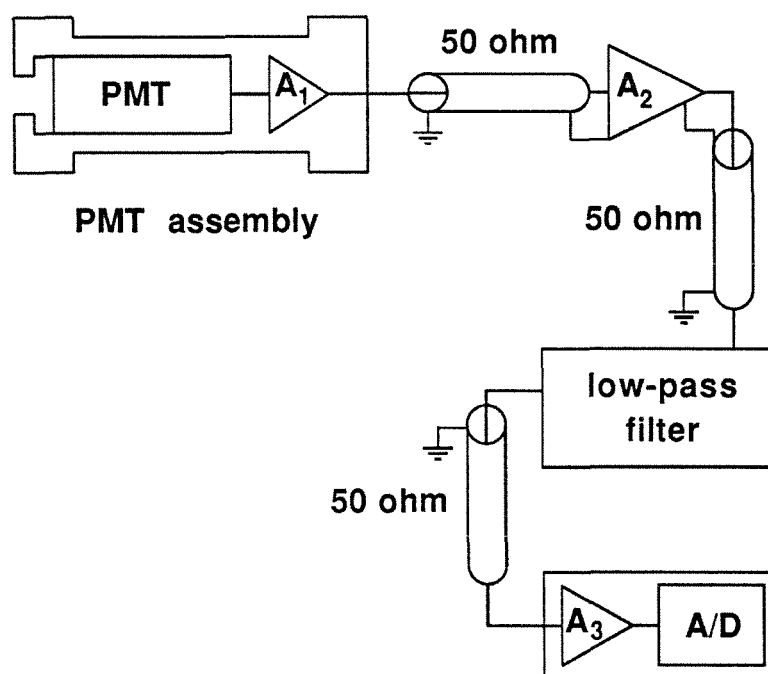


Fig. 2.5 Schematic of signal path from PMT to A/D board.

The PMT and transimpedance amplifier (A_1) from Phase I were connected by $50\ \Omega$ coaxial cable to a Stanford Research Systems SR560 low-noise amplifier (A_2). The amplified signal was low-pass filtered with a Krohn-Hite model 3202R, 4-pole Butterworth filter, and fed to a unity gain buffer (A_3) and then to the A/D board. The SRS amplifier and the K-H filter provided additional flexibility

over the previous, in-house built, amplifier used in Phase I. A 16-bit A/D board (Data Translation 2757) replaced the previous 12-bit version. Data acquisition software changes permitted writing the data directly to disk, greatly expanding the temporal dynamic range of the data. This allowed records of up to 500 large-scale structure passages to be collected, while maintaining full resolution of the viscous scale described in Appendix C.

A photograph of the facility in its Phase II configuration is included in Fig. 2.4.

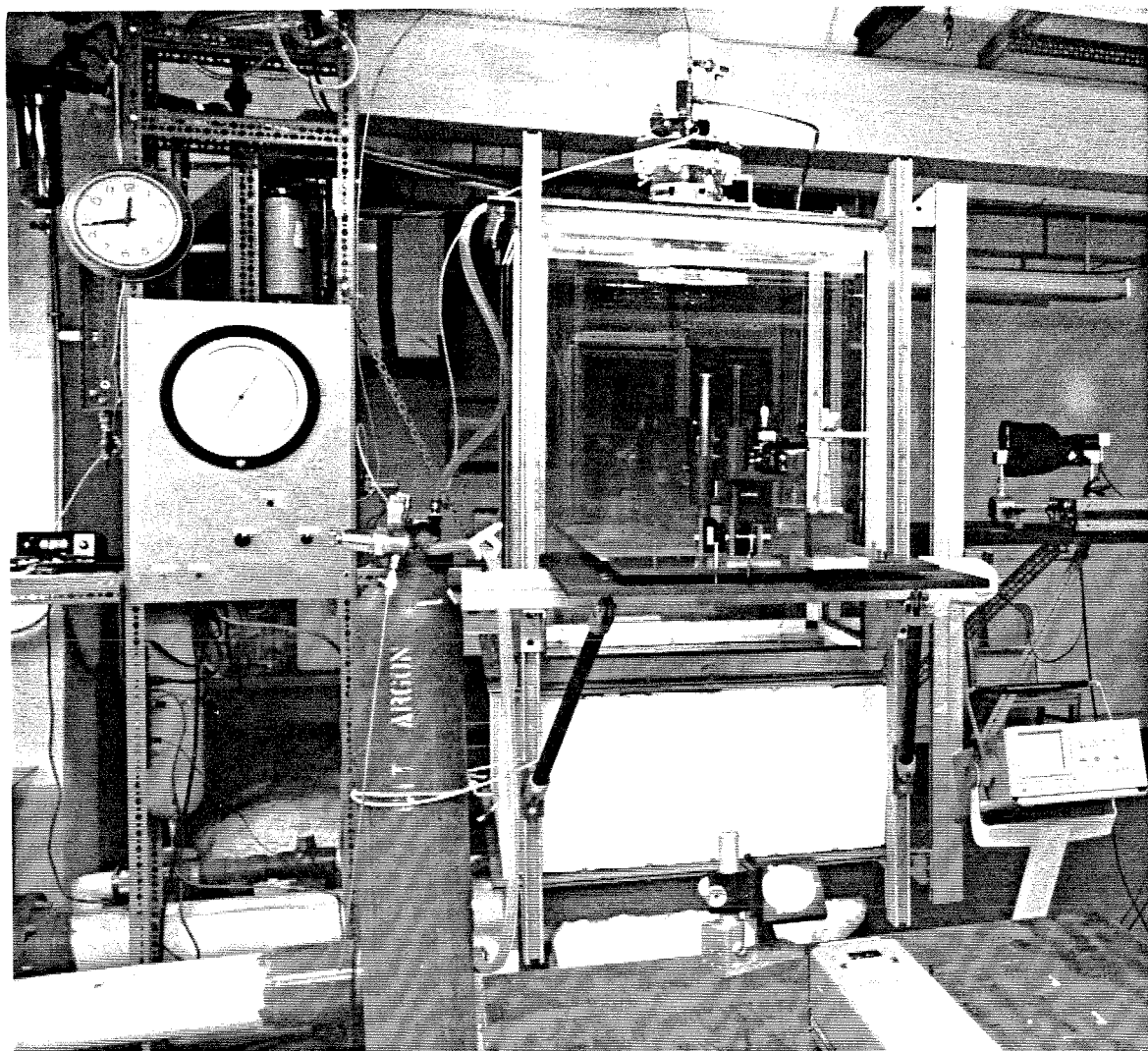


Fig. 2.4 Overview of facility during Phase II. The tank, with the adjustable shelves, is just right of center. For scale, the tank windows are about 1 m wide. The control panel is on the left, and the PMT and second-stage amplifier are on the shelf to the right (above the oscilloscope). The end of the laser is visible at the bottom right, and the focusing optics are on the shelf in front of the tank. The plenum is mounted in the top of the tank, and the nozzle plate can be seen just below the surface of the water.

CHAPTER 3

Structure and statistics of the scalar field

This chapter examines aspects of the structure and statistical behavior of a high Schmidt number turbulent jet scalar (concentration) field. Time traces of the concentration signal on the jet axis are examined directly for possible characteristic behavior. The dynamic range of the fluctuations is striking, and the presence of both ramp-like and plateau features is suggested. Histograms of the jet concentration are accumulated and investigated as a function of sample size. For long record lengths, the histograms approximate the true probability density functions (pdf's) of the jet concentration. The histograms, which usually form in a very localized manner at short record lengths, are slow to converge, and typically exhibit bumps and protuberances of a greater magnitude than would be expected from a random process. The behavior of the mean concentration value is explored via the autocorrelation of an auxiliary (zero-mean) process. The mean is found to converge rather slowly, suggesting that very low-frequency fluctuations are present. The approach to convergence is discussed using quantitative measures. The variance of the concentration, $\overline{(c - \bar{c})^2}$, where the overbar denotes a time average, is examined, and is also found to converge slowly. Finally, a simple model of the large-scale jet concentration field is employed to study the magnitude of several possible influences. It also ties together aspects of the time traces, the concentration histograms, and the variance behavior.

3.1 Time traces of the concentration

Since the data discussed here are Eulerian, single-point measurements *versus* time (acquired as described in Chapter 2 and the appendices), a logical first step toward understanding the behavior of the scalar field structure is to examine these traces directly. However, in setting out to do so, it immediately becomes apparent that the display of the information poses a challenge. The dynamic range of these data is so large (up to more than five decades) that, like most high Reynolds number turbulent flows, it is possible to view only a limited bandwidth at a time. In an attempt to overcome this difficulty, and as an informative demonstration before beginning some more detailed and specific analyses, a data record was processed so that it could be plotted *logarithmically* in time (Fig. 3.1). To avoid plotting several million points, such processing necessarily involved sampling the data. To eliminate sharp resolution changes between decades, every point of the record was plotted at small times, up to times where the spacing was sufficiently small between adjacent points. Thereafter, an approximately constant \log_{10} spacing was maintained. On account of the sampling, the signal in Fig. 3.1 at large times appears less jagged than it actually is. The aspect ratio of the plot was stretched to enhance readability.

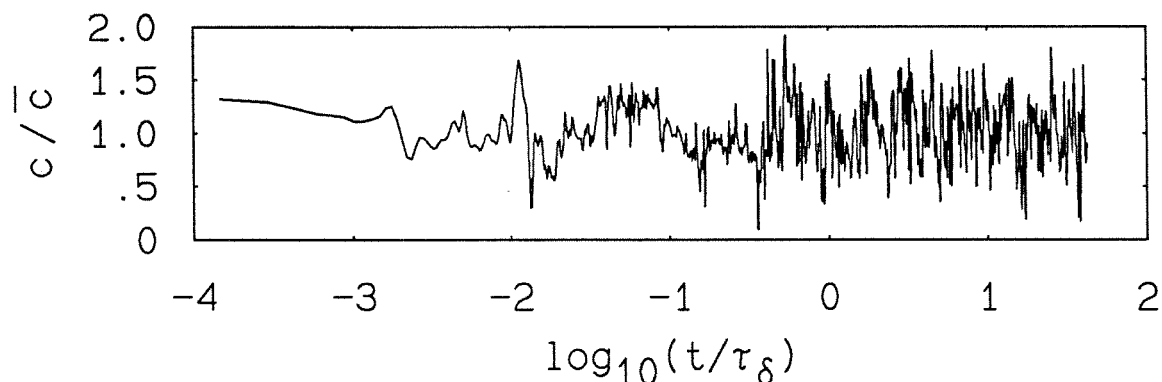


Fig. 3.1 Logarithmically plotted concentration trace; $Re = 6,000$, $x/d = 305$.

Several features are apparent in Fig. 3.1. In the vicinity of $\log(t/\tau_\delta) \approx -1$ to -0.5 , there is what might be called a “plateau,” i.e., a relatively level region of the signal. In the neighborhood of $\log(t/\tau_\delta) \approx 0$, corresponding to scales on the order of the jet diameter, several “ramp-like” structures may be discerned. This is further demonstrated in the plot of another concentration trace in Fig. 3.2. Here, the Reynolds number is about three times as high as that in Fig. 3.1, while the axial location is one third as far. Again, several ramps are visible, as well as a plateau. The pronounced fluctuations visible in these plots, it should be emphasized, are not noise, but fine-scale concentration fluctuations. The data were Wiener-filtered as described in Appendix B, and then sampled at every fourth point, since they had been oversampled to begin with.

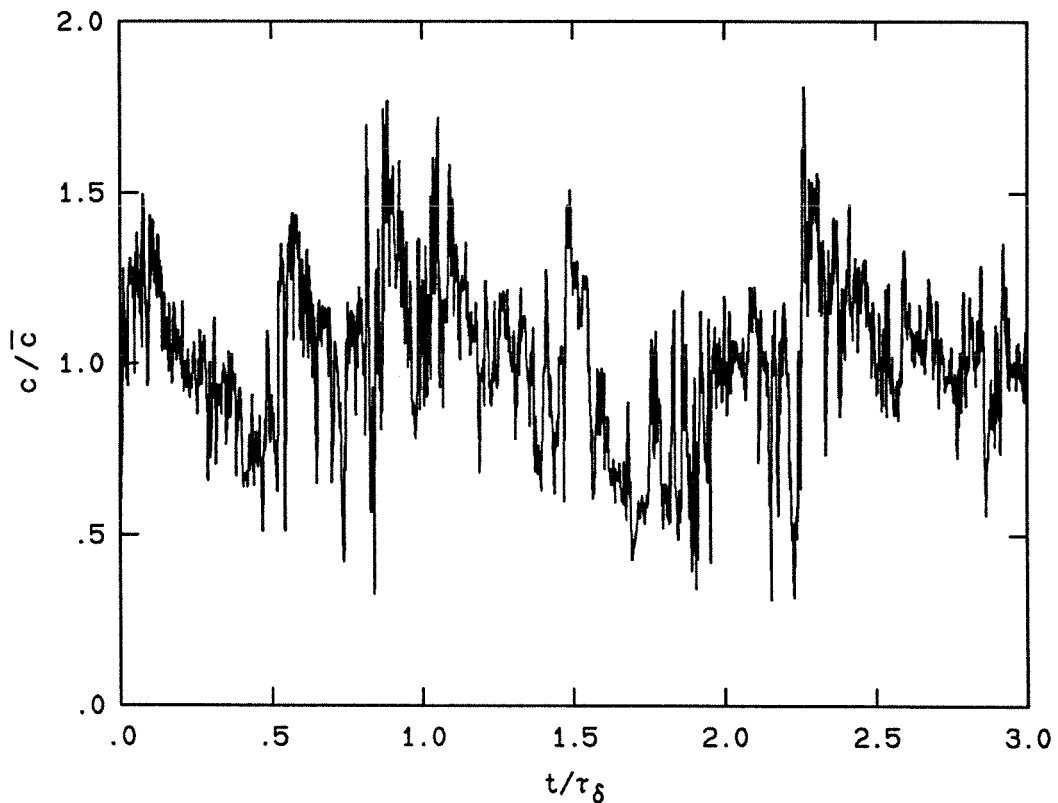


Fig. 3.2 Concentration trace; $Re = 12,500$, $x/d = 100$.

If we consider the jet concentration trace to be represented by a series of ramp-like structures, the plateaus, and many of the small chunks of ramps observed, are pictured as the products of collisions between two or more ramps, necessitated by the scaling laws governing the large-scale spacings in the jet. The collisions are envisioned to cause a scrambling of the involved ramps in a large-eddy turnover type of event, e.g., similar to the “triplet map” utilized by Kerstein (e.g., 1990) in his linear-eddy model.

While it is not the intention here to represent the jet centerline concentration as a simple conglomeration of plateaus and ramps, their occurrence is ubiquitous, and cannot be ignored. Almost every record examined contained ramps, while rarely, the trace was an indistinct hash. Fig. 3.2 was selected as a strong example out of a random six records of that particular data set. For comparison, Fig. 3.3 is included, chosen without prior examination, even as this is being written. No comment will be made upon it. An additional question, whether this particular data run is representative, is difficult to answer, and will be addressed to some extent in Chapter 4.

The presence of decreasing ramp structures in the time traces of the jet scalar field is consistent with findings of some other investigators, e.g., Dowling (1988), in gas-phase, but contradicts a conclusion by Dahm (1985), in which he states that no ramps exist in high Schmidt number jets. His conclusion is a bit surprising, since, based on his own flame-length visualizations, large-scale structures in the flame were observed to burn out in a rear-to-front manner. See also the discussion of entrainment in Dahm & Dimotakis (1987). The flame-length behavior certainly suggests that the concentration in the structures similarly increased from rear to front, in agreement with the ramps observed in the current work.

A last point concerning the concentration traces is their appearance over long

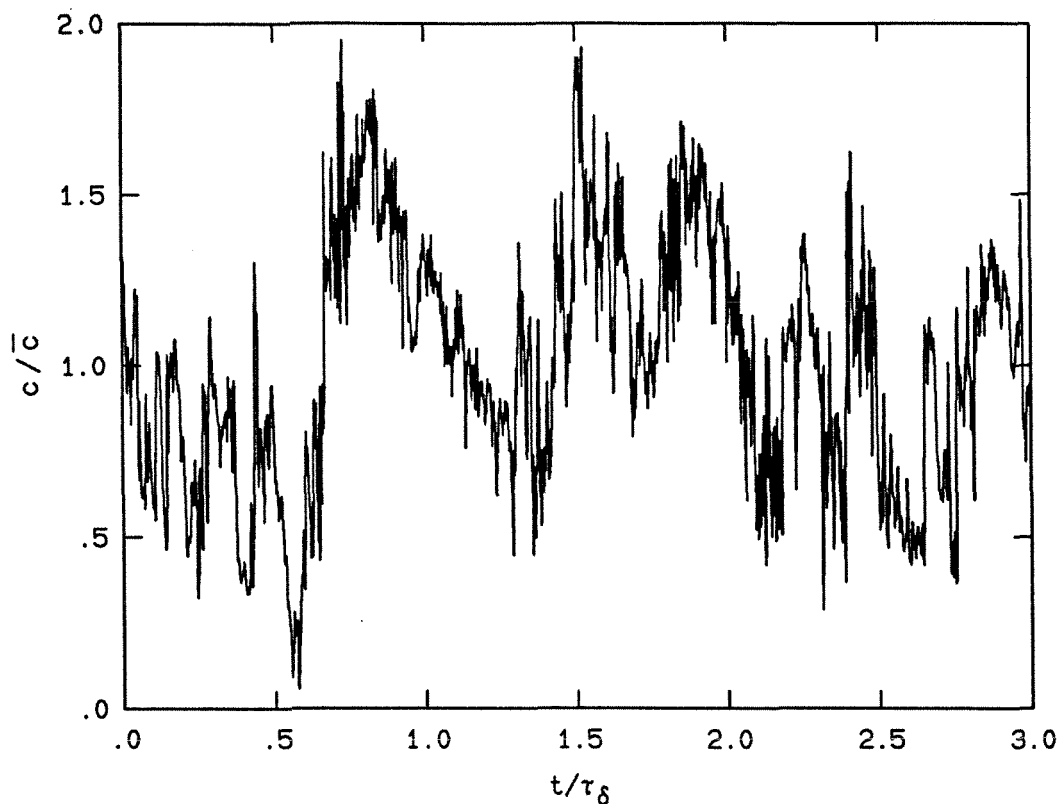


Fig. 3.3 Randomly selected record from the same run as Fig. 3.2; $Re = 12,500$, $x/d = 100$.

times. Data records of many large-scale times were compressed by convolving them with a large Gaussian filter and sampling the result at the filter's standard deviation. A sample is plotted in Fig. 3.4. A somewhat striking feature of these plots is that they exhibit a certain degree of structure, in the sense that the trace doesn't look very uniform, even over time scales of dozens of large-scale structure passages, or so. This observation prompted further investigation into the convergence of the mean, which is discussed in a later section.

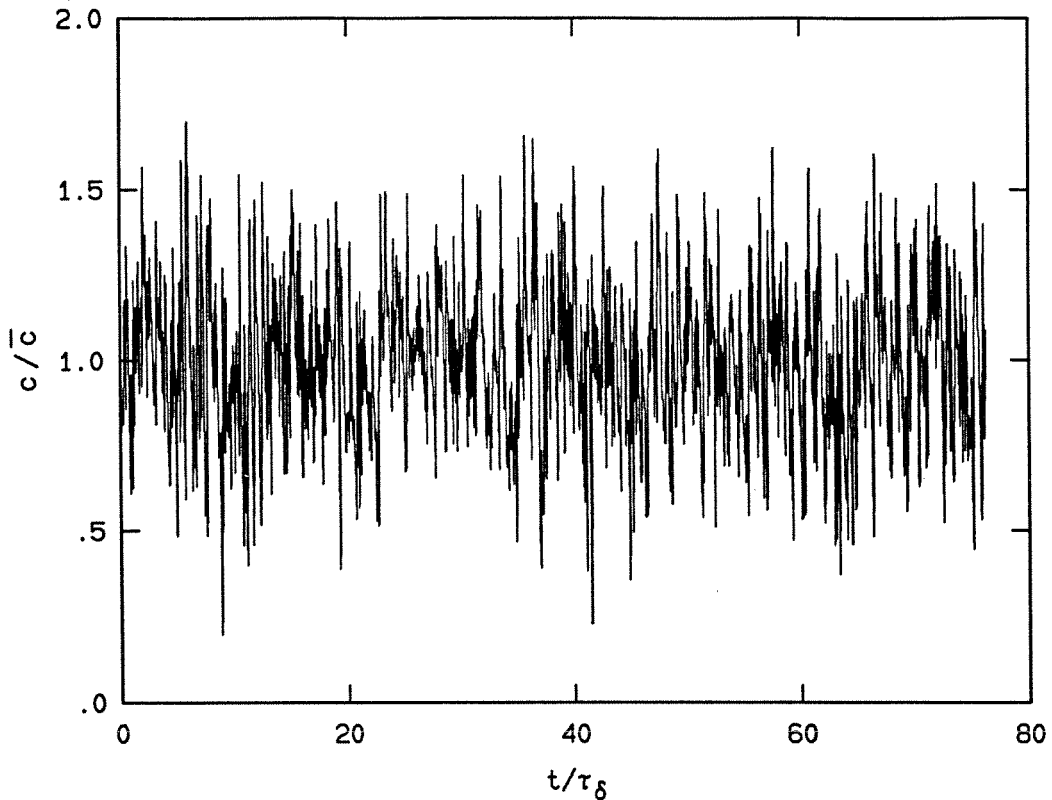


Fig. 3.4 Long concentration record, compressed after filtering with a Gaussian ($\sigma = 100$ sampling times); $Re = 25,500$, $x/d = 170$.

3.2 Histograms of jet concentration

Another basic statistical measure of the concentration measurements is a normalized histogram of the time history of the concentration at the measurement point. For long record lengths, this approximates the true jet concentration probability density function, or pdf. The result expresses the fraction of the time a particular concentration value is encountered, as well as the variance of the concentration (the second moment of the pdf). A sample plot of the probability of c/\bar{c} is shown in Fig. 3.5. As is typical for this flow (on the jet centerline), little low-concentration fluid (reservoir fluid represented by zero) is present, the distribution is peaked at or near the mean, and the estimated pdf falls off rapidly at higher concentrations, normally never exceeding a value 2 or 2.5 times the local mean.

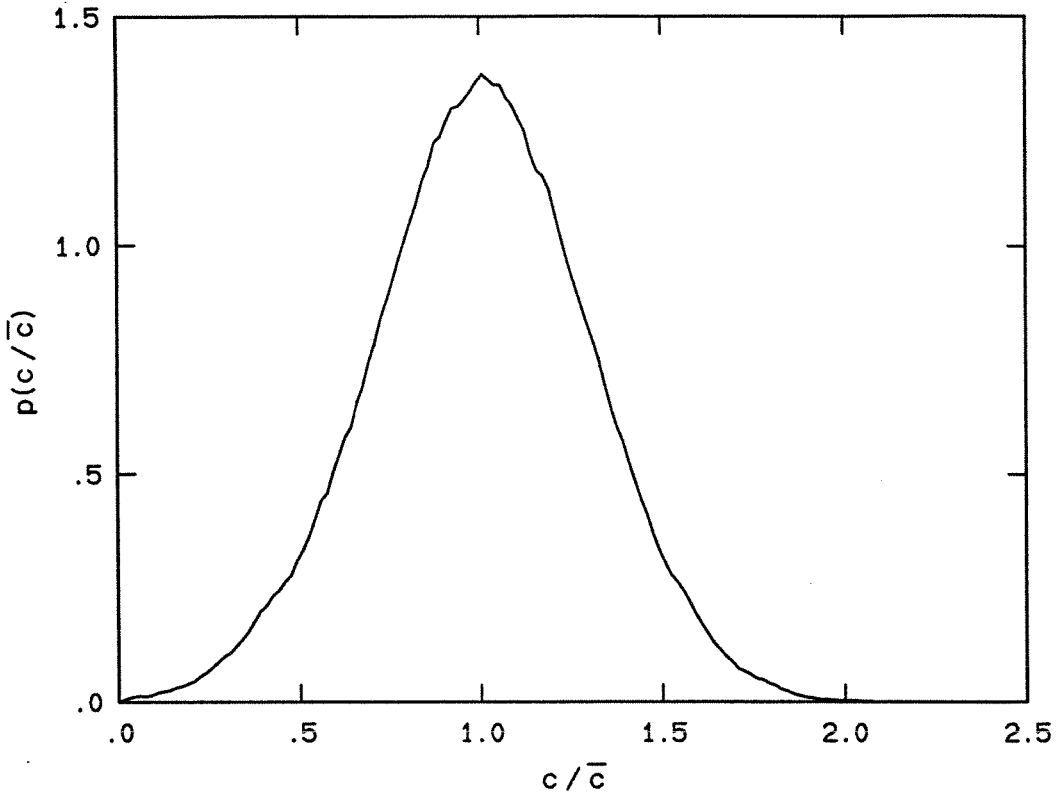


Fig. 3.5 Estimated pdf of long data record (about 477 times τ_δ) ; $Re = 12,500$, $x/d = 100$.

The case shown was chosen because it represents one of the highest resolution conditions with a large number of structures. The number of bins used to construct the histogram is 150.

The histogram in Fig. 3.5 is compiled from over two million data points. Distributed over 150 bins, that produces an average of almost 14,000 points per bin. Near the histogram peak, there are actually closer to 35,000 points per bin. Consider the *fractional deviation* of a binomial process (e.g., as discussed in Morse, 1969),

$$\frac{\sigma_n}{N} = \left(\frac{pq}{N} \right)^{1/2}, \quad (3.1)$$

where p is the probability of an event, q is $1 - p$, and N is the number of trials. Near the peak of the histogram, the plot indicates that $p \approx 0.0225$ per bin. The

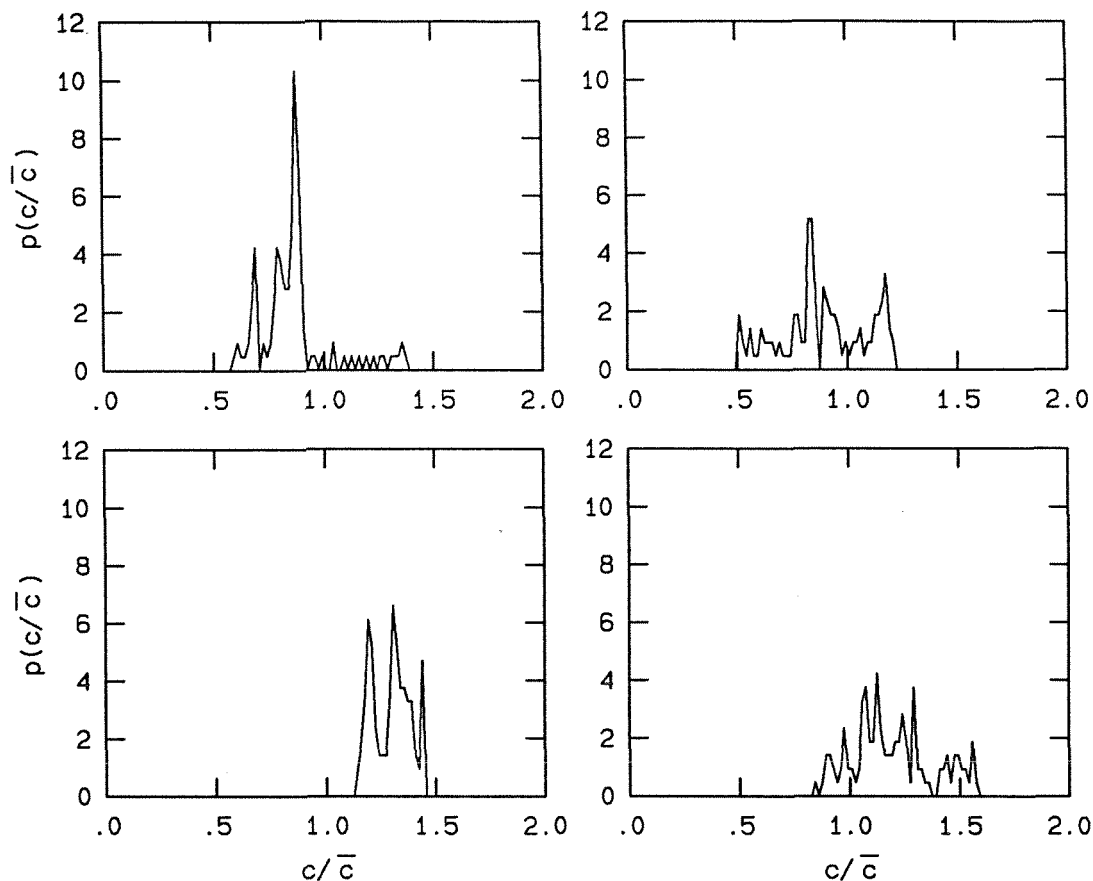


Fig. 3.6 Histograms from records $0.03 \tau_\delta$ long, spaced $70 \tau_\delta$ apart. $Re = 12,500$, $x/d = 100$.

product of p and its complement q is therefore 0.022. If the histogram were governed by the random statistics leading to Eq. 3.1, the fractional deviation near the peak would be about $0.148 / \sqrt{N}$, or 0.08% – less than the line thickness used to plot the histogram, by some margin.

Since deviations from a smooth curve greater than these amounts are visible in Fig. 3.5 (e.g., at about $c/\bar{c} \approx 1.2$), we must conclude that either the histogram does not conform to binomial statistics, or that the features exist in the (infinite time) pdf. The two possibilities may be addressed by performing this analysis on shorter records, and then examining longer ones to see if the deviations persist. This has been done qualitatively. It is concluded that the small-scale deviations

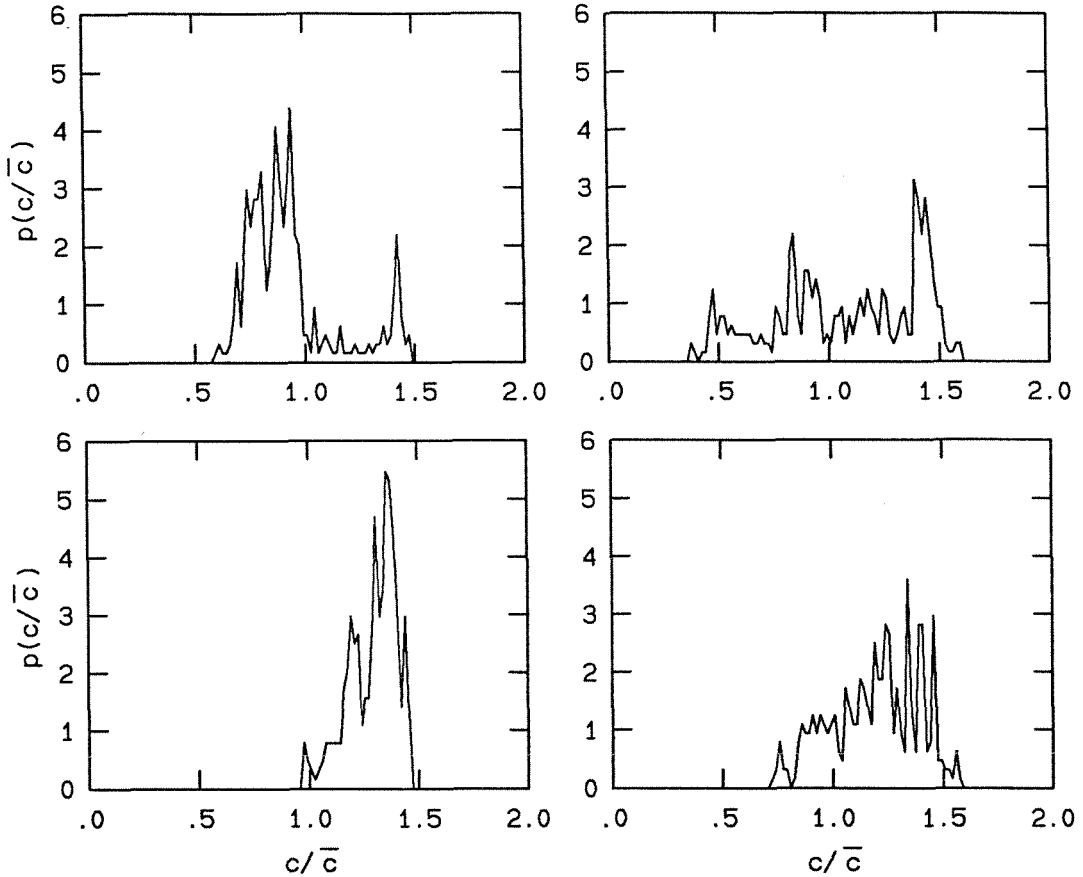


Fig. 3.7 Histograms from records $0.1 \tau_\delta$ long, spaced $70 \tau_\delta$ apart. $Re = 12,500$, $x/d = 100$. Bottom-left, plateau-like; top-right, ramp-like.

of the histogram from a smooth shape, particularly near the mean, are statistical artifacts, and, therefore, that the histogram does not conform to binomial statistics. However, the slight bulges which appear in both wings of the histogram, at c/\bar{c} of about 0.45 and 1.6 (and may be viewed by sighting down the sides of the curve), are a different matter. These bumps have been observed in many different cases, and if they do not represent the long-time shape of the pdf, they are an example of a statistical fluctuation which takes an extremely long time to die out.

It is concluded that the deviations represent evidence that the statistics of the histogram differ from a “random” or binomial behavior to a considerable degree. As a further illustration of this, additional analysis was conducted on the run rep-

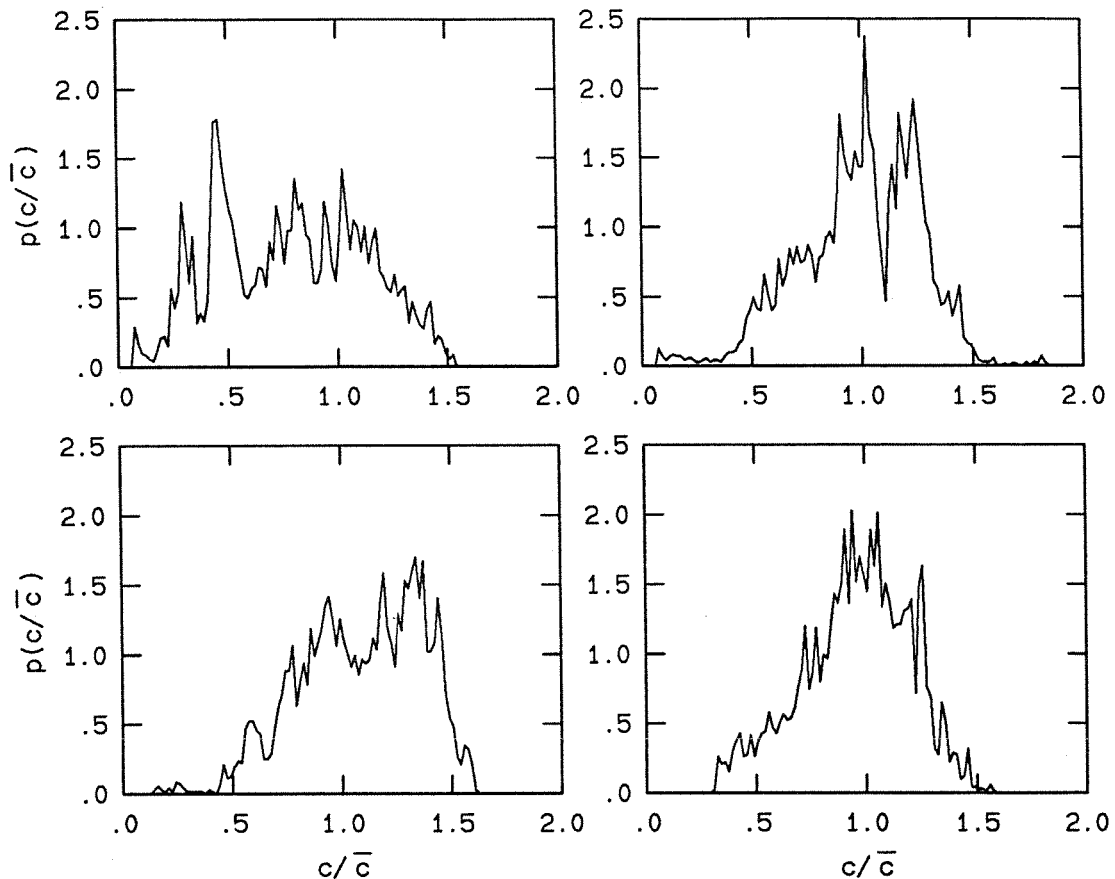


Fig. 3.8 Histograms from records $1 \tau_\delta$ long, spaced $70 \tau_\delta$ apart. $Re = 12,500$, $x/d = 100$.

resented in Fig. 3.5. Histograms were computed of various length portions of the record, from 3% of τ_δ to 100 times τ_δ . Four such histograms were compiled of each length, each beginning $70 \tau_\delta$ apart, except for the $100 \tau_\delta$ histograms, which were contiguous. Each short record is included in the corresponding longer records. The large separation was used in an attempt to have the records be as statistically independent as possible, and the records used were not selected to any degree for their appearance. The results for record lengths of $0.03\tau_\delta$, $0.1\tau_\delta$, $1 \tau_\delta$, and $10\tau_\delta$, are displayed in Figs. 3.6–3.9. The $100 \tau_\delta$ results are included in Fig. 3.10. On the figures composed of four separate plots, the relative order of the short records in the run is top-left, top-right, bottom-left, and bottom-right.

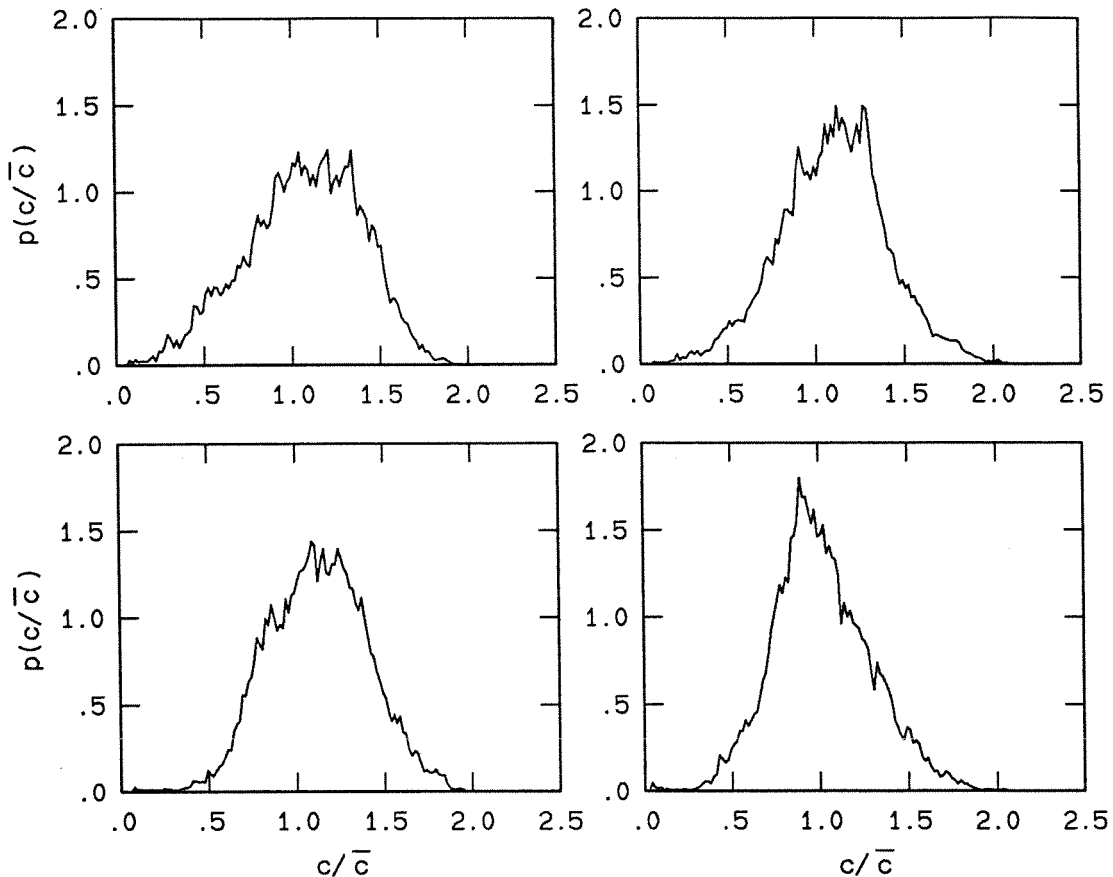


Fig. 3.9 Histograms from records $10 \tau_\delta$ long, spaced $70 \tau_\delta$ apart. $Re = 12,500$, $x/d = 100$.

Please bear in mind the discussion above involving ramps and plateau features in the concentration trace. Note that the histogram resulting from a ramp is uniform across the ramp's range, while the contribution of a plateau to the histogram is strongly peaked, approaching a delta function for a perfectly flat plateau. Also note that the contribution to the histogram at a maximum or minimum point of the concentration trace would be expected to resemble the pdf of a parabola, which has a singularity at the turning concentration c_{turn} , dropping off rapidly like $1/|c - c_{\text{turn}}|$. This type of behavior is expected whenever the concentration trace has an extremum and the contribution from the vicinity of the extremum represents a significant fraction of the record (i.e., short records). At short times in Figs. 3.6–3.8,

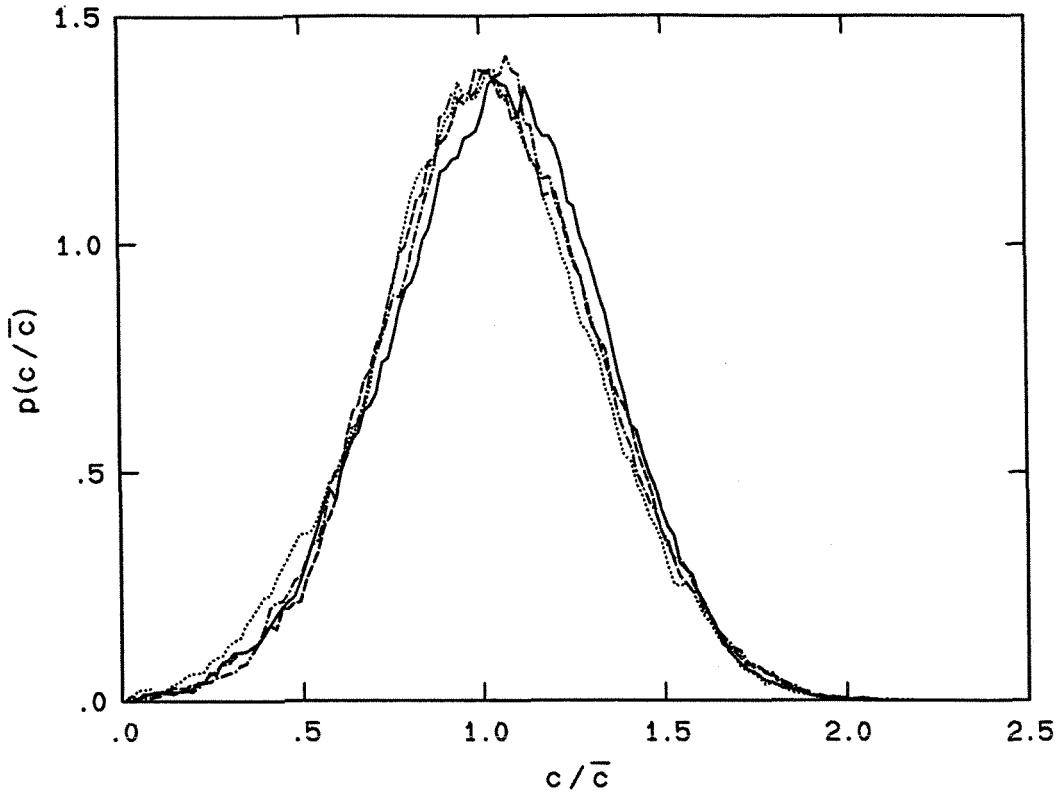


Fig. 3.10 Histograms from contiguous records $100 \tau_\delta$ long. $Re = 12,500$, $x/d = 100$.

characteristics of these cases are visible. Sharp spikes indicate relatively constant concentration values, broad or flat regions are consistent with ramps, and the histogram edges are typically very sharp and somewhat peaked, in agreement with anticipated turning point behavior. In particular, the histograms do not form over time in a manner resembling the textbook accumulation of the eventual pdf. This is not surprising, since the continuity of the concentration signal, among other things, imposes constraints upon how the histogram accumulates.

Increasing the time scale, the records consisting of a single large-scale passage, supposedly the longest fluid dynamical time scale of the flow, only vaguely resemble Fig. 3.5. The appearance of the $10 \tau_\delta$ histograms is noteworthy, particularly the bottom-right, which is very pointed. The four cases all differ significantly. Also

note the small bumps at the extremes of these histograms, again in agreement with turning point behavior. It is apparent that the development of long, thin, tapered tails on the pdf, particularly near zero concentration, is a slow process if the constituents are themselves tapered in the wrong direction.

In the final plot of the group (Fig. 3.10), the histograms are finally shaping up. However, note that the mean of the solid-line curve in Fig. 3.10 differs quite noticeably from the others. Similar behavior of the mean has been witnessed in many other runs and seems to be unrelated to the relative location in the data record (whether at the beginning, middle, or end). The fluctuations in Fig. 3.10 are in spite of the fact that *each* of those histograms contain 100 large-scale structures, and leads naturally to the examination of the statistics of the mean in the next section.

3.3 Behavior of the mean

Many possible ways of examining the behavior of the mean were considered, and several were explored, but one in particular was the most informative and quantitative. The tactic is to define an auxiliary process, $w'(T)$, that consists of the time average of the concentration fluctuation $c'(t)$ over a time T , i.e.,

$$w'(T) = \frac{1}{T} \int_0^T c'(t) dt = \frac{1}{T} \int_0^T [c(t) - \bar{c}] dt, \quad (3.2)$$

where \bar{c} is the average concentration of the entire record. It can be shown, e.g., Papoulis (1984), that if the autocorrelation function $R_{c'c'}$ exists, the variance of $w'(T)$ is

$$\text{var}\{w'(T)\} = \frac{1}{T} \int_{-T}^T \left(1 - \frac{|\tau|}{T}\right) R_{c'c'}(\tau) d\tau = \sigma_{w'}^2(T). \quad (3.3)$$

Additionally, if $R_{c'c'}(\tau) \approx 0$ for $\tau > T$, then,

$$\sigma_{w'}^2(T) \rightarrow \frac{\text{constant}}{T} \sim \frac{\text{var}\{c'(t)\}}{T}. \quad (3.4)$$

In other words, not only is the variance of the auxiliary process obtained, but it can then be related to the expected asymptotic correlation behavior of $c'(t)$ for long times, assuming the autocorrelation is small enough. Alternatively, the long-time behavior is a measure of the convergence of the autocorrelation to zero. The autocorrelation isn't examined directly, because, in addition to obtaining a quantitative estimate for $\text{var}\{w'(T)\}$, this method relies on an integral which helps to reduce the impact of a noisy autocorrelation at long times.

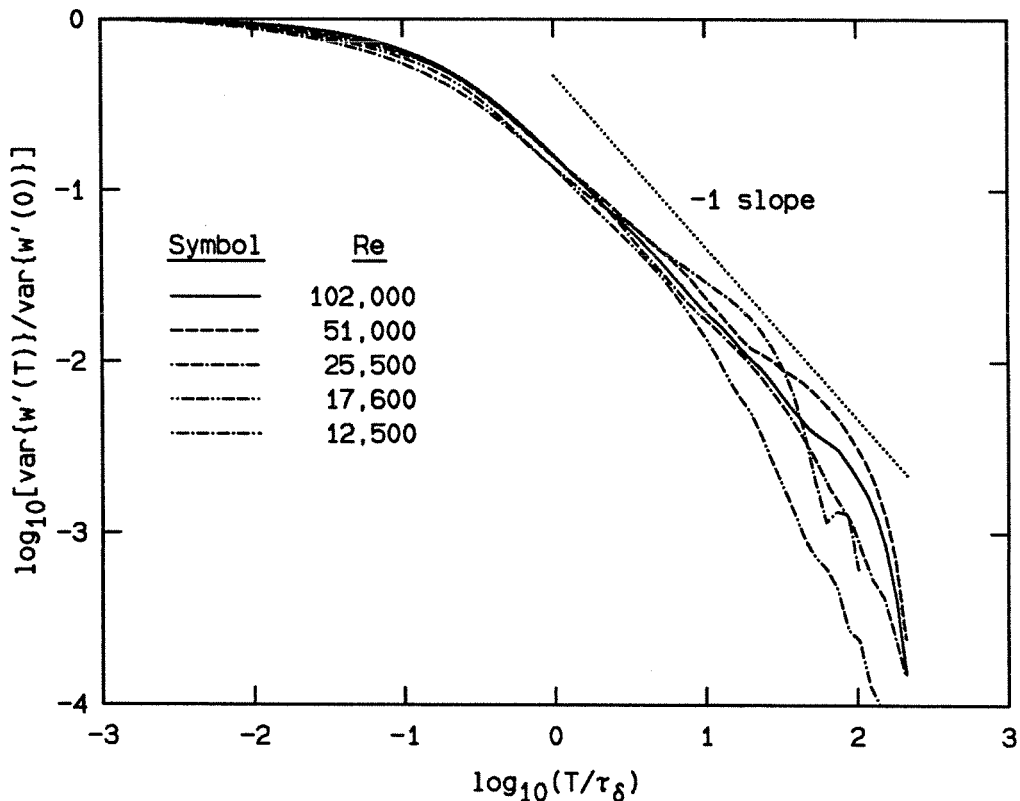


Fig. 3.11 Computation of the variance of Eq. 3.3 for long data records (Phase II, $x/d = 100$).

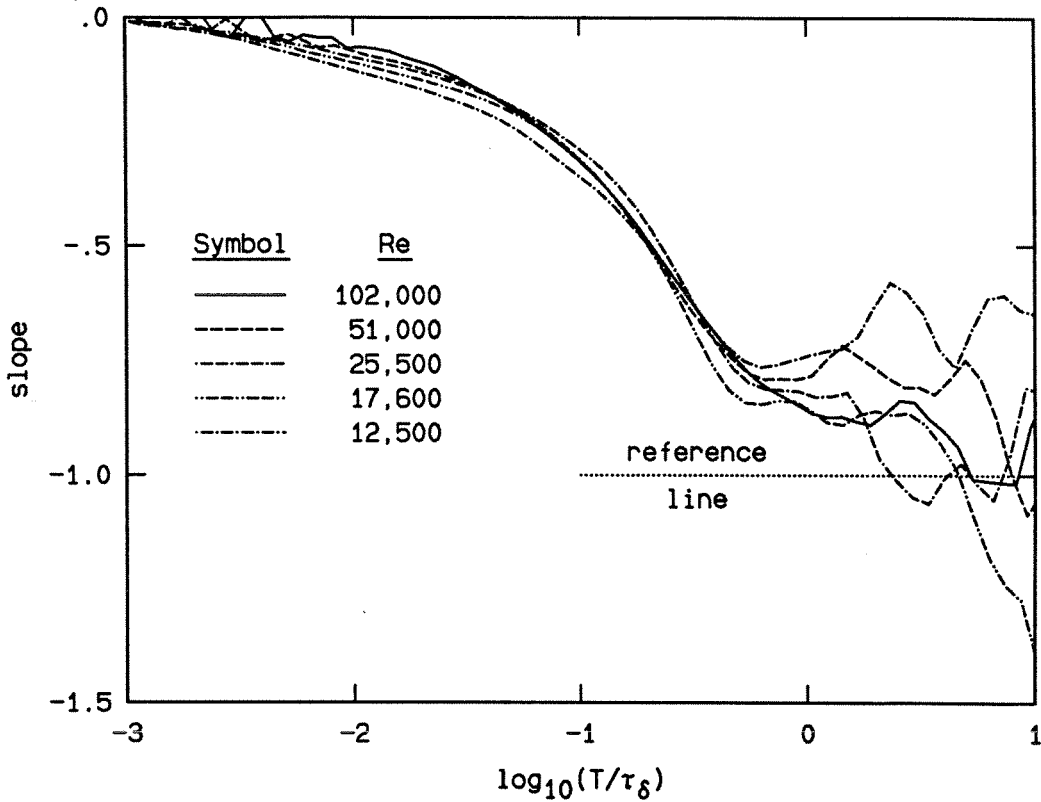


Fig. 3.12 Slopes of the curves in Fig. 3.11, computed numerically.

The result of the calculation for a sequence of runs conducted at $x/d = 100$ is shown in Fig. 3.11. The variance of the auxiliary process declines slowly at small times, passing a knee at about a tenth of a large-scale time, and finally achieves a, more or less, constant slope at large time. Small bumps near the longest times are end-effects. This plot shows how many large-scale structures are required for the mean to have converged within a given uncertainty. Typical values of $\text{var}\{w'(0)\}$, equivalent to the record variance, are about 0.1, or so. Therefore, if we desire the mean to converge to within (a standard deviation of) 1%, which would correspond to a value of $\text{var}\{w'(T)\} / \text{var}\{w'(0)\}$ of roughly 10^{-3} , Fig. 3.11 suggests that 100 structures are required. Actually, as will be discussed below, it is perhaps better to extrapolate the lines from the vicinity of $T/\tau_\delta = 1$, which would then indicate that perhaps 300 structures are required to reduce the uncertainty in the mean to

1%. It is interesting to note that similar empirical rules have been suggested in the extraction of shear layer behavior statistics (cf. Dimotakis & Brown 1976).

To better extract the long-time behavior of the curves in Fig. 3.11, the curves were differentiated numerically to yield the logarithmic derivatives (slopes). These were then plotted as a function of T/τ_δ in Fig. 3.12. The numerical differentiation was implemented using different multipoint schemes, and the particular method utilized was not found to influence the results. Also included in this figure is a reference line at -1 , corresponding to the behavior of a converged autocorrelation. The “true” slope values cannot actually maintain values less than -1 , since the best the autocorrelation can do to help is to assume a zero value at some time, which is exactly the condition under which Eq. 3.4 applies. Therefore, the occurrence of smaller values indicates that the statistics of this measure, as usual with an autocorrelation, deteriorate near the end of the record, causing large fluctuations in the slope values. For this reason, the slopes were not plotted beyond $10 \tau_\delta$, although the records used were about $230 \tau_\delta$ in length. Nevertheless, it is clear that they level out at values somewhat shy of -1 .

If the slope levels out at a value α , where $0 > \alpha > -1$, then it is implied that

$$\text{var}\{w'(T)\} \propto T^{1+\alpha} , \quad (3.5)$$

which, by Eq. 3.3, suggests that $R_{c',c'}(\tau) \propto \tau^\alpha$. In other words, the autocorrelation is decreasing with τ slower than exponentially, i.e., as a power law.

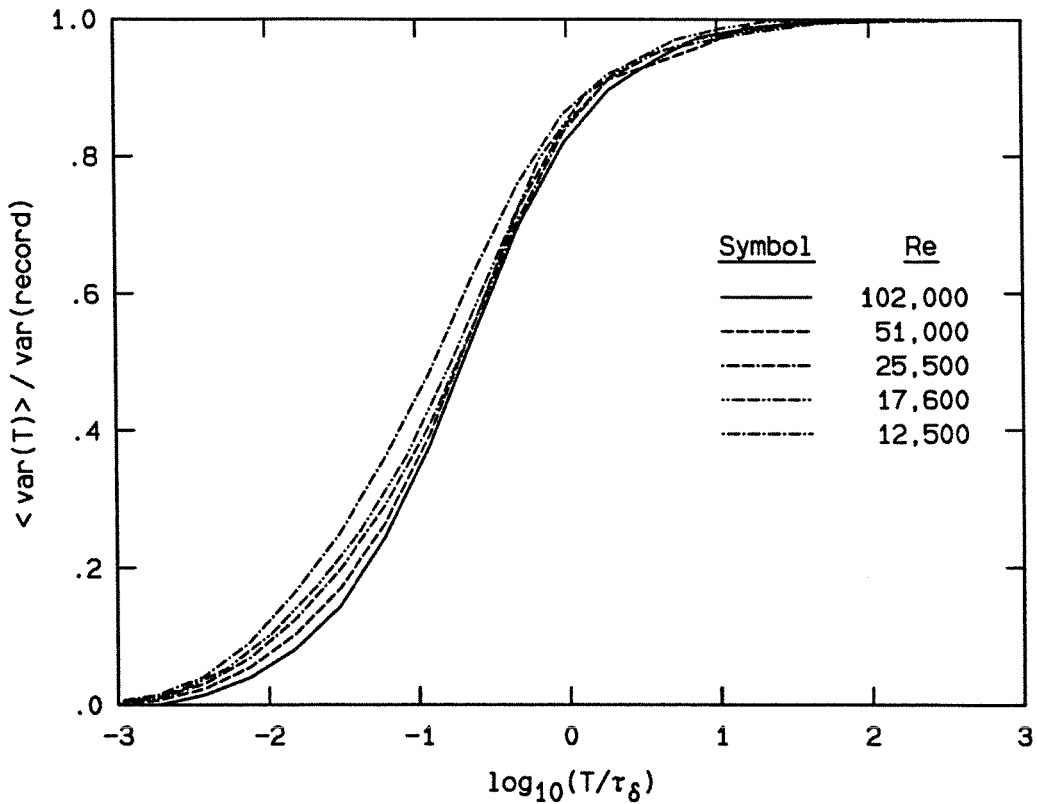


Fig. 3.13 Ensemble-averaged variances for sub-records of length T , normalized by the variance of the entire record. Phase II data, $x/d = 100$.

3.4 Variance of the concentration

In principle, an analysis similar to the one conducted above for the mean is possible for the variance, also. However, a slightly different approach was chosen, in which the accumulation of the variance is calculated as the scale of interest is increased from the smallest time scales up to the record length. A record which consisted of the largest number of points that were an exact power of two was extracted from the data of an entire run. A program was written to process the record, computing the variance of every two adjacent data points with respect to their own mean, then every four data points, eight, and so on, up to the full record length, at which point the variance of the entire record is recovered. The individual contributions are averaged at each scale and normalized by the record variance.

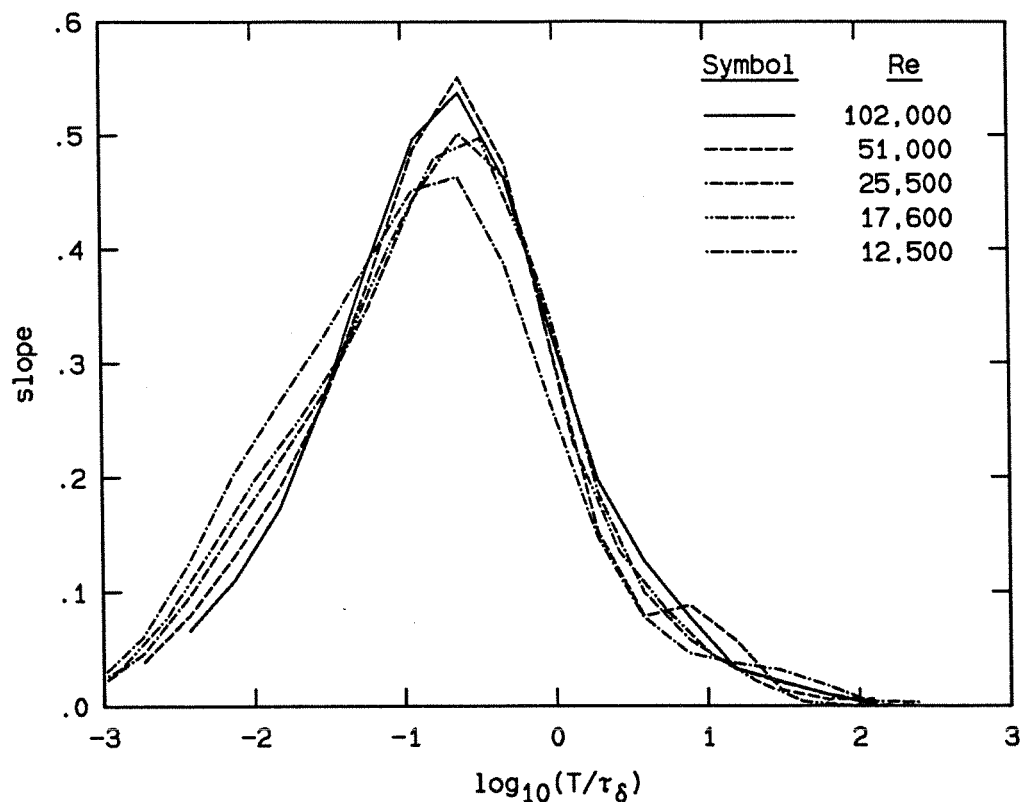


Fig. 3.14 Slopes of the curves in Fig. 3.13, computed numerically.

The net result is a cumulative integral of the variance, starting at the sampling interval, and increasing in scale. We recognize that this is information that is also contained in the concentration power spectrum, which will be explored in some detail in Chapter 4.

The results are displayed in Fig. 3.13 for the same runs that were used in Fig. 3.11 and 3.12. Note that the resolution on these plots, roughly $\log(T/\tau_\delta) = -2.6$, does not change with Re (see Appendix C). An interesting conclusion from Fig. 3.13 is that only about 80% of the variance is contained in portions of the signal spanning a large-scale passage time. If Fig. 3.13 represents the cumulative contribution to the variance, then the contribution to the variance from each scale may be estimated by the derivative of the curves. The slopes are shown in Fig. 3.14, using the same symbols as in the previous plot. The slopes of the unnormalized

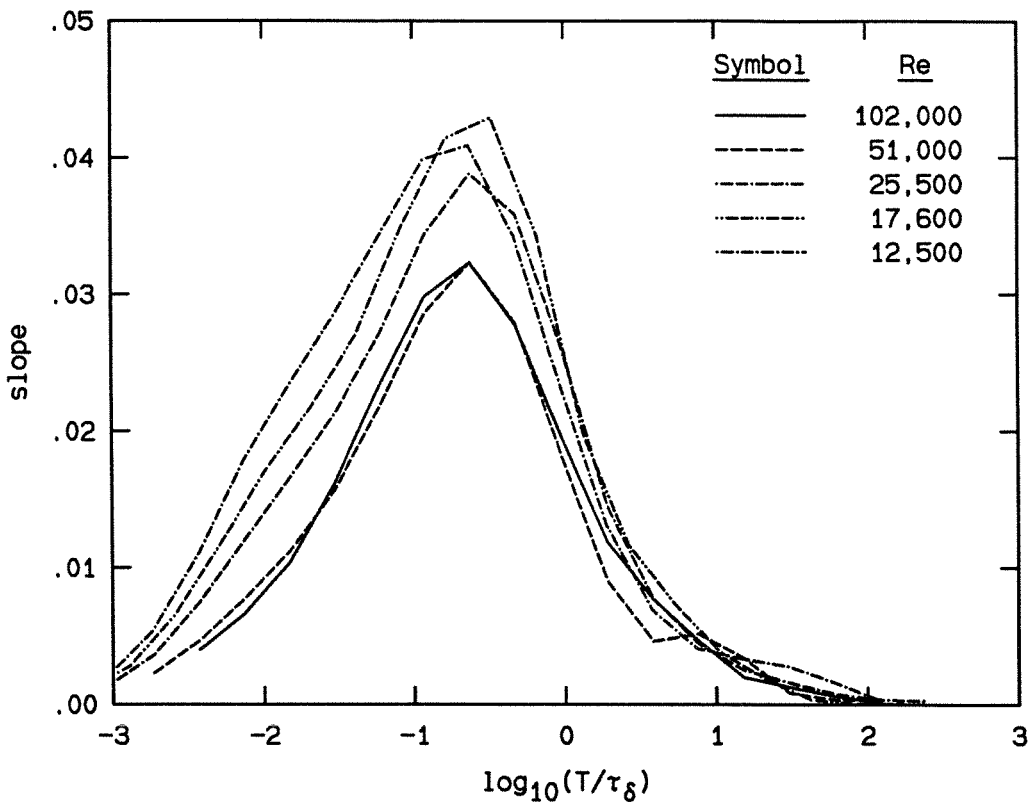


Fig. 3.15 Slopes of unnormalized versions of curves in Fig. 3.13, similar to Fig. 3.14.

version of Fig.3.13 are displayed in Fig. 3.15. It is apparent that the greatest contribution to the variance is made by scales of roughly $1/5$ of the large scale. The variations with Reynolds number are the subject of discussion in Chapter 4, but it is clear, and perhaps somewhat surprising, that the variance is produced over a relatively narrower range of scales as the Reynolds number is *increased*.

3.5 Model of large-scale structures

Returning to the initial topic of this chapter, a simple model was formed that uses the observation of ramps in the concentration traces and addresses the issue of the variance of the concentration.

In this model, the large-scale structures consist of uniform concentration within each structure, and approximate them as spherical objects, roughly tangent to the cone of the jet (Fig. 3.16). Such a picture is made plausible by, in addition to the present work, laser-induced fluorescence jet photographs taken at GALCIT (e.g., Dimotakis, et al. 1983), and is a primitive version of the homogeneous reactor of Broadwell (e.g., Broadwell & Mungal 1991).

In order to maintain the behavior in which the mean jet concentration decays inversely with axial location, each homogeneous large-scale structure assumes the correct concentration as dictated by the location of its center. Sitting at a fixed point on the centerline, an observer sees a locally decreasing concentration as a structure passes, followed by a sudden jump to a higher value upon the arrival of the next, and the pattern repeats in a periodic manner. The resulting concentration trace is therefore a series of identical ramps. The variation of velocity of the structure, and the resulting curvature in the time traces, is neglected.

The question to be addressed is: to what extent *could* the Lagrangian decay of the concentration in the structures, required by the model just described, account for the observed variance? If the remainder of the variance is ascribed to a simple Eulerian variation across each structure, relaxing the spatial homogeneity condition, how much of a variation is required to account for the observed values? Recall that it was shown above that the variance production seems to peak around $\tau_\delta/5$, and the majority of the production appears to occur in the scales between a little less than $\tau_\delta/10$ and τ_δ , large enough to regard the variance as dominated by the large scales.

From the geometry, it was calculated that the concentration seen at a point, from when a structure first arrives to when it leaves, would change by a factor of approximately 0.66. Neglecting the deceleration of the structure, this implies the

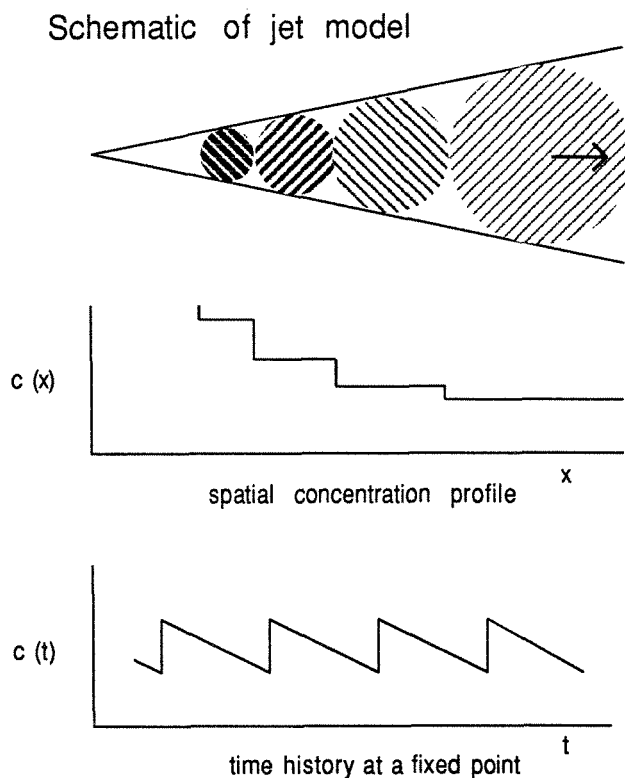


Fig. 3.16 Schematic of jet model, with sample traces of both $c(t)$ at a fixed point and $c(x)$ at a fixed time.

local concentration, as described by the model, varies in a ramp-like fashion from about 1.2 to 0.8 times the local mean.

Next, the amplitude of the ramps in the model required to produce the observed variance is estimated. The variance of the ramp model was calculated for ramps with a mean value of 1.0 and a peak value of $1 + A$ (with a corresponding minimum value $1 - A$), and found to be $A^2/3$. For an observed variance of 0.048 (the approximate minimum value measured in the current work), the amplitude of A is 0.38. Thus, to account for the observed variance with a ramp model, the concentration would have to range at least from 0.62 to 1.38 of the local mean, and the Lagrangian effect, estimated above to produce a range of 0.8 to 1.2, is

only be able to account for roughly *half* of the concentration fluctuation required to yield the observed variance. Therefore, in the ramp model, a spatial variation is required across the large-scale structures, with the higher concentration located at the downstream end, to accurately reproduce the measured variance. This is in agreement with experimental observations, particularly Dahm & Dimotakis' (1984) and Dahm's (1985) images of flame-length fluctuations, as mentioned earlier, in which the structures are seen to burn out from the rear.

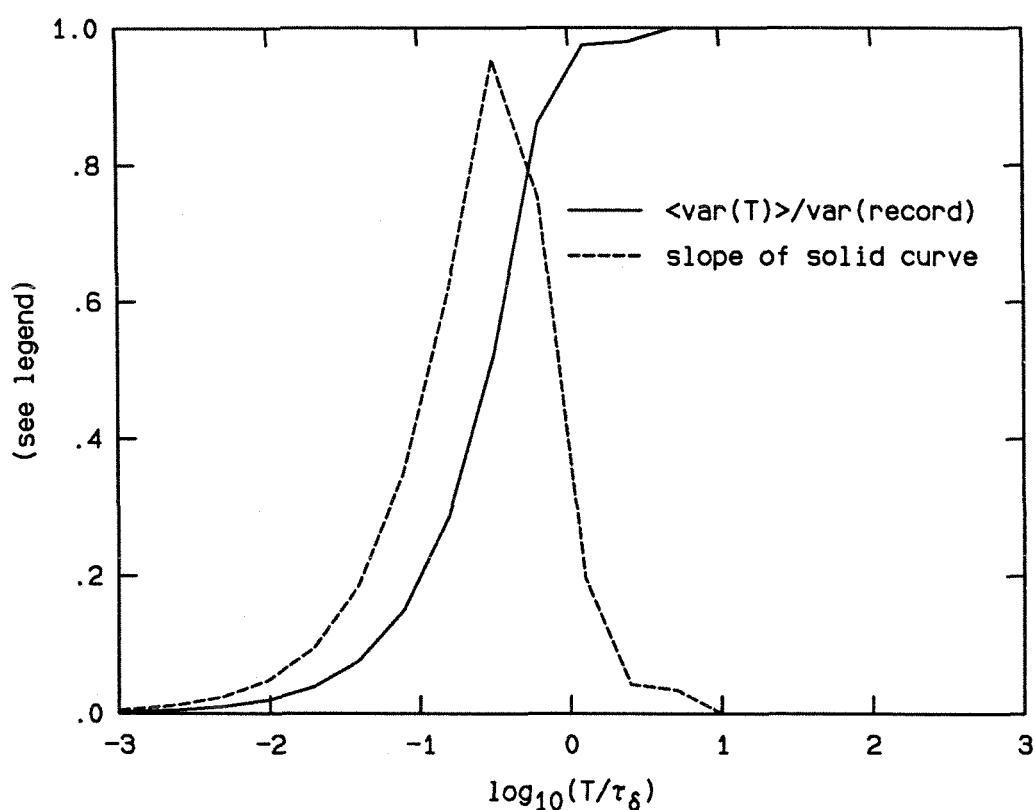


Fig. 3.17 Behavior of the variance of artificial ramps with $\bar{c} = 1.0$ and $c' = 0.2$.

Finally, the behavior of the calculations displayed in Figs. 3.13–3.15 was explored using the ramp model. A program was written to generate a record of ramps with a mean value of 1.0 and c' of 0.2 (corresponding to a variance of 0.04). Particular care was given to the construction of the record. Since the program which

processes the data to obtain Fig. 3.13 relies on powers of 2 in its logic, the ramps were constructed to contain 3^8 points per large scale, incommensurate with the program's scaling. It was suspected that phase effects of the structures produce a shift in the location of the peak of Fig. 3.14, even for records composed of structures exactly τ_δ long. In other words, there is a large difference in the variance of an interval which includes the large jump between ramps and one which does not. The results are displayed in Fig. 3.17. It is clear that there *are* phase effects, since the peak occurs at about $\tau_\delta = 0.5$, rather than 1.0. If the ramp consisted of an exact power of 2 number of points, and the starting point of the first interval was always aligned with the discontinuity in the ramp, it can be derived that the normalized, averaged variance as a function of τ would behave like $(T/\tau_\delta)^2$. At $\tau = 1.0$, it would assume the value 1.0, and since every successively longer record would consist of an integral number of large scales, would remain at 1.0. If the first interval is moved slightly to straddle the discontinuous jump, it would yield a much greater contribution to the average, while all other intervals on the smooth ramp would contribute as before. To extract the correct result, the various starting locations need to be taken into account, or randomness in the data must be counted upon to, in effect, vary them for us.

The last result reinforces the importance of the large scales in the behavior of the variance. The leading edge (or *fronts*) of the structures, that often appear as a dip in the concentration trace, followed by a very steep, very large rise, dominate the overall variance of the jet. This point should be kept in mind during the following discussions.

CHAPTER 4

Reynolds number effects

As documented previously for the Phase I data (Miller & Dimotakis, 1991b), the high Schmidt number, turbulent jet scalar field exhibits a strong dependence on Reynolds number, by several measures, at least for the Re range investigated. The discussion in this chapter will focus on this issue.

A brief description of the relevant fluid dynamic microscales and resolution conclusions is included from Appendix C. The jet fluid concentration pdf's are investigated, and found to vary in shape, becoming narrower with increasing Re . As a consequence, the normalized scalar variance declines with increasing Re , suggesting that the jet becomes better mixed with increasing Reynolds number. The concentration power spectra are examined, and changes with Re are described. It is shown that the decrease in the scalar variance is primarily a result of a broad decrease in the spectral power density, over the entire spectrum, with increasing Reynolds number.

The slopes of the power spectra are examined in more detail in Chapter 5, and some effects of initial conditions are outlined in Chapter 6.

4.1 Microscales and resolution

Before describing the results from these measurements, part of the discussion of microscales from Appendix C is presented.

From the definition of the Kolmogorov length scale λ_K ,

$$\lambda_K \equiv \left(\frac{\nu^3}{\varepsilon} \right)^{\frac{1}{4}}, \quad (4.1)$$

we may use the result of Friehe et al. (1971) for the kinetic energy dissipation rate ε on the centerline of a turbulent jet (cf. Dowling & Dimotakis 1990), i.e.,

$$\varepsilon = 48 \frac{u_0^3}{d} \left(\frac{x - x_0}{d} \right)^{-4}, \quad (4.2)$$

to estimate the Kolmogorov scales for these measurements as

$$\lambda_K = 0.38 (x - x_0) Re^{-3/4}. \quad (4.3)$$

The values calculated from Eq. 4.3 are tabulated in Appendix A for the various runs.

By similarity arguments, the velocity field spatial scale where the action of viscosity will become important, say, λ_ν , will be some multiple of λ_K . Normalized energy spectra are found to break from a constant power-law at a wavenumber k_ν such that $k_\nu \lambda_K \approx 1/8$ (e.g., Chapman 1979). This yields an estimate of (cf. Miller & Dimotakis 1991b)

$$\lambda_\nu = \frac{\pi}{k_\nu} \sim 25 \lambda_K, \quad (4.4)$$

i.e., to resolve the roll-off of the *velocity* spectrum, a scale ~ 25 times λ_K needs to be resolved.

While the Kolmogorov scale represents the smallest *velocity* scale in the flow, for $Sc > 1$, the smallest expected *scalar* diffusion scale λ_B is smaller yet by a factor of $Sc^{1/2}$ (Batchelor 1959), i.e.,

$$\lambda_B \equiv \frac{\lambda_K}{\sqrt{Sc}} . \quad (4.5)$$

Adopting the diffusion coefficient for fluorescein reported in Ware, et al. (1983), of $5.2 \times 10^{-6} \text{ cm}^2/\text{sec}$, the calculated Schmidt number for dilute fluorescein in water is slightly less than 1900. This implies a scalar diffusion scale

$$\lambda_D \sim 25 \lambda_B \quad (4.6)$$

that is roughly 25/43, or 0.6, times the Kolmogorov scale. Accepting this estimate, the scalar diffusion scale λ_D is resolved in most of the measurements reported here.

4.2 Behavior of the concentration pdf's

Jet centerline concentration pdf's, or normalized histograms, at $x/d = 305$, for Reynolds numbers from 3,000 to 65,000, are displayed in Fig. 4.1. The concentration has been scaled by the (local) mean. These pdf's are compiled into 125 bins over the full range, or 25 bins per interval. The bin widths were chosen to reflect the (amplitude) dynamic range of the data of (roughly) 100:1. Straight lines connect the centers of each histogram level. These records consist of approximately 35 large-scale structures each, independently of Re , and the rough appearance of the pdf's is a result of statistical uncertainties, as discussed in Chapter 3.

Several features are evident in Fig. 4.1. The pdf's become narrower and, as required to maintain their normalization, taller, with increasing Reynolds number. For $Re = 3,000$, there is a considerable tail at the large values. This tail actually

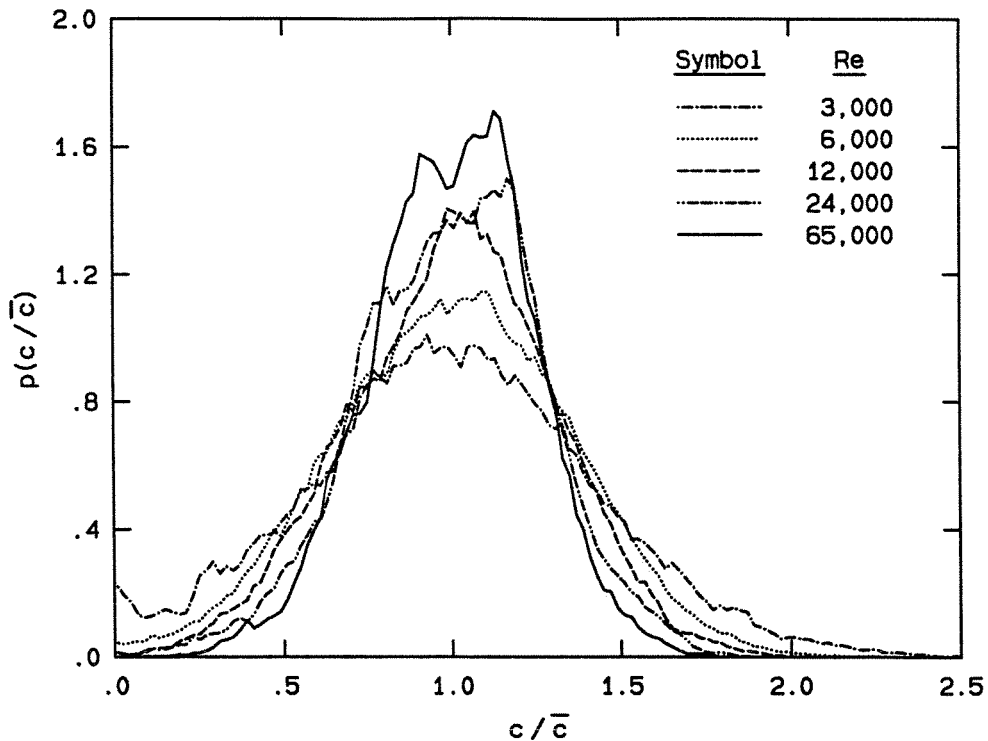


Fig. 4.1 Jet centerline concentration pdf's at $x/d = 305$, for varying Reynolds numbers.

extends beyond the plotted range to a value of 2.75 times the mean (including .04% of the area of the pdf in its unplotsed portion). None of the other pdf's extend beyond 2.5 times the mean. At the low concentration values, there is an accumulation of probability for the lowest Re , indicating the presence of unmixed reservoir fluid on the jet axis. As the Reynolds number is increased, the proportional amount of unmixed fluid decreases, until there is virtually none at the highest Re .

It should be emphasized that the general behavior of Fig. 4.1 is *not* the result of a degradation of resolution with increasing Reynolds number (see Appendix C). For comparison, Fig. 4.2 shows the pdf's of two runs at similar Re , but different x/d . Note that tripling the x/d results in a tripling of the microscales of the flow (cf. Appendix C), proportionally relaxing the resolution requirements. The two pdf's agree well, if it is recognized that the $x/d = 100$ run contains over 470 large-scale

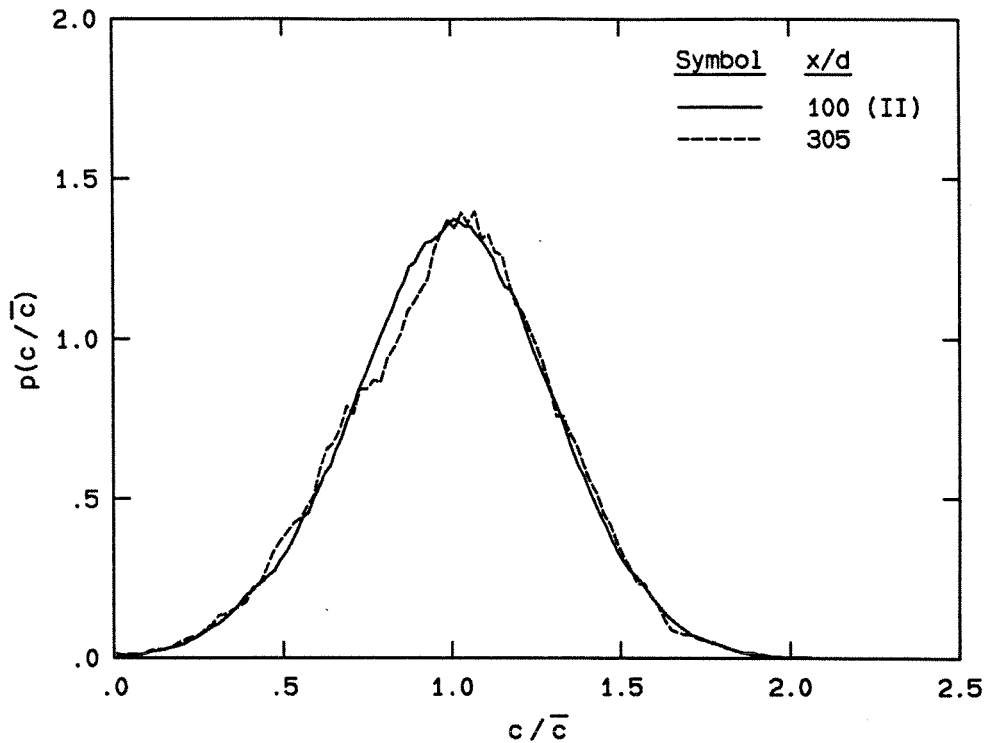


Fig. 4.2 Jet centerline concentration pdf's for $Re = 12,000$, $x/d = 305$, and $Re = 12,500$, $x/d = 100$.

structures, while the $x/d = 305$ run captured about 35.

As the Reynolds number is increased further, the pdf's continue to become more narrow, until, at the highest Re , there is little change (Fig. 4.3). A caveat should be added here that, at Reynolds numbers of 71,000 and 102,000, acoustic flow noise was generated in the vicinity of the jet nozzle. As described in Appendix B, this noise may have stemmed from cavitation, and suggests that a mechanism may have been at work which could have influenced the flow. In Fig. 4.3, for example, the pdf at $Re = 102,000$ is actually a bit shorter and wider than the pdf at 51,000. Such differences may be traceable to the same process which generated the sound.

The overall picture formed by Figs. 4.1 and 4.3 is that the jet concentration pdf's become narrower with increasing Reynolds number, suggesting a more ho-

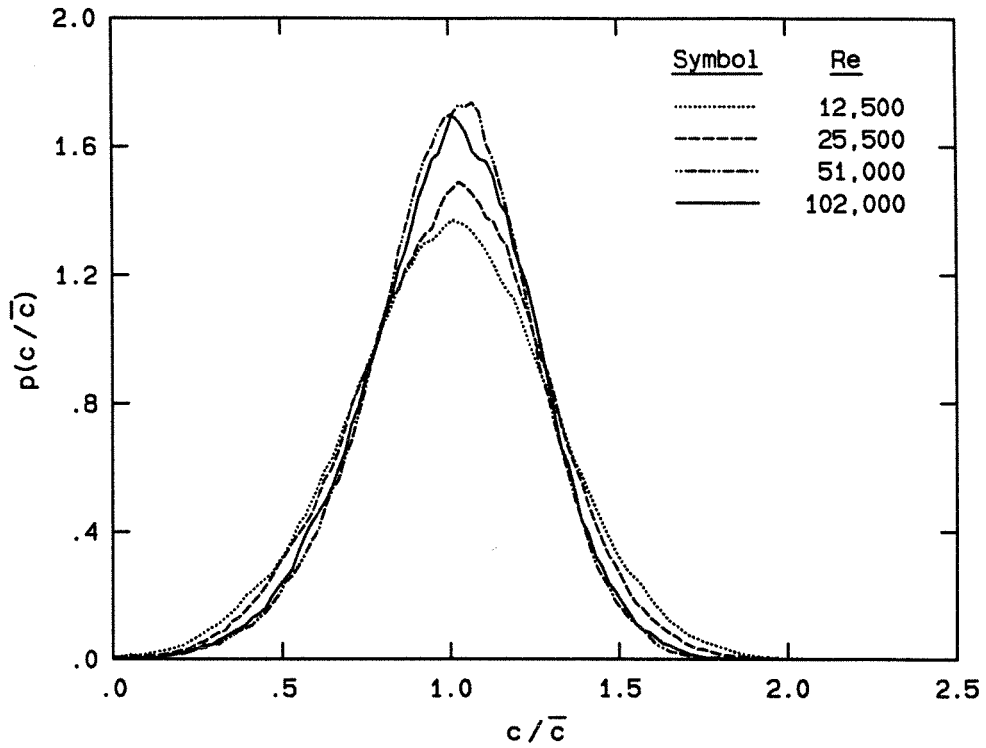


Fig. 4.3 Jet centerline concentration pdf for varying Re at $x/d = 100$.

mogeneous, or better mixed, jet. A quantitative measure of the width of the pdf is obtained from its second moment, or variance, which is examined in the next section.

4.3 Scalar variance results

The scalar, or concentration, variance is defined as:

$$\text{var}\{c\} = \overline{c'^2} \equiv \int_0^{c_{\max}} (c - \bar{c})^2 p(c) dc, \quad (4.7)$$

(cf. Miller & Dimotakis 1991b), where c_{\max} is the highest concentration present and $p(c)$ is the probability density function of c , normalized such that

$$\int_0^{c_{\max}} p(c) dc = 1. \quad (4.8)$$

Throughout this work, the variance will typically be nondimensionalized by the mean squared, \bar{c}^2 . The resulting quantity is a measure of the width of the distribution $p(c/\bar{c})$. The concentration variance was calculated from the jet concentration data, taken at three axial locations, over a range of Reynolds numbers. The results are shown in Fig. 4.4.

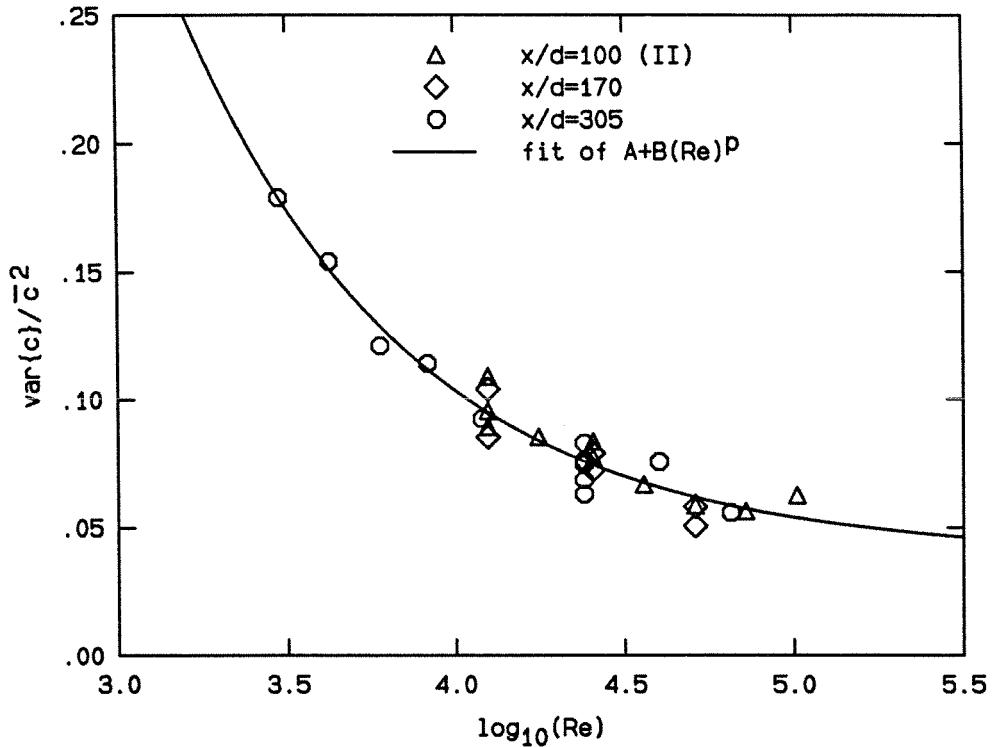


Fig. 4.4 Normalized jet centerline concentration variance for varying Re , at $x/d = 100$, 170 , and 305 . Line is best fit with $A + B Re^p$. The determined parameters are $A = 0.039$, $B = 24.8$, and $p = 0.647$.

The points are fit with a function that was chosen for its simplicity, ability to approximate the observed behavior, and capability to either approach a nonzero asymptotic value (or zero, if it were indicated). The fit does suggest that the points are approaching a constant value with increasing Reynolds number, and the determined asymptote, 0.039 , is in good agreement with the finding from the analysis of the Phase I data of 0.04 (Miller & Dimotakis 1991b), as discussed further

in Chapter 6.

The observed decrease of the concentration variance (or, equivalently, the rms) is a substantial effect. The jet becomes better mixed, apparently approaching an asymptotic, high Reynolds number value of the variance and a similarity in the concentration pdf's. *In a span of 1.5 decades in Reynolds number, the variance is reduced by over 70%.* In addition, the measurements at three different axial locations all exhibit the same behavior, indicating that there is specific similarity of this variable with x/d . Bear in mind that the decline is not from deteriorating resolution, as discussed briefly above, in Appendix C, and in Miller & Dimotakis (1991b).

The manner in which the change in the variance arises, the scales which contribute, and clues to the possible mechanisms which may cause the effect are found in the power spectrum of the concentration.

4.4 Concentration power spectra

The concentration power spectrum $E_c(f\tau_\delta)$ is normalized here to the variance of the scalar fluctuations, i.e.,

$$\overline{c'^2} = 2 \int_0^\infty \frac{E_c(f\tau_\delta)}{\tau_\delta} d(f\tau_\delta) , \quad (4.9)$$

where f is the (linear) frequency, and has been nondimensionalized by the large-scale time τ_δ .

These spectra are compensated as described in Appendix C, and are fully resolved to $\log_{10}(f\tau_\delta) \approx 2.6$ at $x/d = 100$ and $\log_{10}(f\tau_\delta) \approx 2.8$ at $x/d = 305$, beyond which the data are SNR limited. Starting at the low frequencies, the first

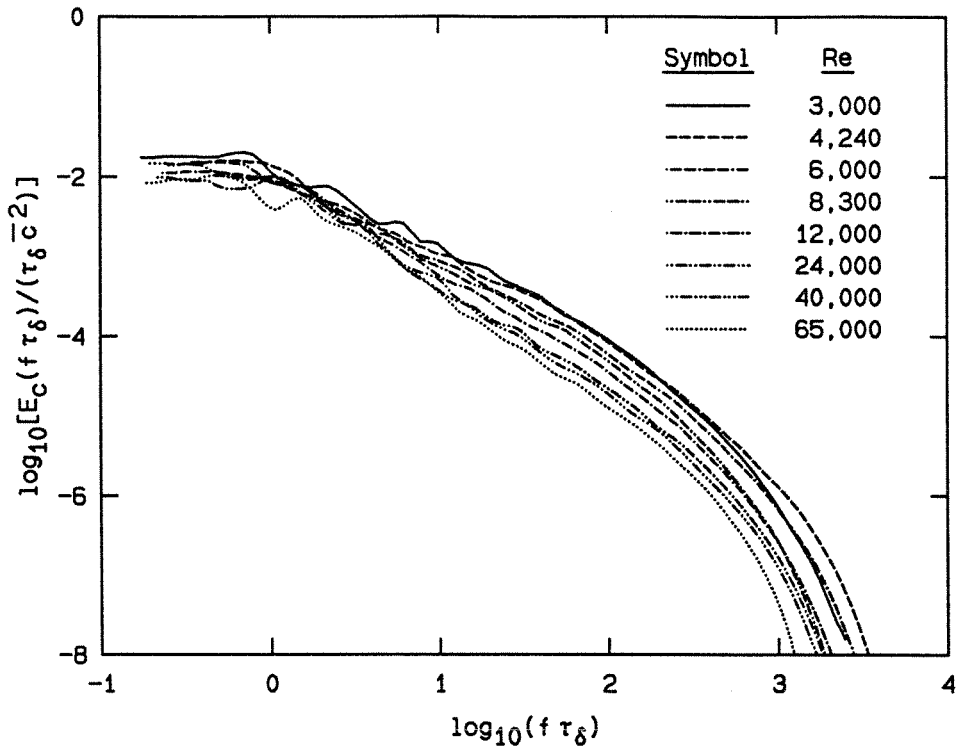


Fig. 4.5 Jet centerline concentration power spectra for varying Re at $x/d = 305$ (compensated as described in Appendix C).

feature encountered on the spectrum is an approximately constant level, and then a knee in the curve at $\log_{10}(f\tau_\delta)$ that corresponds to the large-scale passage frequency. While there are some bumps from the statistics of the records, there is a trend toward lower levels in this constant region with increasing Reynolds number. The constant low-frequency behavior of the spectrum is consistent with the fact that the power spectral density at zero frequency is equivalent to the integral of the autocorrelation function of c' , which is normally non-zero.

As was noted about Eq. 4.9, the scalar variance is also equal to the area under the spectrum. To make this more evident when plotting the spectra in logarithmic coordinates, power spectra are sometimes multiplied by the frequency (or wavenumber, k), to yield the contribution to the variance at each scale. This is equivalent to adding 1 everywhere to the slope. It is clear the result has a local maximum

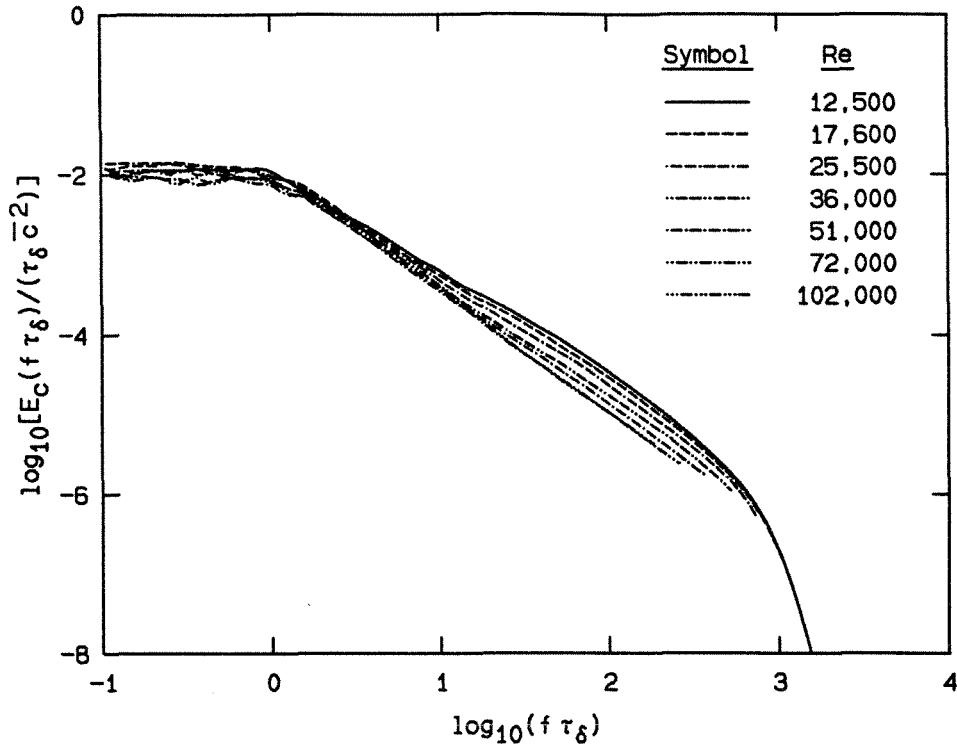


Fig. 4.6 Jet centerline concentration power spectra for varying Re at $x/d = 100$ (compensated as described in Appendix C).

wherever the slope of the spectrum is equal to -1 , and a global maximum if no part of the spectrum extends beyond a line of -1 slope passing through the point of interest.

All of the spectra from Figs. 4.5 and 4.6 are plotted together in Fig. 4.7, with reference lines for comparison. The entire extent of all the displayed spectra is resolved. It can be seen that at the lower Reynolds number, spectra corresponding to the higher lines, have slopes close to -1 for quite a range of frequencies. At higher Re , a break-point develops, and the spectrum decreases faster than -1 before the break-point. By sighting along the reference $-5/3$ slope, there is a small but clear difference between the developing inertial slopes and $-5/3$. This issue will be addressed further in Chapter 5. One implication of this increase in the slopes is that, according to the transformation described above, the contribution to the

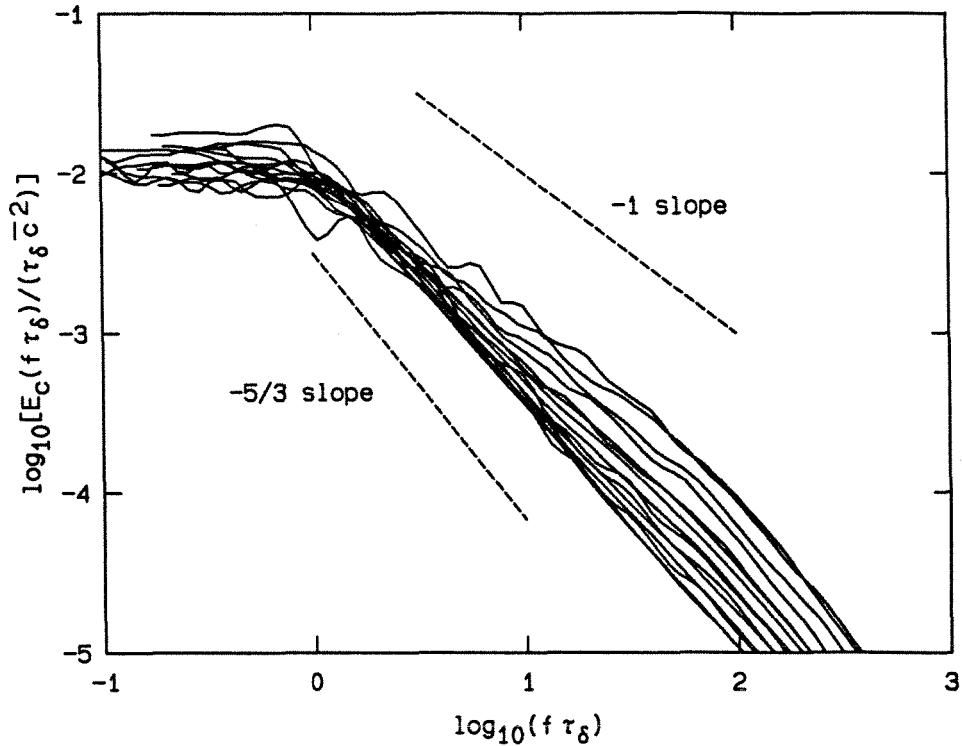


Fig. 4.7 Composite plot of all of the spectra shown in Figs. 4.5 and 4.6. Reference slopes are shown for Kolmogorov and Batchelor scaling.

variance is broadly distributed over scales at the lower Reynolds numbers, but the distribution narrows with increasing Re . The maximum contribution is associated with times close to, but slightly less than, the large-scale time. This conclusion is equivalent to the results in Figs. 3.14 and 3.15.

Spectra from three widely spaced Reynolds numbers are plotted in Fig. 4.8. Note that there is a significant vertical shift, across the entire spectrum, between the three cases. It is concluded that the decrease of the variance with increasing Reynolds number (Fig. 4.4) is primarily from this broad shift, rather than the effect of increasing slopes in the inertial range. This is also consistent with the earlier results. Not only do the peaks in Fig. 3.14 get narrower with increasing Re , in accord with the increasing inertial slopes, but the peak heights in Fig. 3.15 get shorter, reflecting the lower total variance (also exhibited in Fig. 4.4) from the

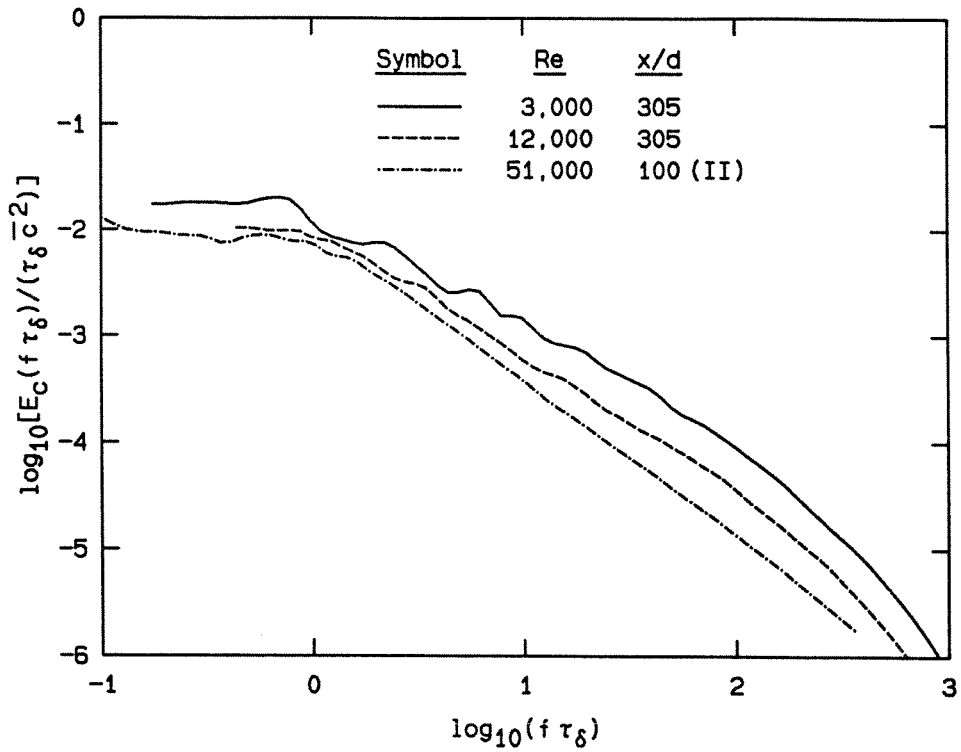


Fig. 4.8 Spectra at three widely separated Reynolds numbers.

broadly lower spectral levels.

The mechanism behind the change in the spectra has not been determined. However, as discussed in Chapter 6, similar effects are observed from the influence of initial conditions, specifically, fluid disturbance levels in the jet plenum and near the nozzle exit. See that chapter for additional discussion.

CHAPTER 5

Spectral slopes

While this chapter might more properly be called “Slopes of the spectra”, the term “spectral slopes” will be used throughout to designate the logarithmic derivative of the various power spectra $E_c(f\tau_\delta)$, i.e., the slope of these spectra on the log-log plots. The spectral slopes are of interest because, in accord with the objectives of identifying Schmidt number and Reynolds number effects, the concentration power spectrum is a powerful diagnostic of the behavior of the scalar field, and the spectral slopes are sensitive to changes in the spectra. Additionally, turbulence models often predict particular behavior of the spectral slopes, and the experimental results may be used to assess such models.

The average spectral slopes, between the knee frequency and the roll-off, are found to steepen with increasing Reynolds number, from values of about -1 at $Re = 3,000$ to approximately -1.5 at $Re = 102,000$. The average slopes in the inviscid range are also examined, and they similarly steepen with Re . Above $Re \approx 35,000$, the inviscid slopes have values close to 1.5 . The local spectral slopes are examined in more detail. The results indicate that the slopes display specific similarity between different x/d locations.

The general spectral behavior, starting at the lowest frequencies and moving toward higher ones, may be approximated as follows: a constant level, a knee at the large-scale passage time, a region of roughly constant negative slope, a break-point leading to a region of less-steep slope, and a roll-off at the highest frequencies (e.g.,

Figs. 4.5 and 4.6). No constant -1 (Batchelor 1959) spectral slope region is present. Rather, the spectra at viscous scales are found to be *log-normal*.

The scaling of the break-point location at the beginning of the log-normal region behaves like $Re^{3/4}$, i.e., Kolmogorov scaling, but the magnitude is found to be about 80–85 times longer than the calculated λ_K . SNR resolution limitations dominate the behavior of the spectral slopes in the vicinity of the roll-off location, but from the lowest Re results, it appears that the log-normal behavior may extend further than $Sc^{1/2}$ from the break-points.

5.1 Average slopes

To further examine the development of the spectra with Re , the average slope values were determined numerically, by fitting a straight line from the knee frequency to the roll-off point, for a wide variety of runs (Fig. 5.1). The results display an increase in the average slope, from values in the vicinity of -1 at the lowest Re , toward values near $5/3$ at the highest. The agreement between the Phase II $x/d = 100$ and $x/d = 305$ results is interpreted as evidence that the slopes have specific similarity, i.e., are similar at different x/d locations. The different behavior of some of the other x/d results is partly ascribed to statistical uncertainties, partly to uncertainties in the selection of the averaging region, and partly to effects of initial conditions, as discussed in Chapter 6. It is interesting to note that, even at a Reynolds number as high as 102,000, these average slopes have neither reached an asymptotic value nor attained a slope of $-5/3$.

Beyond the knee frequency, the spectra at the lowest Re decline with an almost constant slope, until they finally roll off at high frequencies. With increasing Re , however, the spectra begin to develop a break-point (dividing a steeper slope region

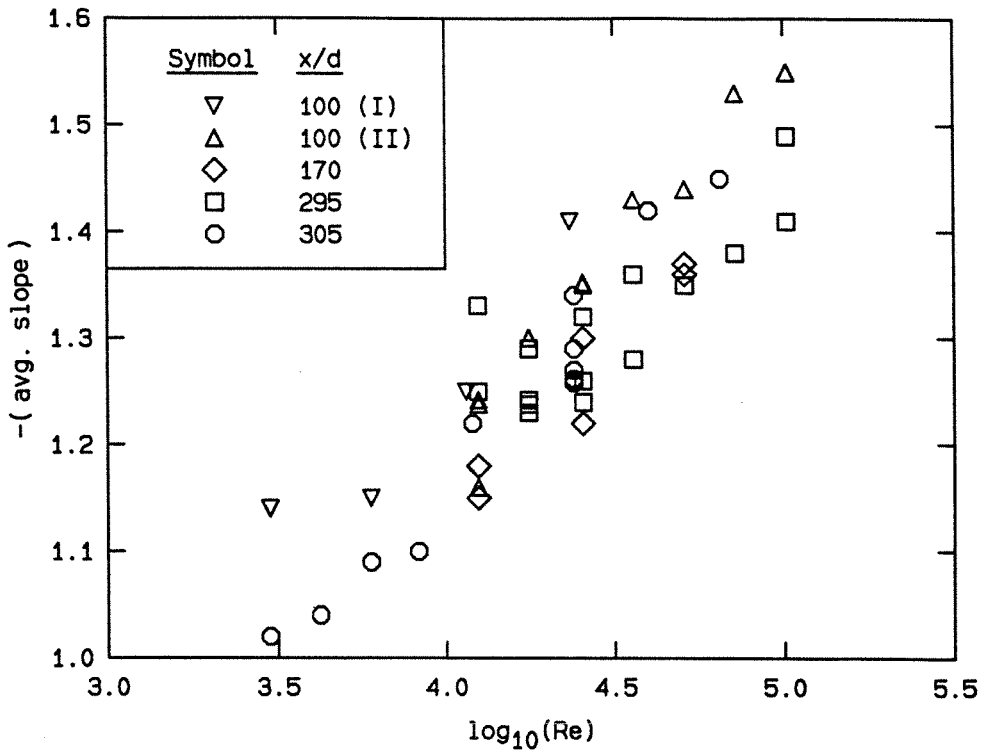


Fig. 5.1 Average spectral slopes, between the knee frequency to the roll-off, under many conditions.

at lower frequencies from a less steep portion at the higher frequencies), which moves away from the knee with increasing Re . In the context of classical turbulence theories, this behavior could be interpreted as the development of an inviscid range between the outer (large) scales of the flow, and the Kolmogorov (1941) scale (see, for example, Monin & Yaglom 1975). This slope is expected to be close to $-5/3$, to the extent that homogeneous, isotropic turbulence theories may be appropriate in this situation.

The slow approach to an asymptotic value in Fig. 5.1 is, in part, because the average slopes include the regions both before and after the break-point. In Figs. 4.5 and 4.6, it is apparent that the inviscid range is establishing itself by $Re \sim 12,000$, or so, and it is the inviscid range slope which might be expected to approach $-5/3$ (e.g., as reported by Clay 1973 for a hot air jet).

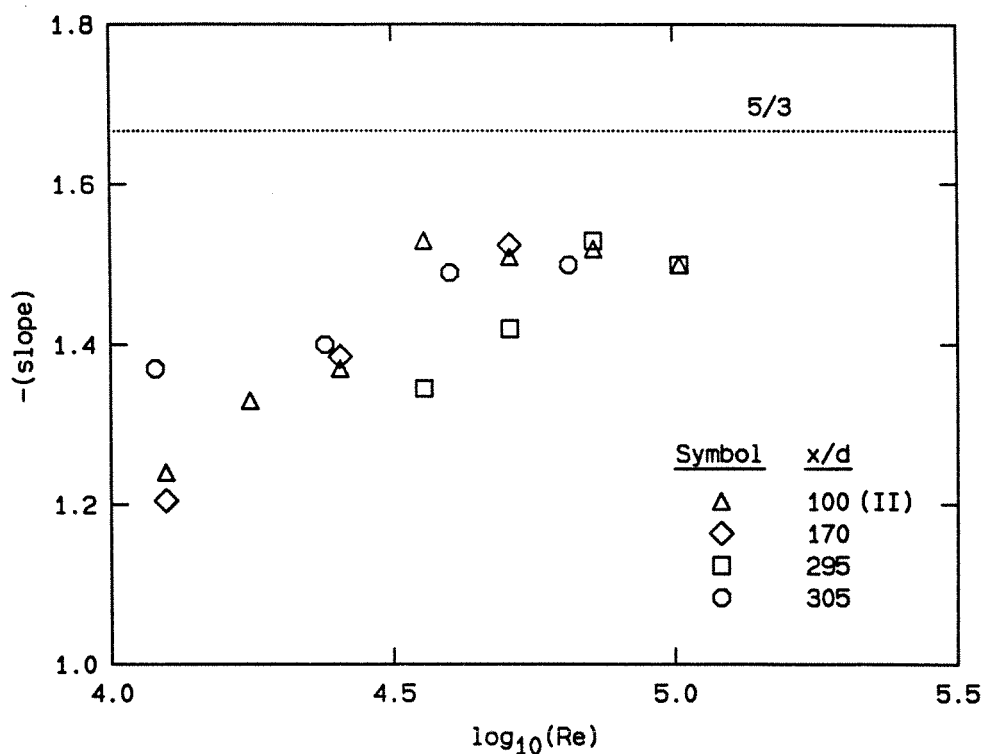


Fig. 5.2 Average spectral slopes of the steep portion of the inviscid range.

The inviscid slopes were estimated from the higher Reynolds number spectra by fitting a straight line to their steeper portion, at frequencies just below the break-point. The result is displayed in Fig. 5.2. Some of the points are averages of pairs of values, from runs at the same Re . The slope values increase with increasing Reynolds number. Three points seem to depart from the general behavior. The low squares ($Re = 25,500$ and $51,000$) were “quick runs”, with higher plenum disturbance levels (see Chapter 6). The high circle ($Re = 12,000$, $x/d = 305$) also had a moderately high slope in Fig. 5.1, but nothing else special was noticed about the run. These slopes are difficult to extract in general, and should be viewed with uncertainties perhaps on the order of ± 0.05 . This uncertainty is from the difficulty of determining the break-point location, the short extent of the inviscid range at the lower Re , and particularly from the oscillations in the spectra which will become more evident in the following sections.

5.2 Spectral slope behavior

The spectral slopes were computed directly from the compensated spectra, as a function of frequency, using numerical three-point differentiation of the one-third octave averaged spectra (as described in Appendix B). An example of a concentration spectrum and the corresponding spectral slope curve is shown in Fig. 5.3.

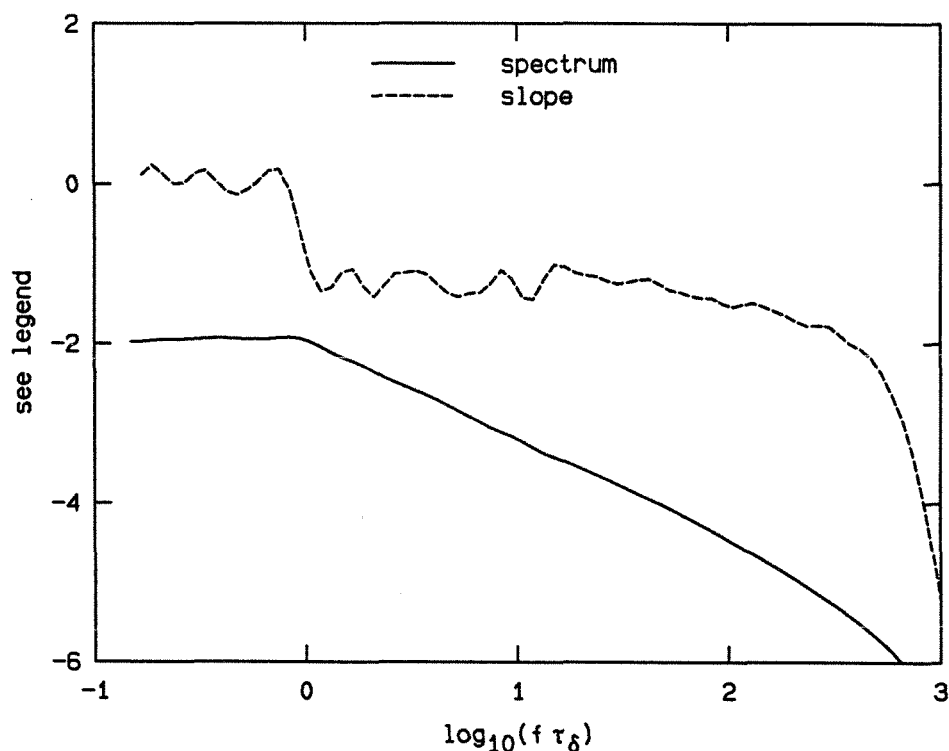


Fig. 5.3 Spectrum at $Re = 12,500$ ($x/d = 100$) and its derivative. The vertical scale for the spectrum is the same as in Figs. 4.5 and 4.6, and the slope is measured in the same coordinates.

The slope oscillates about a value of ~ 0 until the large-scale passage frequency, where it drops to a value of about -1.25 . This region, between $\log_{10}(f\tau_\delta) = 0$ and 1.18 , is interpreted as the inviscid range of the spectrum. At a value of $\log_{10}(f\tau_\delta) = 1.18$, the oscillations decrease, and the curve assumes an approximately constant slope. This is concluded to be a distinct region, the beginning of which will be called

the break-point, since the spectrum appears to undergo a change in the character of its slope at that location. Finally, the frequency at which the slope begins to drop off sharply, at $\log_{10}(f\tau_\delta) \approx 2.6$, will be called the roll-off point.

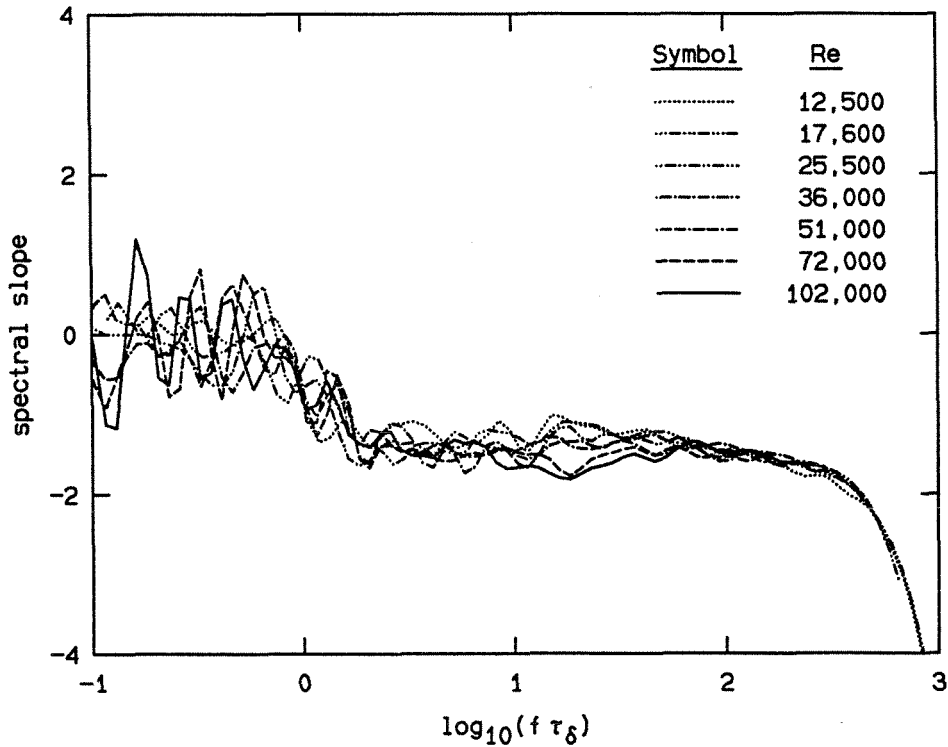


Fig. 5.4 Ensemble of slope plots at $x/d = 100$.

An ensemble of slope plots, over a wide range of Reynolds numbers at $x/d = 100$, is displayed in Fig. 5.4. All of the spectra at $x/d = 100$ and 300 used in this chapter were compensated as described in Appendix C. Another set of curves from $x/d = 305$ are included as Fig. 5.5. The oscillations in the slopes are rather pronounced. It should be noted that the curves in Fig. 5.4 were calculated from concentration records containing 400–500 large-scale structure passages, while the runs in Fig. 5.5 captured about 35. It was suspected that the different statistical uncertainties accounted for the large difference in the amplitudes of the slope oscillations between Fig. 5.4 and Fig. 5.5.

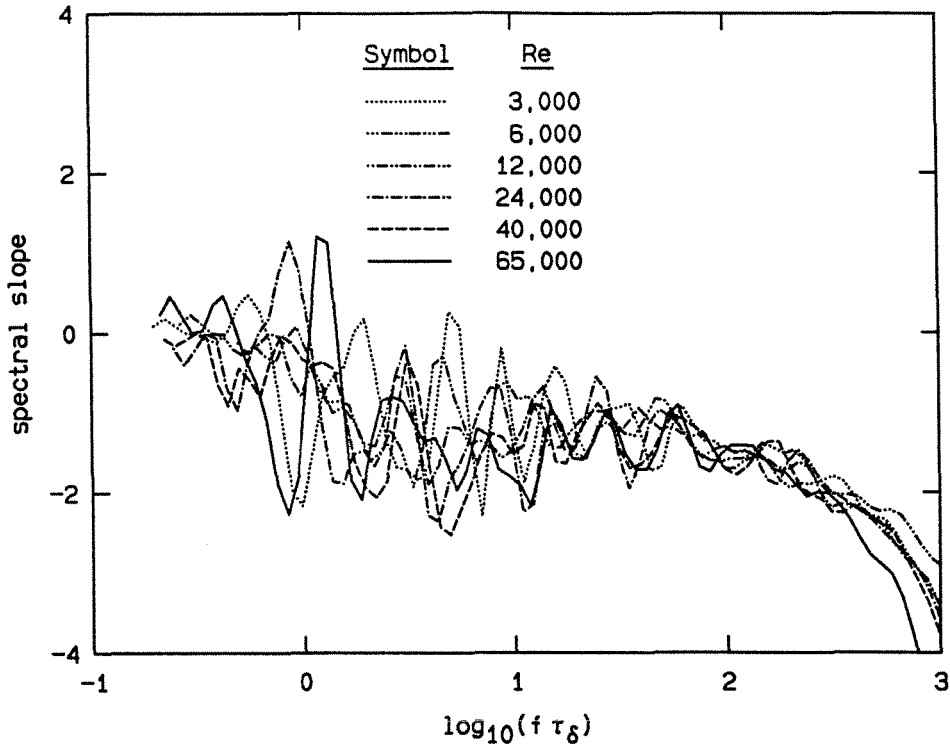


Fig. 5.5 Ensemble of slope plots at $x/d = 305$.

Several comparisons were made to address questions about the oscillations in the slope results. Slopes of two runs at the same x/d and same Re are displayed in Fig. 5.6. Note that the bumps move, but the break-point and roll-off locations remain the same. The fact that the bumps move, under the same conditions, suggests that they are not caused by fixed frequencies in the flow. As another test, thirds of a record were processed individually and compared both to each other and to the result from the entire record (Fig. 5.7). The preceding strongly suggests that the oscillations of Figs. 5.6 and 5.7 are the consequence of statistical nonconvergence.

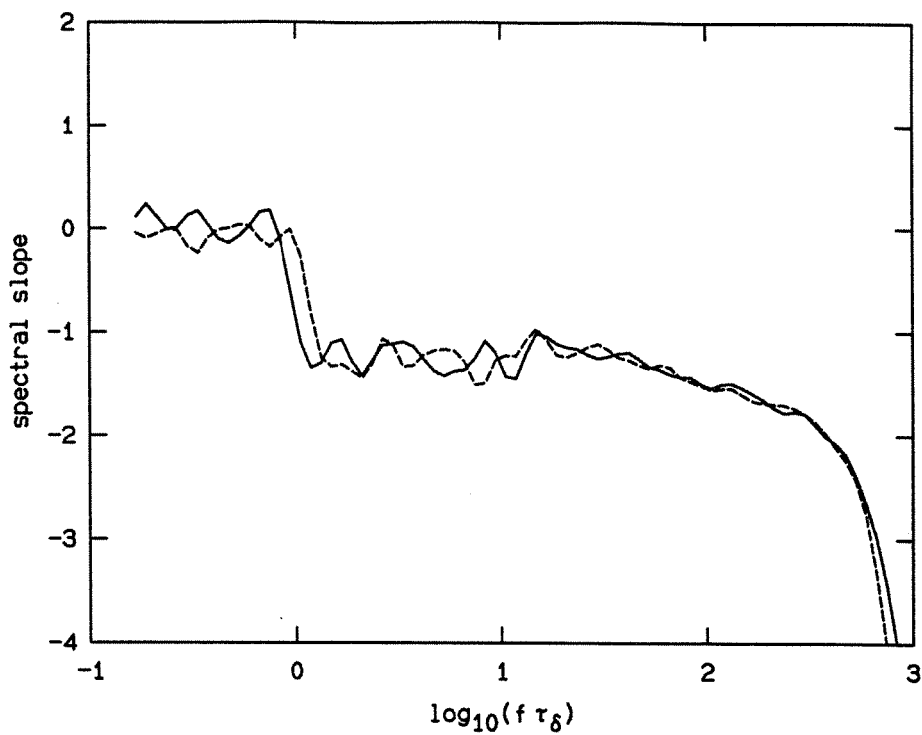


Fig. 5.6 Two cases under identical conditions ($Re = 12,500$, $x/d = 100$).

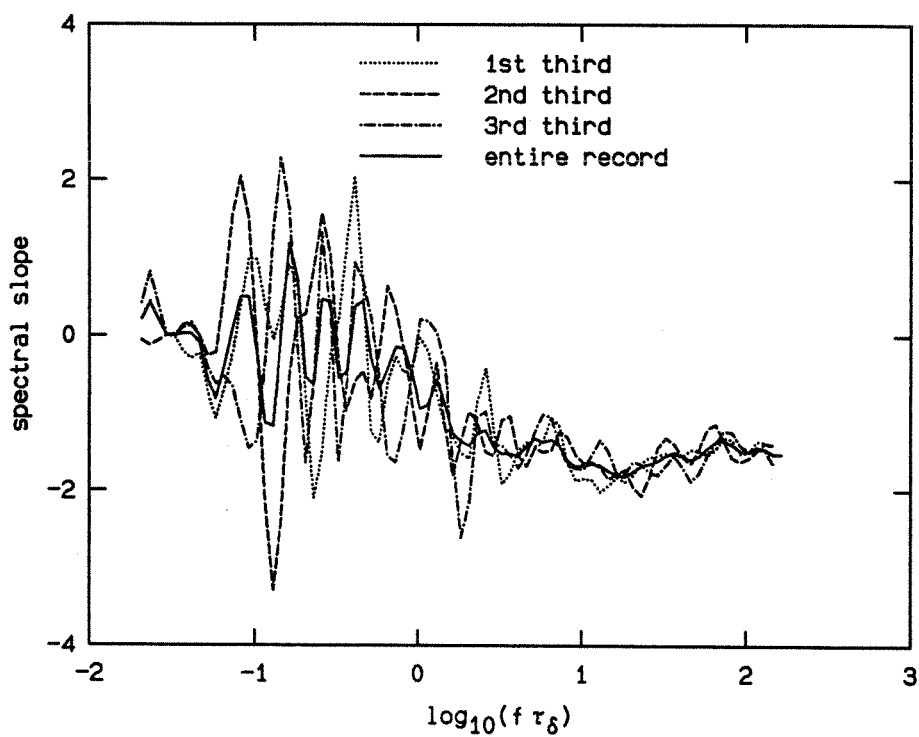


Fig. 5.7 Effect of analyzing partial records ($Re = 102,000$, $x/d = 100$).

5.3 The log-normal range and the break-point

For scales between the viscous diffusion (Kolmogorov) scale and the smaller species diffusion (Batchelor) scale, Batchelor (1959) predicted that another, *viscous-convective*, range would be present at high Schmidt numbers between λ_K and λ_B , with a slope of -1 . The extent of this range should be independent of Re , since $\lambda_B \approx \lambda_K/\sqrt{Sc}$ (see Appendix C). No such constant -1 slope is observed. Additionally, theoretical difficulties exist with this proposal (Dimotakis & Miller 1990). Nevertheless, it is clear that the extra length scale provided by the Batchelor (species diffusion) scale might cause a change in the spectral behavior in the vicinity of λ_K (or λ_ν), extending to some multiple of λ_B .

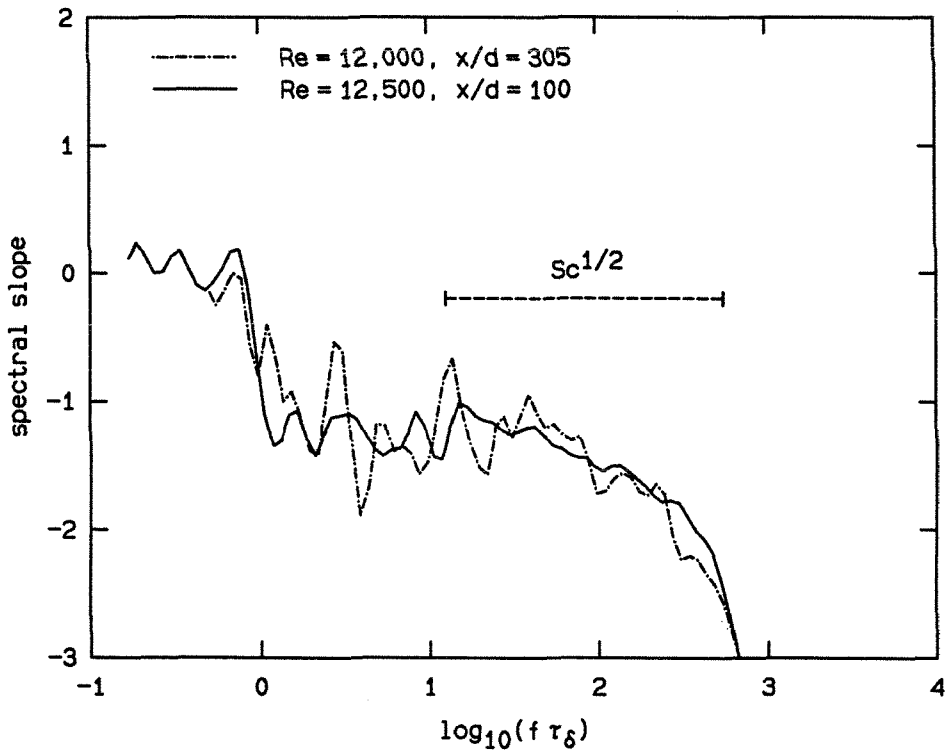


Fig. 5.8 Comparison of $x/d = 100$ and $x/d = 305$ results at $Re \approx 12,000$.

Returning to Fig. 5.6, it is concluded that the region between about $\log_{10}(f\tau_\delta) = 1.18$ and 2.6 , at $Re = 12,500$, displays a considerably different be-

havior than the inviscid range. Note that the oscillations in the slope values are of almost constant amplitude at the lower frequencies, but appear to become considerably smaller at the start of this region. Rather than an influence of improving statistics, which would be associated with a gradual decline, the sharp change is interpreted as the effect of viscosity damping out velocity fluctuations, thereby affecting the scalar field.

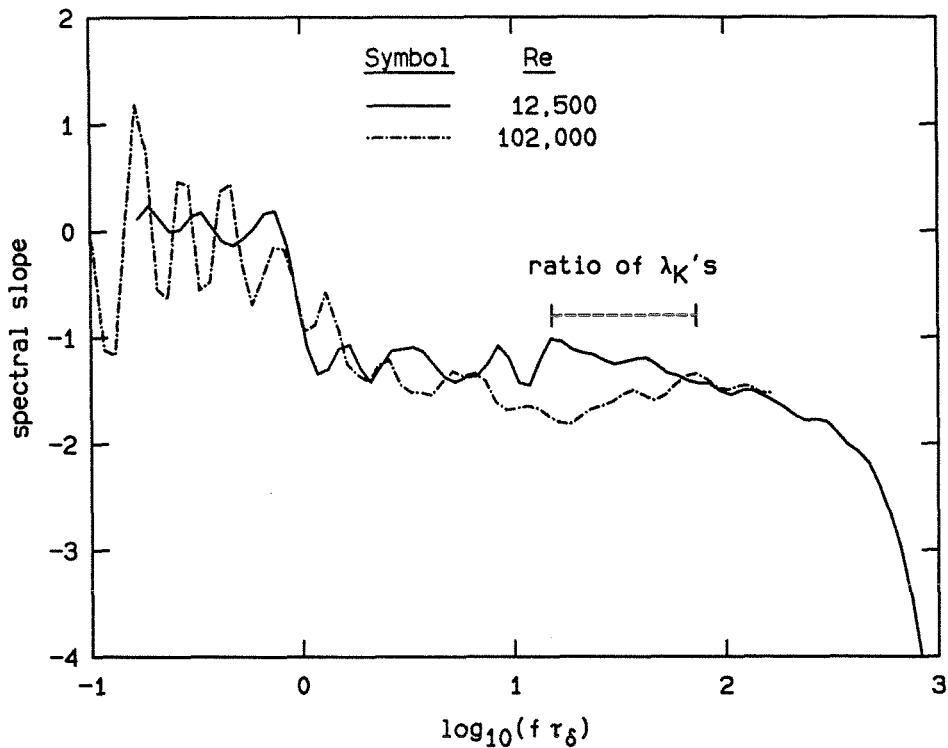


Fig. 5.9 Demonstration that break-point location scales with Kolmogorov scale ($x/d = 100$).

This different region seems to exhibit a constant derivative on the slope curves, implying that the spectrum is parabolic when plotted in log-log coordinates, and *log-normal* in linear coordinates. For this reason, it is referred to as the log-normal range. This behavior is evident in Fig. 5.4, and, less clearly, in Fig. 5.5. A comparison between the $x/d = 100$ and $x/d = 305$ results at $Re \approx 12,000$ is made in

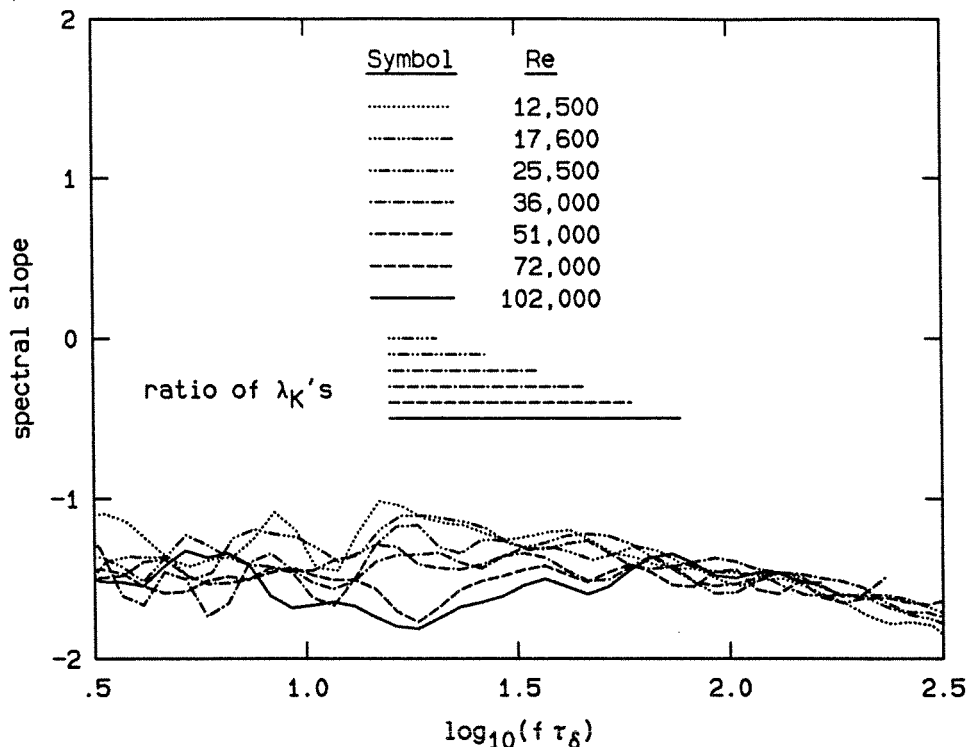


Fig. 5.10 Close-up of break-point scaling ($x/d = 100$). Line segments represent the ratio of the Kolmogorov scale at $Re = 12,500$ to the Kolmogorov scale at each of the other Re , with the same line types as in the legend.

Fig. 5.8. Within the uncertainties of the poorer statistics at $x/d = 305$, the two cases display the same behavior. The square root of the Schmidt number is included on the plot for comparison, but the agreement with the width of the log-normal range is probably coincidental, as will be discussed later.

The starting location of the log-normal range, i.e., the break-point, is consistent with Kolmogorov scaling ($f \sim Re^{3/4}$), as demonstrated by Fig. 5.9. The same comparison is made in Fig. 5.10 for a wider set of Reynolds numbers. The break-point appears as the point at which each Reynolds number's curve joins the constant slope decline, starting with the $Re = 12,500$ case at about $\log_{10}(f\tau_\delta) = 1.18$. The line segments shown represent the ratio of the Kolmogorov scale at $Re = 12,500$ to the Kolmogorov scale at each of the other Re . The alignment of the segments is

only approximate; their lengths represent the relative scaling. If the spatial scale of these break-points is estimated from the mean centerline velocity calculated from Eq. A.2, they are about 80–85 times the Kolmogorov scale calculated from Eq. C.5, or slightly more than 3 times λ_ν (Eq. C.6).

5.4 The roll-off

The span of the viscous-diffusive range is expected to be approximately $Sc^{1/2}$, as argued by Batchelor (1959). The behavior in Fig. 5.8 appears, at first, to agree quite well with this quantity. However, it should be noted that the location of the roll-off predicted by Batchelor is proportional to the (Batchelor) diffusion scale λ_B . Since λ_B is proportional to the Kolmogorov scale λ_K , the roll-off should move with Reynolds number accordingly. It is clear in Figs. 5.4 and 5.5 that the roll-off moves little, if any. The spectra of the cases which do differ slightly in Fig. 5.5 were examined, and it was determined that the early roll-off ($Re = 65,000$) had a higher-than-normal noise floor on the raw spectrum, and the late roll-off ($Re = 6,000$), a lower noise floor. It was concluded that the roll-off behavior is a result of SNR resolution limits. In the vicinity of the noise floor, the spectral slope results are sensitive to imperfections in the implementation of the Wiener filter, and the roll-offs in the spectra appear to be a result of this limitation. The behavior of the spectrum at yet higher frequencies cannot be determined at this time. However, the fact that the roll-offs in Fig. 5.5 remain fixed as the Reynolds number is decreased from 12,000 suggests that their log-normal ranges may exceed $Sc^{1/2}$ in extent, by some margin.

CHAPTER 6

The influence of disturbances

It became apparent, during the experiments described in Chapter 4, that the fluid disturbance levels, both in the jet plenum and beneath the nozzle exit, were influencing the behavior of the scalar variance. The variance values of Chapter 4 are revisited, this time considering the various changes made throughout the experiments which would affect disturbance levels, including additional runs specifically conducted for this purpose. The jet variance is found to increase with increasing disturbance level. In addition, the Phase I measurements suggest that the plenum and/or nozzle geometry may also play a role.

6.1 The scalar variance, revisited

The measured variance values from 55 runs are displayed in Fig. 6.1. Points which did not appear previously on Fig. 4.4 include the Phase I, $x/d = 100$, and Phase II, $x/d = 295$, measurements.

In the course of conducting the $x/d = 305$ runs, the difference between the previous Phase I variance values and the Phase II results was puzzling. Suspicions grew that the cruciform in the plenum was possibly misaligned, causing swirl in the jet, so several things were tried at the new $x/d = 295$ location. The cruciform was removed, but the variance increased. The time the plenum sat between filling and starting the run was increased by 50%, yet the resulting variance was still large.

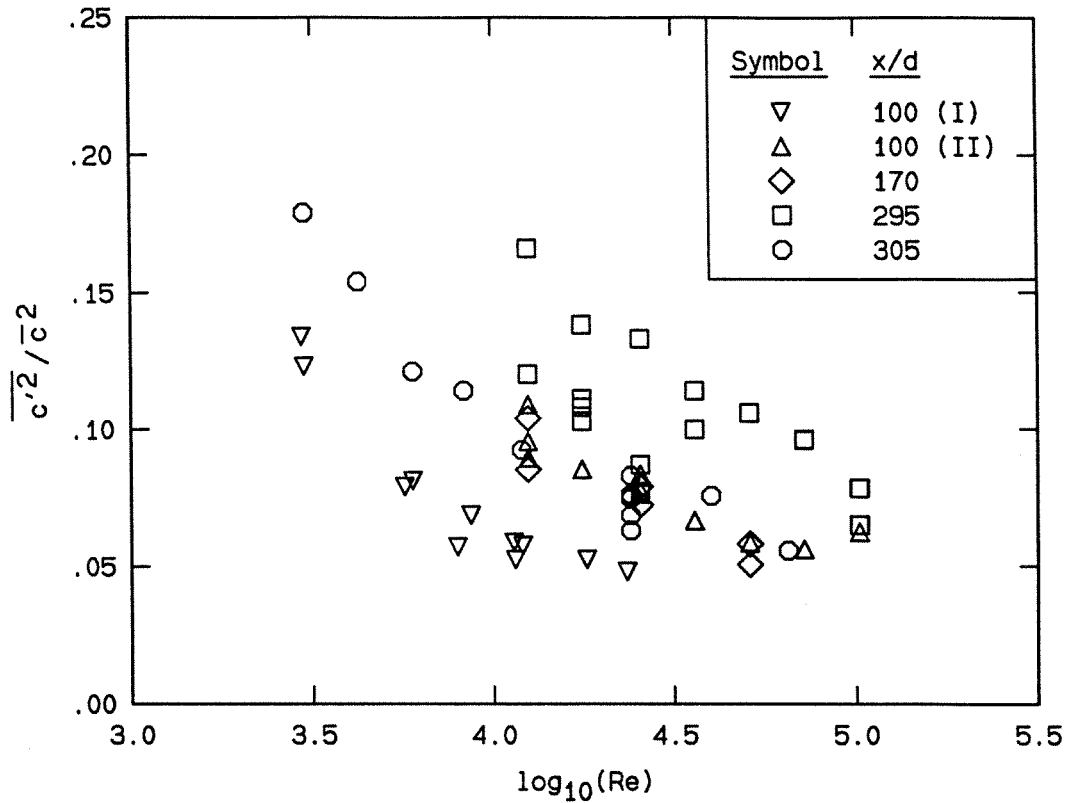


Fig. 6.1 Measured variance values for complete ensemble of runs.

Finally, a series of runs was conducted in which the plenum was vigorously filled, and the run started within 60 seconds. These runs were called “quick runs.” This is in contrast to the previous “quiet runs,” when the plenum was filled more than 30 minutes before the run to allow any disturbances to decay. The collection of results from $x/d = 295$ is displayed in Fig. 6.2. The resulting variances of the quick runs were consistently high, with a few exceptions. After repeating quick runs at $Re = 17,600$ and not observing variances as large as at adjacent Reynolds numbers, the water under the plenum was stirred briskly by hand (for ~ 10 seconds) and the run was conducted within 30 seconds. The resulting variance was much higher. This is the “extra disturbance” run in Fig. 6.2. These results indicate that the cruciform had been doing its job, reducing the plenum disturbance levels. It is concluded that both the *plenum* disturbance level and the disturbance level at the *exit of the nozzle*

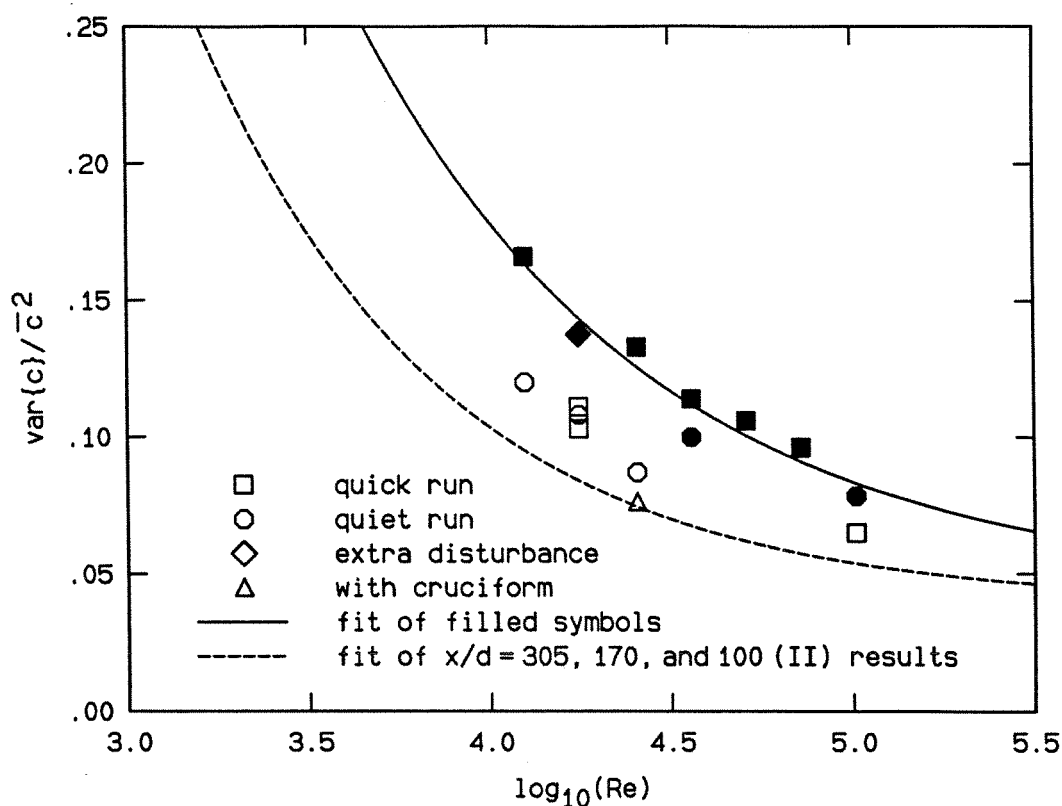


Fig. 6.2 Measured variance values for the Phase II, $x/d = 295$ runs. The *shapes* of the symbols designate the run conditions. Additionally, the filled symbols were selected as representative of an upper bound of the measured values, and fit with an expression of the form $A + B Re^p$. Parameter values determined from the fit are: $A = 0.045$, $B = 19.6$, and $p = -0.54$.

affect the variance, generally increasing it with increasing disturbance levels.

In order to fill the plenum with dyed fluid before a run, it was necessary to reach below the nozzle plate (under water), and hold a finger over the nozzle exit while pouring the fluid into the plenum. After the plenum was full, the fill valve was closed and the finger removed. The act of withdrawing the hand from beneath the nozzle, and the attendant disturbances left behind in the nozzle exit vicinity, are deduced to be a major cause of the high variance levels in the quick runs. The hand was withdrawn more gently before the quick runs with the smaller variances. The result from the extra disturbance run is consistent with this explanation. The

high (quiet run) result at $Re = 36,000$ is a bit of a puzzle, since it sat for 30 minutes prior to the run. The discrepancy at $Re = 102,000$ should be viewed in light of the hissing noise accompanying those runs (as described in Chapter 4).

Note that two fits are included in Fig. 6.2. The solid line is a fit of $A + BRe^p$ to the filled symbols. This function was chosen for reasons described in Chapter 4. The points included for this fit were chosen somewhat subjectively for their appearance of lying on a distinct “branch.” Also included in the plot is the fit obtained to the other Phase II data, which appeared previously in Fig. 4.4. The asymptotic values obtained from the fits (parameter A) are similar (0.039 in Fig. 4.4 and 0.045 in Fig. 6.2). The multiplicative factors B changed from 24.8 (Fig. 4.4) to 19.6 (Fig. 6.2), and the exponents p changed from -0.65 (Fig. 4.4) to -0.54 (Fig. 6.2). The disturbance level beneath the nozzle is clearly not the entire cause of the large variance values. The run with the cruciform conforms to the previous behavior, while, without the cruciform, no amount of waiting for the plenum to settle produced such low levels. However, the cruciform was not replaced for the subsequent $x/d = 100$ and 170 runs (although they were “quiet runs”), yet their variance values agree with the behavior at $x/d = 305$, with the cruciform present. This suggests that the axial location is a parameter in the sensitivity of the local normalized variance to disturbance levels. It is not known whether this dependence reflects the confinement of the jet (noting that $x/d = 295$ is over half the working height of the tank), or some other factor.

6.2 Plenum/nozzle geometry

The Phase I results are plotted alone in Fig. 6.3. Again, the results are fit with an expression of the form $A + B Re^p$. Note that the change in the exponent p indicates that these curves are not simply translating, as if from a virtual origin shift. The resulting asymptotic value of A (0.043) agrees well with the values 0.045 and 0.039 from the other two fits. This value of A differs slightly from the inferred value of 0.04 from Miller & Dimotakis (1991b), because the least squares fit here is for the variance. Previously, it was for the rms, and the corresponding error weighting is slightly different.

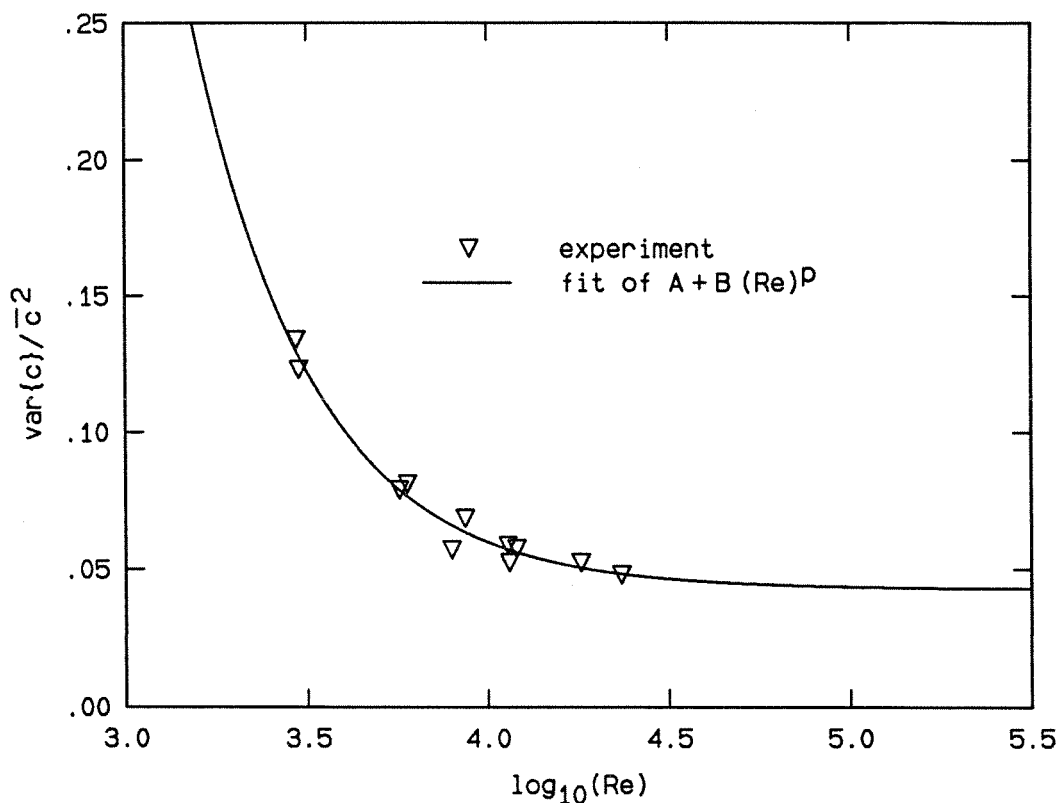


Fig. 6.3 Measured variance values for the Phase I, $x/d = 100$ runs. The results were fit with an expression of the form $A + B Re^p$. Parameter values determined from the fit are: $A = 0.043$, $B = 3,600$, and $p = -1.33$.

The conclusions of the previous section may help explain the disagreement

between the Phase I and Phase II variance values (Fig. 6.1). Both sets of experiments were conducted in the same facility, using nozzles of the same diameter, and both plena contained cruciforms of similar design to reduce plenum disturbances. However, there were two major differences between the two configurations: the contraction ratio (and size of the plena), and the nozzle exit geometry. The Phase I plenum had a 9.5 cm (3.75 in.) internal diameter, and the nozzle consisted of a smooth radius at the inlet and a short length of 0.254 cm (0.1 in.) I.D. tubing extending 1.8 cm (0.7 in.) beyond the nozzle plate (see Fig. 2.2). The tubing extension was tapered on the outside to provide a thin edge at the nozzle exit. The Phase II plenum had a nominal 14.5 cm (5.7 in.) I.D., and the nozzle consisted of a circular contour leading to the exit plane of the nozzle plate, with a $\sim 3^\circ$ converging angle at the exit. With no extension tube, the nozzle exit was flush with the surface of the 30.5 cm (12 in.) lucite nozzle plate (see Fig. 2.3).

Because of the different plenum diameters, the area contraction ratios were dissimilar for the two plenum/nozzle combinations. The Phase I contraction was about 1400, while the Phase II ratio was close to 3200. Since a contraction has the effect of stretching disturbances in the streamwise direction, amplifying streamwise vorticity, the difference in the two contraction ratios would cause equivalent disturbances in the two plena to amplify by different amounts. This may have influenced the resulting jet variance through some unknown mechanism.

Although the contraction ratio might be able to account for the difference in variance behavior, there are also details of the nozzle geometries which should be considered. In the case of the Phase I nozzle, the short extension permitted entrainment from behind the plane of the nozzle exit, while the Phase II jet emerged from a hole in a wall, with corresponding radial entrainment from the very beginning. If the changes in behavior were influenced by the flow in the vicinity of the nozzle

exit (such as the potential core shear layers), the local entrainment flow might play a role. In comparison, Dowling & Dimotakis (1990) reported scalar variance values on the centerline of a gas-phase jet. That experiment had a mild co-flow to satisfy the entrainment requirements of the enclosed jet. It is interesting to note that their measured variance was relatively unchanged over a range of Reynolds numbers from 5,000 to 40,000.

In conclusion, it has been shown that both the nozzle/plenum geometry and disturbance levels may greatly influence the jet variance (under some conditions, doubling the measured values). It has not been determined, at this time, to what extent this sensitivity may be susceptible to Schmidt number. Many investigations of excited jets (e.g., Lee & Reynolds 1985) have been reported in the literature. The current findings contribute observations of quantitative effects on the jet mixing, from the influences described above, in *unforced* jets.

CHAPTER 7

Discussion of Schmidt number effects

The various measures of jet mixing behavior examined in Chapter 4 are revisited, and compared to gas-phase (order unity Sc) results. The measurements of Dowling (1988) and Dowling & Dimotakis (1990) are used for this comparison because the demonstrated similarity behavior of those data testifies to their quality. For additional comparison, consult the references in both of the above investigations.

The jet centerline concentration pdf's are examined. In the current high Sc case, the pdf's become narrower and taller with increasing Re , while the gas-phase results change little. Correspondingly, the normalized scalar variance values decrease in the liquid-phase with increasing Re , while the gas-phase values do not. Indications are that the differences in mixing behavior are less pronounced as the Reynolds number is increased. The high Schmidt number power spectra exhibit a much greater high frequency content compared to the gas-phase. The implication of these findings is that the high Schmidt number turbulent jet is less homogeneous, or less well mixed, than the gas-phase jet, at least at the low to moderate Reynolds numbers investigated.

7.1 Scalar pdf's

Pdf's from the current work are displayed in Fig. 7.1 with the gas-phase results of Dowling (1988). The high Schmidt number pdf's, as described in Chapter 4, become narrower and taller with increasing Re , while the gas-phase cases at $Re = 5,000$ and $16,000$ show little change.

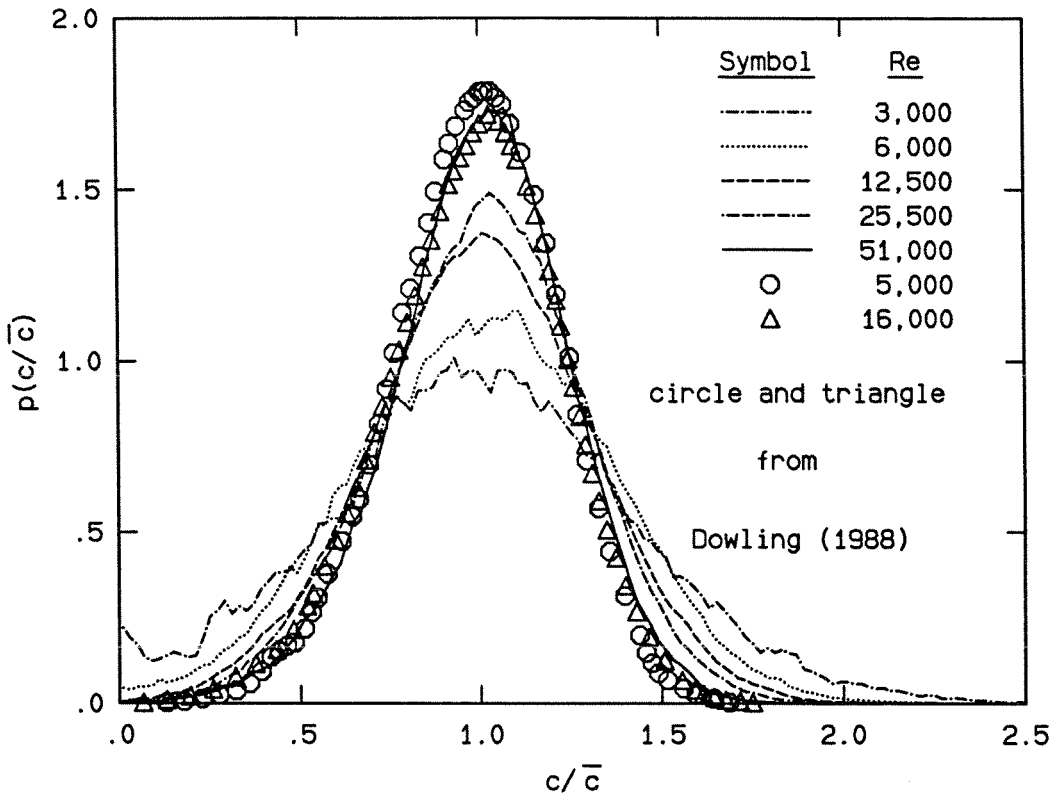


Fig. 7.1 Comparison of current pdf's with gas-phase results from Dowling (1988).

What little change is apparent in the Dowling pdf's is in the opposite direction from the liquid-phase jets. At the higher Reynolds numbers, the differences between the two cases are much less pronounced. These results suggest that, at the lower Reynolds numbers investigated, the gas-phase jet is more homogeneous, or better mixed, than the high Schmidt number jet, but that this difference decreases with increasing Re .

7.2 Scalar variance

Consistent with the behavior of the pdf's, the high Schmidt number variance decreases with increasing Reynolds number, in contrast to the gas-phase values, which are relatively constant (Fig. 7.2).

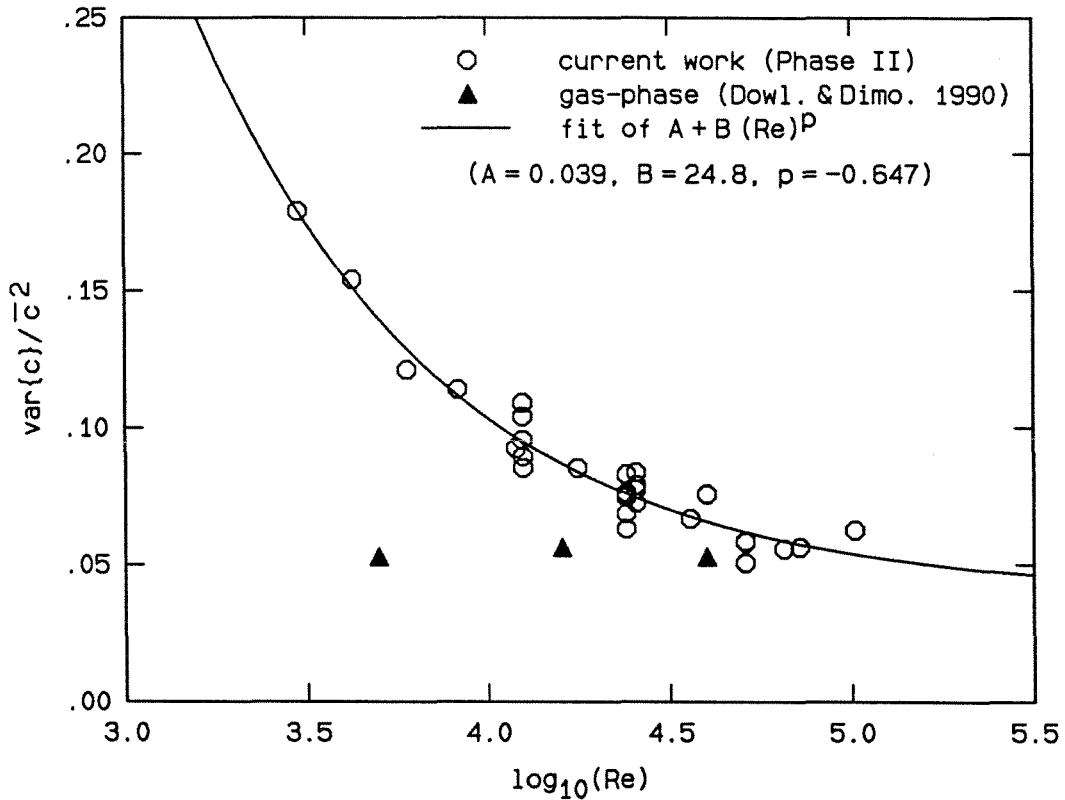


Fig. 7.2 Comparison of variance values with gas-phase results from Dowling & Dimotakis (1990).

In fact, the reported statistical error bars for the gas-phase variances overlap (Dowling & Dimotakis 1990), implying that any perceived trend in those data may not be statistically significant. In light of the observations on convergence of the jet concentration pdf's in Chapter 3, such variations are not surprising. The behavior of the variance again indicates that the high Schmidt number jet is less well mixed than the gas-phase jet, with the difference decreasing with increasing Re .

7.3 Power spectra

Power spectra from the current work are compared in Fig. 7.3 with the gas-phase spectra of Dowling (1988). The high Sc spectra have a considerably greater extent than the order unity Sc spectra at the high frequencies.

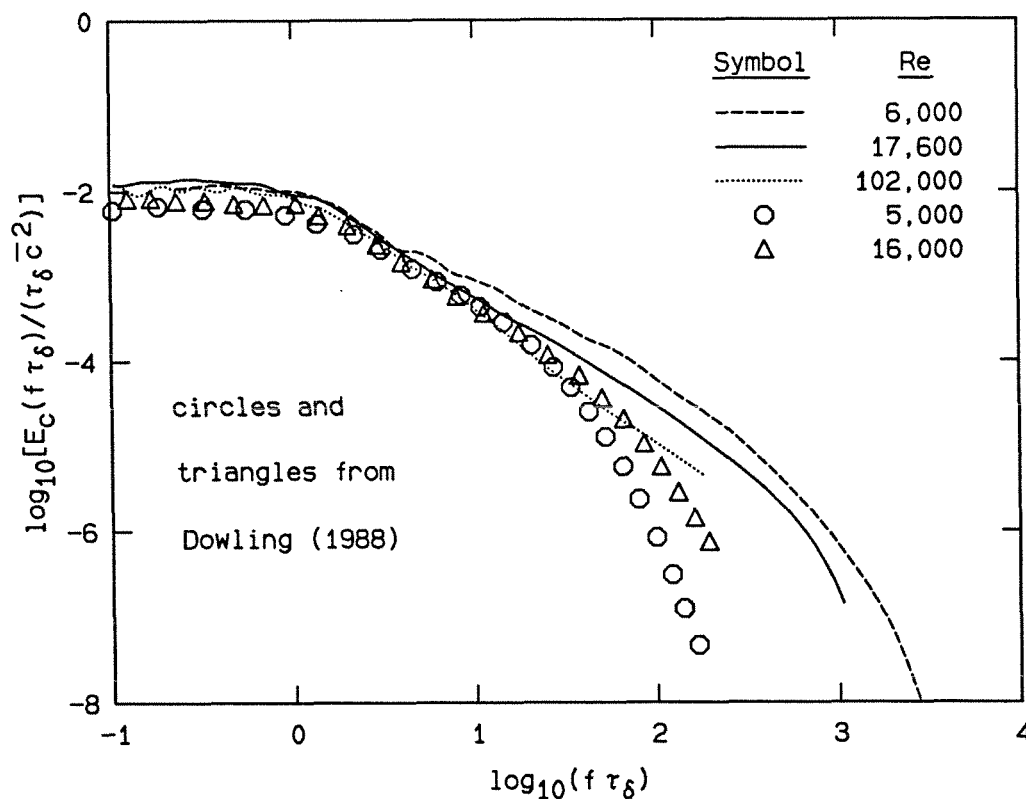


Fig. 7.3 Comparison of power spectra with gas-phase results from Dowling (1988).

This behavior is expected in view of a species diffusion scale that is smaller than the viscous diffusion scale, which provides an additional length scale in the flow (as noted by Batchelor 1959). While no constant -1 spectral slope is present, as discussed in Chapter 5, a log-normal range is observed at frequencies higher than the viscous scale, suggesting that the particular assumptions of Batchelor's theory which lead to the -1 slope require reexamination (cf. Dimotakis & Miller 1990).

In addition to the greater extent of the high frequency portion of the high Sc spectra, it is also noted that the power spectral densities are slightly larger than the gas-phase values, over the entire range of frequencies. A possible factor in this difference is that Dowling's jet nozzle was externally contoured, and a mild co-flow was provided to satisfy the entrainment requirements of the (enclosed) jet. There was no co-flow in the current work. If the effect of the co-flow was to reduce fluctuations near the nozzle, and consequently throughout the jet (in light of the findings described in Chapter 6), it may have resulted in the broadly lower spectral densities.

CHAPTER 8

Estimation of flame lengths

Estimated flame lengths from the current work are compared with those of Dowling (1988) and Dahm (1985), and are found to become significantly shorter with increasing Reynolds number, in contrast to the previous investigations. This Reynolds number dependence is greatest at the lower Re , but persists to some extent to the highest Re investigated.

8.1 Estimation method

Much of the following discussion is excerpted from Appendix B of Miller & Dimotakis (1991b).

Given the jet fluid concentration pdf's $p(c, x; Re)$, the "flame length" can be estimated as the distance required for $1 - \epsilon$ of the jet fluid (with, say, $\epsilon = 0.01$) to have mixed to the proper stoichiometric composition (stoichiometric jet fluid fraction) c_s , as required by the chemical reaction. This is related to the stoichiometric mixture ratio (equivalence ratio) ϕ by the expression

$$c_s = \frac{1}{\phi + 1}, \quad (8.1)$$

where ϕ is equal to the parts of reservoir fluid that must be molecularly mixed and reacted for the complete consumption of one part of (pure) jet fluid.

Briefly, to estimate the flame length corresponding to a given c_s and ϵ we need two additional assumptions. First, that the pdf of concentration on the jet axis is a function of c/\bar{c} only, i.e.

$$p(c, x) \approx f(c/\bar{c}) , \quad (8.2)$$

where the function $f(c/\bar{c})$ may vary with Reynolds number (and Schmidt number), but is taken as independent of x/d . Note that it is $f(c/\bar{c})$ that was plotted under this implicit assumption in Chapter 4. This is the usual assumption, recently corroborated for gas phase ($Sc \sim 1$) turbulent jets (Dowling & Dimotakis 1990), with supporting evidence for liquid phase ($Sc \sim 10^3$) jets (see discussion in Chapter 4, and also Papanicolaou & List 1988). The second assumption deals with the dependence of \bar{c} on x/d , i.e. (momentum-driven turbulent jets)

$$\bar{c} = \frac{\kappa d^*}{x - x_0} . \quad (8.3)$$

In this expression, the (pure) jet fluid concentration is taken as unity, the dimensionless parameter κ is taken as a constant (which may, however, depend on Reynolds number, e.g., Dowling & Dimotakis 1990), d^* is the jet momentum diameter (e.g., as used in Dahm & Dimotakis 1985), and x_0 is a virtual origin (possibly weakly dependent on Reynolds number at low Reynolds numbers). Combining Eqs. 8.2 and 8.3, we have, for each Reynolds number,

$$p(c, x) \approx f \left[\left(\frac{x - x_0}{\kappa d^*} \right) c \right] . \quad (8.4)$$

For a given ϵ , the flame length L_f may then be estimated as the implicit solution of the equation

$$\int_{c_s}^{\infty} p(c, L_f) dc = \epsilon . \quad (8.5)$$

It can be seen that the computed flame length is determined by the behavior of the pdf at high values of c/\bar{c} . Basically, if $f_j(c/\bar{c})$ is the pdf of c/\bar{c} at a Reynolds number Re_j , then for $c_s/\bar{c} > 1$ (small ϵ) and $f_2(c_s/\bar{c}) > f_1(c_s/\bar{c})$, we will have $L_{f2} > L_{f1}$. In other words, and as perhaps obvious in retrospect, a larger c'/\bar{c} (less well-mixed jet) implies a longer flame length.

The inferred flame length dependence on Reynolds number made above assumes that any deviations of the x -dependence of $p(c, x)$ from Eq. 8.2, as well as the possible dependence of d^* , κ and x_0 on Reynolds number, are not strong enough to offset the relatively large dependence of L_f predicted using Eq. 8.5 and the assumptions outlined above. We note, however, that the rigorous validity of these assumptions may not be unassailable, especially at the high Schmidt number in this experiment (Dimotakis & Miller 1990).

With these caveats in mind, the flame lengths were estimated from the current concentration data. Equation 8.5 was implemented in the form

$$\int_{c_\epsilon/\bar{c}}^{\infty} p(c/\bar{c}) d(c/\bar{c}) = \epsilon, \quad (8.6)$$

where c_ϵ is determined implicitly. A value of $\epsilon = 0.01$ was selected, permitting sufficient statistical confidence, and the pdf's were integrated numerically, starting at the largest concentrations, to determine c_ϵ/\bar{c} . The stoichiometric mixture ratio is related to c_ϵ/\bar{c} by

$$c_s = \left(\frac{c_\epsilon}{\bar{c}}\right) \bar{c} = \frac{1}{\phi + 1}. \quad (8.7)$$

Using Equations 8.3 and 8.7, having determined c_ϵ/\bar{c} , the flame length is computed from (cf. also Dowling 1988, Eq. 5.6)

$$\frac{L_f}{d^*} = \frac{c_\epsilon}{\bar{c}} \kappa (\phi + 1). \quad (8.8)$$

Here, the effect of (the small) virtual origin x_0 has been neglected. For the current results, the momentum diameter d^* will be replaced by the geometric nozzle diameter d , since the reservoir and jet densities are matched and the nozzle exit velocity profile should be very close to an ideal “top-hat” profile.

Because the current measurements are of relative, and not absolute, concentration, it is necessary to approximate the jet concentration decay constant κ . A value of $\kappa = 5.2$ was chosen as intermediate between the reported values of $\kappa = 5.4$ from Dahm (1985) and 5.11 at $Re = 5,000$ from Dowling & Dimotakis (1990). Additionally, κ was taken to be independent of Reynolds number, primarily because existing experimental results (Ricou & Spalding 1961, and Dowling & Dimotakis 1990) suggest opposite Re effects, and it is unclear what the Re dependence, if any, would be. This is an assumption in the following discussion.

8.2 Results

The computed values of L_f for both Phase I and II data, using $\epsilon = 0.01$, $\phi = 10$, and $\kappa = 5.2$, are displayed in Fig. 8.1.

The estimated flame lengths vary by 24% in the Phase I measurements, and more than 35% in Phase II, over the Reynolds number range investigated, with increasing Re yielding shorter flame lengths. The vertical separation of the two sets of data is approximately 13%. In the context of the findings in Chapter 6, it is possible the differences between the plenum/nozzle geometries may be the source of this offset. In particular, if the values of κ in the two situations differed by 13% (the Phase I κ being larger), the difference would be removed. A dependence of κ on Reynolds number could also be a factor in the decrease of the flame lengths, for both sets of data. However, the reported values of κ in the literature (e.g., Dowling

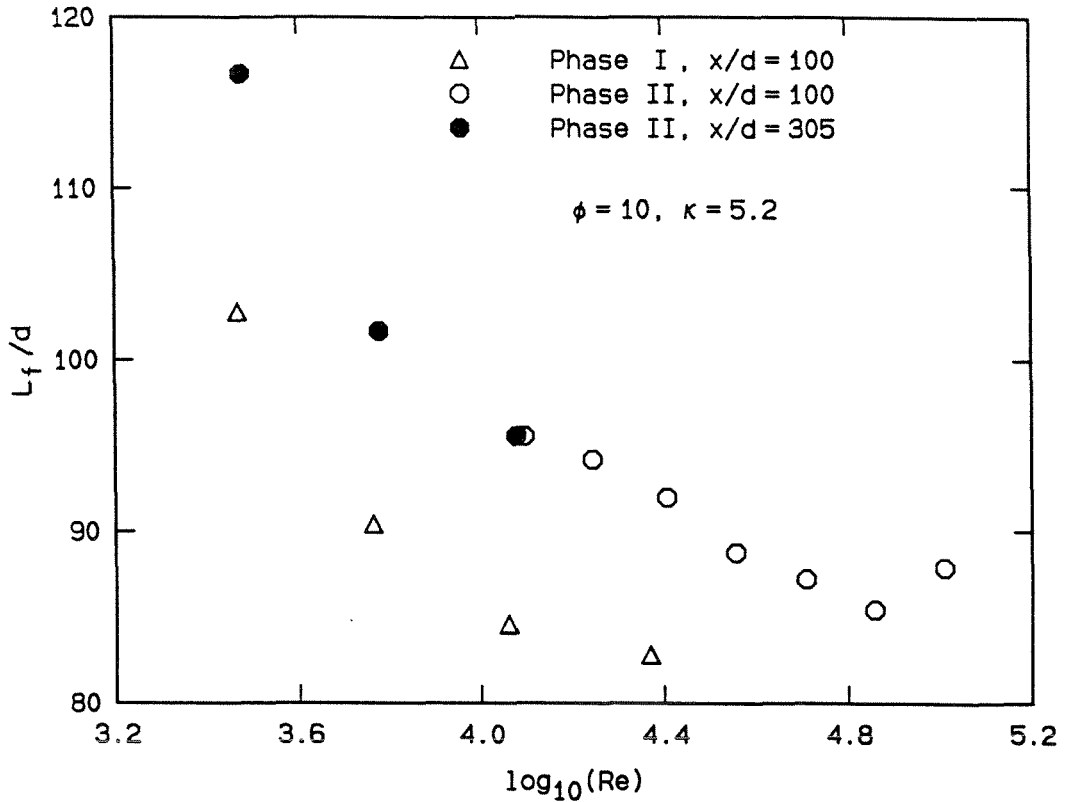


Fig. 8.1 Values of L_f/d , computed from the concentration pdf's, for $\epsilon = 0.01$, $\phi = 10$, and $\kappa = 5.2$. Both Phase I and II data are shown.

& Dimotakis 1990, Fig. 7) lie between 4.5 and 5.5, for the most part. The change in κ required to account for the entire 33% Phase II variation is greater than this range of values, which most likely reflects other influences as well, such as facility geometry. In addition, no clear Reynolds number dependence is evident in those results. It is therefore considered unlikely that the *entire* variation in the flame lengths could be accounted for by a Reynolds number dependent κ . This suggests that increasing molecular mixing is taking place with increasing Re , as manifested by the narrower pdf's and smaller resulting c_ϵ/\bar{c} 's.

8.3 Comparison with other investigations

The flame lengths for the current (Phase II) data are compared in Fig. 8.2 with the maximum observed flame lengths of Dahm (1985) in water, and the gas-phase estimates of Dowling (1988). Dahm's results are from observations of an acid-base reaction, conducted at particular values of ϕ , while Dowling's flame lengths were estimated from passive scalar measurements, in the same manner as the current work (with $\epsilon = 0.01$). Dowling's results are displayed as symbols, rather than lines, for clarity. As mentioned above, the value of κ used in Fig. 8.2 is 5.2.

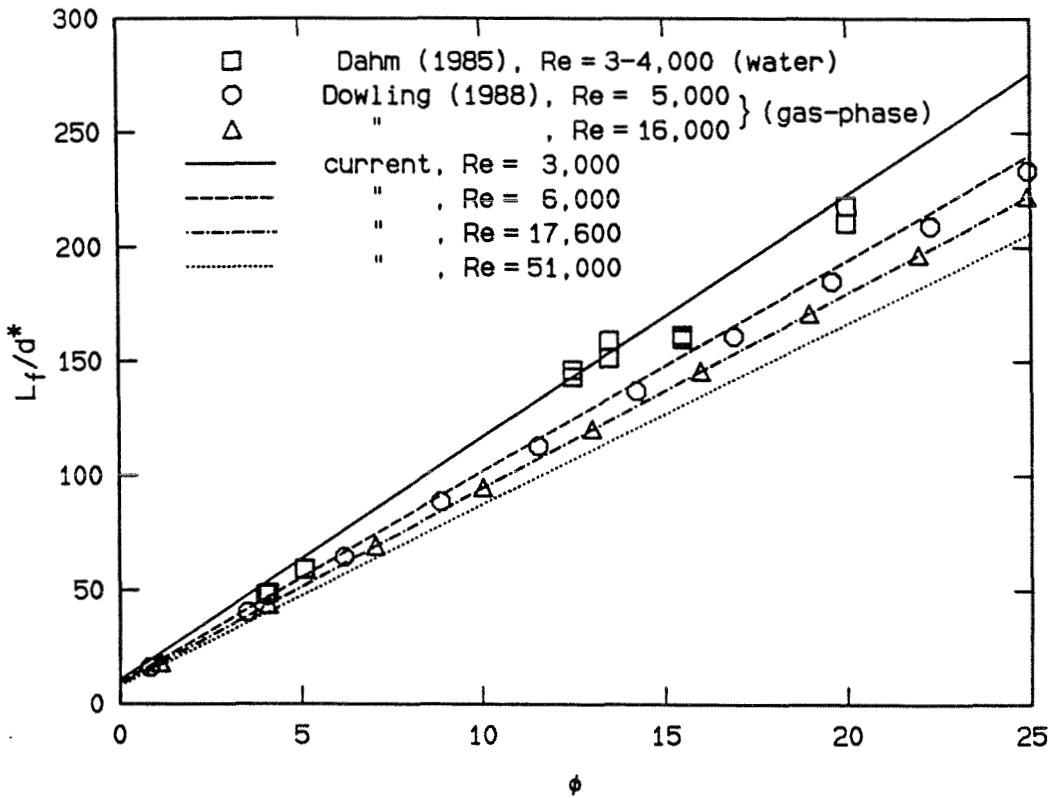


Fig. 8.2 Comparison of current Phase II flame length estimates with gas-phase results from Dowling (1988) and previous results in water from Dahm (1985).

It is apparent from Fig. 8.2 that the current flame lengths vary by more than 33% over the range of Reynolds numbers investigated. This is in contrast to earlier

findings in liquid-phase turbulent jets (Weddell 1941, Dahm 1985) that the flame lengths were constant for Reynolds numbers in excess of 3,000. In addition to a possible variation of κ in the present experiments, discussed above, part of the discrepancy may be in the respective Schmidt numbers of the two measurements.

In using an acid-base reaction technique to measure flame lengths, the reaction was determined by the pH of the environment around each dye molecule. The Schmidt number in that situation will reflect the diffusion coefficients of both the dye and the acid (hydrogen ions, i.e., protons) — some intermediate value. The diffusion of protons in water is very fast. In addition to its small size, there is a mechanism in which a free proton is bound to a water molecule, releasing one of the two protons previously attached. By means of this bond swapping, protons in water can “diffuse” without moving (F. Anson, personal communication). The resulting diffusion coefficient for (infinitely dilute) protons in aqueous solution is $9.3 \times 10^{-5} \text{ cm}^2/\text{sec}$ (e.g., Parsons 1959, p. 79), almost 18 times the diffusivity of fluorescein. Therefore, it would be expected that the Schmidt number describing the acid-base reaction would lie somewhere between the Sc of the protons (≈ 100) and the dye (≈ 1900). It is not known to what extent this could account for the difference between previous results and the current work.

The apparent agreement in Reynolds number behavior of the current flame lengths with the estimates of Dowling (1988) may well be coincidental. First, the difference between his reported flame lengths at $Re = 5,000$ and $16,000$ is about 5%. This is the result of a decrease in κ of 8%, combined with a slightly wider pdf at $Re = 16,000$. For the current flame-length estimates, κ is approximated by a constant. If a similar decrease in κ with Re were included, the Reynolds number dependence of the current flame lengths would be *even stronger*. Note that κ determines the behavior of the mean concentration, and is a function of the

jet entrainment rate. Entrainment is a feature of the velocity field, which, at the Reynolds numbers of interest here, should be unaffected by changing the Schmidt number (species diffusion coefficient). Any Reynolds number dependence of κ in a turbulent jet, therefore, would be expected to be independent of Schmidt number. It could, however, possibly be flow-geometry dependent. If the current trend of decreasing flame lengths with increasing Reynolds number were to be explained solely by a change in κ , not only would a very substantial change of about 33% be required, but it would have to be in *the opposite sense* as that observed by Dowling (1988) between $Re = 5,000$ and 16,000.

Secondly, in Dowling & Dimotakis (1990), additional data at $Re = 40,000$ were reported. While κ for those runs was not derived directly, it was estimated to be about 5.1 to 5.2. This estimate, combined with the near perfect coincidence of their $Re = 40,000$ pdf with their pdf at $Re = 5,000$, suggests that the estimated gas-phase flame length at $Re = 40,000$ would be *very nearly the same* as the $Re = 5,000$ case. This is in contrast to the observed high Schmidt number behavior, as seen in Fig. 8.2, in which there is a strong dependence of flame length on Reynolds number.

CHAPTER 9

Conclusions

These experiments have investigated the behavior of the passive scalar field of a round, axisymmetric, turbulent jet at high Schmidt number. High-resolution, temporal, single-point measurements, on the jet axis, were obtained using laser-induced fluorescence techniques to determine the jet fluid concentration. The principle conclusions of this work include the following:

1. Time traces of the concentration exhibit features indicative of the passage of large-scale structures, on the order of the local jet diameter in extent, including both upstream facing ramps and plateaus.
2. Analysis of the accumulation of the concentration histogram suggests the statistics of that quantity deviate significantly from statistics of a random (binomial) process.
3. Long-time statistics of the jet concentration converge slowly. About 100–300 large-scale structure passages are required to reduce the uncertainty in the mean to 1%. Similar conclusions have previously been reported for shear layers (Dimotakis & Brown 1976).
4. As the Reynolds number is increased, the normalized scalar variance is produced over a relatively narrower range of scales.
5. The jet centerline concentration pdf's vary with Reynolds number, becoming taller and narrower as Re is increased. The jet centerline concentration variance correspondingly decreases with increasing Re .

6. The jet centerline concentration power spectra evolve with Reynolds number, with average slopes between the large-scale passage frequency and the high-frequency roll-off of about -1 at $Re = 3,000$, increasing to about $-3/2$ at $Re = 102,000$.
7. No constant -1 (Batchelor) spectral slope region is present in the concentration power spectra of these high Schmidt number (~ 1900) jet flows.
8. For scales in the viscous region, the power spectra exhibit a *log-normal* behavior, over a range exceeding a factor of 40, in some cases.
9. The location of the beginning of the log-normal spectral region is marked by a break-point in the spectrum. The break-point frequency scales like $Re^{3/4}$, but is about 80–85 times smaller (corresponding to a larger scale) than the calculated value of the Kolmogorov scale passage frequency.
10. Mixing in the far-field of high Schmidt number turbulent jets is found to be susceptible to initial conditions. In particular, fluid disturbances in the jet plenum and in the vicinity of the nozzle exit were discovered to strongly influence the normalized jet centerline scalar variance, with larger disturbances causing larger variances, i.e., less homogeneous mixing. A larger contraction ratio plenum, its nozzle orifice flush with a large end-plate, produced larger variances than a smaller contraction ratio plenum with a short nozzle tube extension, of the same nozzle exit diameter.
11. Similar to shear layer behavior, the effects of initial conditions are found to persist for hundreds of diameters from the nozzle exit, over hundreds of large scales.
12. Mixing in high Schmidt number turbulent jets differs from gas-phase, order unity Sc , jet mixing. At low to moderate Re , the higher Sc jet is less well

mixed. The indications are that, as the Reynolds number is increased, the difference in mixing behavior is less pronounced.

13. The large variations with Re observed in the concentration pdf's, scalar variance, and power spectra, are not found in gas-phase results.
14. Flame lengths estimated from the current data decrease substantially with increasing Reynolds number, in contrast to previous results from both liquid- and gas-phase jets. This implies either a change in the entrainment rate of the jet, in excess of the range of previously reported values, and/or an increase in the amount of molecular mixing in the jet.

APPENDIX A

Description of flow parameters

This appendix will detail many of the specific flow parameters for these experiments. For a description of the experimental apparatus, see Chapter 2. For a discussion of the relevant microscales and resolution issues, consult Appendix C.

A.1 Velocities and large scales

The principle flow variable in these experiments was the jet exit velocity u_0 . As described in Appendix B, in the Phase I experiments, u_0 was determined from a volume flux measurement which was conducted during each run. In Phase II, the calibration was done in advance, also from direct volume flux measurements. The result was then expressed as a Reynolds number based upon the jet nozzle diameter d and the kinematic viscosity ν , i.e.,

$$Re \equiv \frac{u_0 d}{\nu}. \quad (\text{A.1})$$

Both the value of d and the determined u_0 were considered accurate to a few percent, while ν is a weak function of temperature, varying about 2% per degree near room temperature. The resulting Reynolds numbers are considered accurate to about $\pm 5\%$. Most of the jet quantities of interest have weak dependences on Re , e.g., logarithmic, so this accuracy is considered more than adequate.

The jet growth rate was measured shadowgraphically, as described in Appendix D. The visual full jet angle found, about 23° , was in agreement with previously reported values. The virtual origin was determined from the shadowgraph pictures to be, at most, a few nozzle diameters at the lower Reynolds numbers – less at the higher. Since the measuring stations were located 100 or more diameters downstream, the virtual origin was neglected in the computations.

To estimate the jet centerline velocity u_{cl} , the relation reported in Chen & Rodi (1980),

$$u_{cl} = 6.2 u_0 \left(\frac{x - x_0}{d} \right)^{-1}, \quad (\text{A.2})$$

was used, where x is the axial distance from the nozzle exit and x_0 is the jet virtual origin (cf. Dowling 1988). In Equation A.2, the constant (6.2) may vary from experiment to experiment. The importance of such a variation is minimal in this work, because this relation is used primarily in its role as a scaling law, i.e., $u_{cl} \propto d/x$.

The calculated centerline velocity may be used to estimate a jet large-scale time τ_δ , defined here as

$$\tau_\delta(x) \equiv \delta(x)/u_{cl}(x), \quad (\text{A.3})$$

where δ is the local visual width of the jet. In the present work, time variables are often nondimensionalized by τ_δ , anticipating its role as a scaling parameter. The centerline velocity is also useful for converting the temporal data from the experiment to its spatial equivalent by dividing the time units by the convection velocity, approximated as u_{cl} on the jet axis. This is often referred to as *Taylor's hypothesis* or the *frozen-flow hypothesis*. The only use of Taylor's hypothesis in this thesis is to convert calculated spatial scales, e.g., λ_K , to their $\log_{10}(f\tau_\delta)$ equivalents for comparison with results, and to estimate the resolved scales in Appendix C. In

those instances, the approximations involved should always be kept in mind.

A.2 Buoyancy length scale

The following amplifies on the discussion of buoyancy in Miller & Dimotakis (1991b).

Buoyancy is an important consideration in experiments such as these, because the buoyant jet (or plume) behaves differently (enhanced entrainment, for example), than the momentum-dominated jet. There are several influences to be considered: buoyancy from a jet fluid/reservoir fluid density difference, buoyancy from a nonuniform reservoir density profile (stratification), and possible heating of the jet at the measuring station by the laser beam. Briefly, a nondimensionalized buoyancy length scale (Fischer et al., 1979),

$$\frac{L_b}{d} \equiv \left(\frac{\pi \rho_j}{4 \rho_\infty} \right)^{1/4} \left[\frac{\rho_j u_0^2}{(\rho_j - \rho_\infty) g d} \right]^{1/2}, \quad (\text{A.4})$$

where ρ_j is the jet fluid density, ρ_∞ is the reservoir fluid density, u_0 is the jet exit velocity, and g is the acceleration of gravity, may be derived from dimensional analysis (e.g. Dowling 1988, Sec. A.5). This parameter may then be compared with experimentally derived values to determine the role of buoyancy in the flow. In particular, Papanicolaou & List (1987, 1988) find that jets are momentum-dominated if x/L_b is less than one, while Chen & Rodi (1980) cite a limit of roughly 0.5.

We will estimate the maximum anticipated density difference and calculate the resulting value of L_b/d for the Phase I measurements. A density difference here may arise from the addition of dye to the jet fluid, or from a temperature mismatch between the jet fluid and the reservoir fluid. Let us consider the two contributions separately, since, it turns out, they are of different magnitudes. The

fluorescein dye concentration used in the experiments was roughly 3.3×10^{-7} M in the Phase I experiments. The formula weight of disodium fluorescein is 376.28. This yields an estimate for the dye-induced buoyancy length scale (from Eq. A.4) of more than 19,600 jet nozzle diameters at the lowest Re . For each run, the jet fluid was prepared by diluting a small amount of concentrated stock solution of dye with sufficient water, taken from the reservoir shortly before the run, to yield the proper jet dye concentration. This procedure resulted in no observable temperature discrepancy between the plenum fluid and the reservoir fluid. Using Eq. A.4, the estimated buoyancy length scale resulting from a temperature difference of 0.1° C, the accuracy of the thermometer, is 1,500 jet nozzle diameters. While, of the two contributions, the possible influence of a worst-case temperature mismatch is larger, the resulting buoyancy length is 15 times the distance between the nozzle and the measurement location at $x/d = 100$. Therefore, based on the criterion of Chen & Rodi (1980), the momentum-dominated region extends for a distance that is more than 7 times longer.

A.3 Attenuation considerations

A second way buoyancy may arise is through heating of the fluid in the measuring volume via absorption of laser power by the dye. The approximate residence time of the fluid in the measurement volume is the measurement height ($\approx 80\mu\text{m}$) divided by the calculated mean centerline velocity at the lowest Reynolds number (0.072 m/s), or 0.001 seconds. The attenuation of the laser beam through the entire width of the jet was measured by imaging the laser light from the beam stop onto the PMT, and collecting data before and after the arrival of the jet. The laser beam intensity I at time t will be

$$\frac{I(t)}{I_0} \propto e^{-\int_{-\delta(x)/2}^{\delta(x)/2} I_{fl}(\xi, t) d\xi}, \quad (\text{A.5})$$

where I_0 is a reference intensity and $I_{fl}(\xi, t)$ is the dye fluorescence at location ξ along the beam at time t . Treating the jet concentration as uniform in the radial direction for the purposes here (not too severe an approximation — cf. Dahm 1985), and noting that for the weak concentrations employed in these experiments, $I_{fl} \propto c$, the laser beam attenuation may be approximated as

$$1 - \frac{I(t)}{I_0} \approx e^{-\alpha c}, \quad (\text{A.6})$$

where α is a constant of proportionality. The attenuation, across the entire jet width, was determined from the measurement to be about 1% for a plenum concentration of 10^{-6} M.

The attenuation across the measuring volume ($\sim 80\mu\text{m}$ wide) would therefore be about 0.0025%. Even doubling this value, and assuming a worst case (all power attenuation goes into heat), the resulting temperature rise would only be approximately 0.02° C. While the approximation of uniform concentration and velocity may tend to underestimate the temperature rise, probably much less than half of

the attenuated power is converted into heat. Therefore, this estimate is considered conservative.

It should also be noted that, while some dilatation of the fluid occurs as it passes through the laser beam, it is a localized effect. There is no global buoyancy force to affect the large-scale jet structure and entrainment, as there is when the jet and reservoir densities are different. Thus, it is not appropriate to utilize criteria such as those of Chen & Rodi (1980) in this case, since they apply to globally different densities. The primary influence here, i.e. local dilatation, will have an even weaker effect on the flow for a given temperature rise. The dilatation is extremely small, $\Delta\rho/\rho \approx 5 \times 10^{-6}$, and its influence in our flow environment is concluded to be insignificant.

Having opened the issue of attenuation, we should also consider the possibility of attenuation-caused fluctuations of the laser beam contributing to the measured values of c'/\bar{c} , or, equivalently, the scalar variance. The beam attenuation across the diameter of the jet was typically less than 3%. Fluctuations arising from this attenuation may be completely uncorrelated with the scalar fluctuations at the measurement location, in which case the variances of the two contributions add. Alternatively, the fluctuations may be exactly correlated, in which case the two contributions to c'/\bar{c} add. In either situation, the maximum influence would correspond to fluctuations between the minimum (zero) and maximum ($\sim 1.5\%$) attenuation possibilities, or a maximum correction to the value of c'/\bar{c} of roughly 0.015. This would result in, at most, a 7% change in the measured value. This should be compared with the large percentage decrease in the measured values over the Reynolds number range investigated. Therefore, even in a worst-case scenario, the fluctuations arising from the attenuation of the laser beam would represent only a small correction to the magnitude of the variation we have measured. The actual

situation is obviously not nearly so adverse, and we conclude that the attendant contamination of our results, as a result of beam fluctuations, is extremely small.

A.4 Run parameters

As described in Chapter 2, two distinct sets of experiments were conducted. The first is referred to as Phase I, and the second as Phase II. The jet nozzle diameter was common to both.

jet nozzle exit diameter = 0.254 cm

A.4.1 Phase I

The Phase I measurements were taken under the following conditions:

data acquisition frequency	20 kHz
run time	50.8 sec (38.4 sec at 23,400)
dye concentration	$\sim 3.3 \times 10^{-7}$ M
distance from nozzle exit	25.4 cm ($x/d = 100$)
jet growth rate	$\sim 23^\circ$ (full angle)
laser power	1.0 W

The following table lists additional parameters specific to each Reynolds number.

Phase I experiments						
Re	u_0 (m/s)	u_{cl} (m/s)	τ_δ (s)	# structures	λ_K (μm)	λ_B (μm)
2,940	1.16	0.072	1.43	34	242	5.6
5,800	2.29	0.142	0.725	67	145	3.4
11,500	4.54	0.281	0.367	134	87	2.0
23,400	9.23	0.572	0.180	202	51	1.2

Table A.1 Flow parameters for Phase I.

A.4.2 Phase II

The Phase II measurements were taken under slightly different conditions. The data acquisition frequency was adjusted to match each particular run, and varied from 1.5 to 70 kHz. The dye concentrations used were also changed somewhat, in the range of $1 - 2 \times 10^{-6}$ M, usually 1.5×10^{-6} M. The nozzle diameter was again 0.254 cm (.1 in.), and measurements were conducted at axial locations of $x/d = 100$, 170, 295, and 305. The jet growth rate was assumed to be 23° . The laser power was 3.5 W. Additional parameters specific to each axial location are given below.

Phase IIa experiments, $x/d = 305$						
Re	u_0 (m/s)	u_{cl} (m/s)	τ_δ (s)	# structures	λ_K (μm)	λ_B (μm)
3,000	1.14	0.0232	13.6	25	726	17
4,240	1.61	0.0328	9.60	35	559	13
6,000	2.28	0.0464	6.79	42	433	10
8,300	3.16	0.0642	4.91	37	339	8
12,000	4.56	0.0928	3.39	33	257	6
24,000	9.13	0.186	1.69	35	153	3.5
40,000	15.2	0.309	1.02	41	104	2.4
65,000	24.7	0.503	0.626	35	72	1.7

Table A.2 Flow parameters for Phase IIa.

Phase IIb experiments, $x/d = 295$						
Re	u_0 (m/s)	u_{cl} (m/s)	τ_δ (s)	# structures	λ_K (μm)	λ_B (μm)
12,500	4.76	0.100	3.05	38	241	5.5
17,600	6.70	0.141	2.16	35	186	4.3
25,500	9.70	0.204	1.50	40	141	3.2
36,000	13.7	0.288	1.06	36	109	2.9
51,000	19.4	0.408	0.748	34	84	1.9
72,000	27.4	0.575	0.530	37	65	1.5
102,000	38.8	0.815	0.374	37	50	1.1

Table A.3 Flow parameters for Phase IIb, $x/d = 295$.

Phase IIb experiments, $x/d = 100$						
Re	u_0 (m/s)	u_{cl} (m/s)	τ_δ (s)	# structures	λ_K (μm)	λ_B (μm)
12,500	4.75	0.295	0.349	477	82	1.9
17,600	6.69	0.415	0.248	504	63	1.4
25,500	9.70	0.601	0.171	500	48	1.1
36,000	13.7	0.849	0.121	465	37	0.85
51,000	19.4	1.20	0.0858	465	28	0.064
72,000	27.4	1.70	0.0606	490	22	0.050
102,000	38.8	2.40	0.0429	465	17	0.39

Table A.4 Flow parameters for Phase IIb, $x/d = 100$.

Phase IIb experiments, $x/d = 170$						
Re	u_0 (m/s)	u_{cl} (m/s)	τ_δ (s)	# structures	λ_K (μm)	λ_B (μm)
12,500	4.76	0.173	1.02	127	139	3.2
25,500	9.70	0.354	0.497	78	81	1.9
51,000	19.4	0.708	0.249	111	48	1.1

Table A.5 Flow parameters for Phase IIb, $x/d = 170$.

APPENDIX B

Experimental considerations, data acquisition, and processing

This appendix describes run procedures, selected experimental considerations, details of the data acquisition, and processing techniques used for the experiments in this thesis. The physical description of the experimental apparatus is discussed in Chapter 2, and the flow parameters of interest are outlined in Appendix A. Microscales and issues of resolution are covered in Appendix C.

There were numerous experimental concerns which contributed to the experimental design, preparations for each run, and data acquisition and processing. The goal was to conduct low-noise, high dynamic range concentration measurements in an unexcited (natural), nonbuoyant, free turbulent jet in an essentially infinite reservoir.

B.1 Run preparations

To prepare for a run, the reservoir tank was filled with water, and a pump was used to circulate the water through a filter. The filter's purpose was not to remove particles, since the water supply was already filtered, but to provide a pressure drop to remove small bubbles and dissolved gases from the water. This reduced bubble formation on the windows of the tank, and also made sure that the water was well homogenized, with no strong temperature gradients. The pump was turned off after about an hour, and the tank was allowed to sit a minimum of an hour and a half (longer for low Re , large x/d runs), allowing the water to come to rest.

At least an hour before a run was made, the laser was brought to the desired operating power for the experiment. This was to allow the laser to stabilize electronically, thermally, and therefore, optically. All of the data-acquisition electronics were left powered up continuously, including the high voltage to the PMT. The photomultiplier tube was known to require some time to achieve a quiet state. Close to run time, water was taken from the top of the reservoir and mixed with an appropriate amount of concentrated stock dye solution to obtain the desired dye concentration for the plenum. For reasons discussed in Appendix A, this concentration was kept weak, typically 3.3×10^{-7} M in Phase I, and 1.5×10^{-6} M in Phase II. Since the ratio of tank water to stock solution used was large, and the stock solution temperature was similar to the tank temperature, there was no temperature difference between the plenum fluid and the tank fluid in the Phase I measurements. The larger quantity of fluid needed to fill the plenum for the Phase II runs required additional transfers between containers and took longer to prepare for loading. Consequently, temperature differences up to 0.25° C were observed in some of the runs (normally *colder* plenum fluid), probably partly from evaporative cooling during the mixing procedure and partly conduction with containers during the necessary transfers. No change was detected from these differences in any of the jet statistics, consistent with buoyancy length estimates discussed in Appendix A.

B.2 Tank conditions

At the outset of the Phase II measurements (the first time in the current work that runs at both low Re and large x/d were conducted), the tank was left to sit overnight, and a substantial 0.6° C variation was found in the reservoir temperature between top and bottom. There is a trade-off between letting the tank sit after mixing to allow residual velocities to decay and the possible establishment

of temperature stratification if it sits too long. Unfortunately, both difficulties are most serious under the same circumstances, i.e., at low Reynolds number and large x/d .

In response, the tank was insulated with foam insulation on the bottom and lower 1/3 (metal) portion of the sides. At the same time, it was found that the tank achieved what can only be described as a rock-steady motionlessness (velocities estimated as less than 5×10^{-5} m/s) about an hour and a half after pumping ceased, as determined by observing scatterers in the water illuminated by the laser beam. Therefore, the time between turning off the recirculation pump and conducting a run was reduced to typically an hour and a half. With the insulation and reduced wait time, out of 55 runs, two were observed to have a 0.1° C stratification and three had a 0.05° C difference. None of the other runs had detectable stratification, to within 0.025° C. No behavioral differences were found between the slightly stratified and unstratified cases. As an additional refinement, for the most critical, low Re , large x/d runs, the reservoir water temperature was matched to within 0.1° C of the room temperature by adding hot water to the tank. This aided in matching the plenum fluid temperature to the tank water temperature, and eliminated any observable tank temperature stratification.

It is interesting that a slight temperature stratification was measured in the course of the Phase II experiments, but not in Phase I. Several influences are suspected. Only one run was conducted in Phase I at $x/d = 300$, the others were all at 100. Temperature gradients over the smaller distance would be smaller. More importantly, however, Phase II runs were conducted with the water surface covered. It had been noted that at large x/d , with the surface uncovered, the tank never achieved a motionless state. Evaporative cooling at the surface drove large-scale recirculation in the tank, with velocities visually estimated to be in the 1×10^{-3}

to 1×10^{-4} m/s range. While this represents only about 1% of the centerline velocity for $Re = 3,000$ at $x/d = 100$, it would be closer to 4% at $x/d = 305$ (at the same Re), and it was desired to reduce these velocities. Covering the surface accomplished this very well, as described above. The estimated Phase I motion was possibly large enough to turn the tank fluid over in about an hour, a time shorter than required to establish a detectable temperature gradient. The shadowgraphy described in Appendix D was sensitive enough to visualize this surface cooling, and inverted mushrooms of fluid could be seen dropping from the air-water interface if the evaporation was enhanced by blowing on the surface.

B.3 The laser diagnostic

The concentration measurements discussed in this thesis are more precisely fluorescence measurements, and may be interpreted as concentration only under certain circumstances. See, for example, the discussion in Dahm (1985). Of particular interest is that the fluorescent signal is linearly proportional to the dye concentration. Three runs at different concentrations served to show that the fluorescence was linear with dye concentration, to within 3% (less than the concentration uncertainties).

The fluorescence was not, however, linear with laser power (Fig. B.1). The measured values indicate that the fluorescence is approaching *saturation*. In other words, the dye is pumped so hard, few dye molecules remain in the ground state to fluoresce, if the incident intensity is increased yet further. This type of saturation is not to be confused with either saturation of a detector or nonlinearity of the fluorescence with dye concentration. There are a couple of advantages to operating under near-saturated conditions. One is that the signal has been maximized with

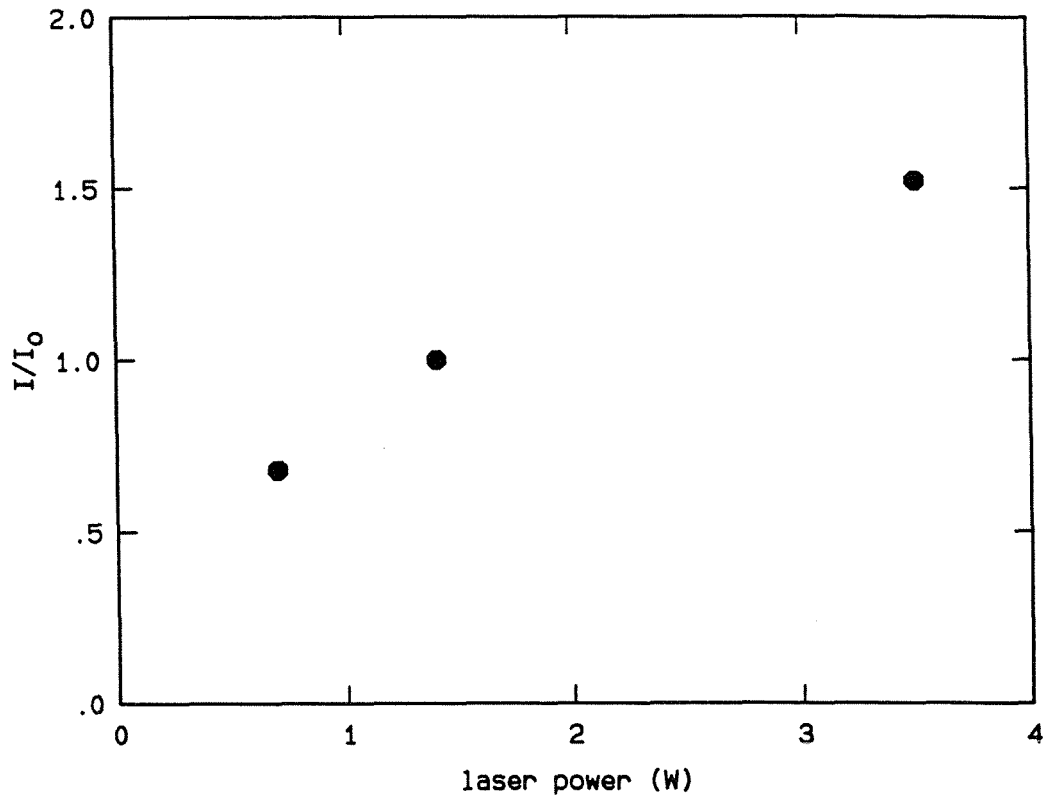


Fig. B.1 Fluorescence intensity for varying laser power. The intensity quantities are normalized by the intermediate value.

respect to the laser power; additional increases in power will increase the intensity little. A second advantage is that operating in a saturated state decouples laser power fluctuations from the measurements. The laser used was very stable (operated in light-control mode), but this decoupling serves as an additional isolation of the fluorescence from laser influences in another way. As discussed in Appendix A, an additional concern in interpreting fluorescence intensity as concentration is the attenuation of the beam in passing through a dyed region before the measuring location. If the fluorescence was fully saturated, this concern would be removed entirely, and, to the extent that Fig. B.1 demonstrates saturation, the analysis of the influence of attenuation on the measurements of c'/\bar{c} is overly conservative.

B.4 Jet alignment

The jet nozzle hole was machined normal to the flat exit plane of the nozzle plate, within typical machining accuracies (roughly a tenth of a degree). The nozzle plate was mounted to the bottom of the jet plenum assembly, and the plenum was positioned in the center of the top of the tank, supported on two beams. The nozzle was aligned to the vertical by filling the tank to a point just below the exit plane and observing the plate and its reflection on the water surface from right angles. The reflection caused the appearance of a long, narrow gap between the real nozzle plate and its reflection. As the nozzle plate was adjusted to be level by tilting the plenum on its supporting screws, the water level was brought closer, causing the gap to be even smaller. With a very small gap, it was easy to detect a variation of 1 mm, or so, across the 30 cm plate. The nozzle was therefore considered aligned to the vertical within 0.2° .

With the nozzle aligned, a length of 6 lb. fishing line was threaded through the plenum from the fill valve and out the nozzle hole, with the aid of a plastic coated wire. A weight was attached to the fishing line, and it was used as a plumb bob to indicate the geometric jet axis. Two pieces of tape were attached to the line, with their top edges separated by the desired x/d apart, and the higher tape was brought up into gentle contact with the nozzle plate. The focusing optics were then aligned so that the laser beam entered the tank at very nearly normal incidence, and intersected the fishing line. The height of the beam was iterated, until it intersected the line at the top of the lower tape. The focus was displaced about a millimeter to one side for a moment (the waist is only a fraction of a millimeter in diameter), just barely above the top edge of the tape, and the beam waist was viewed from the side with a telescope. The waist was then centered in the beam direction, using the fishing line as a reference. With the beam still slightly displaced, the focusing

optics were aligned. The image of the beam was brought into focus on the slit of the PMT, and then the image of the line was centered on the slit. Finally, the beam was moved back sideways to intersect the fishing line at the edge of the tape, making the resulting distorted beam pattern symmetric to achieve the best centering. The various alignments were checked again, and the fishing line was removed.

The general issue of resolution is discussed in Appendix C.

B.5 Signal background

Immediately before the run, data were recorded with the PMT under two conditions: with the PMT blocked, recording the dark background signal, and with the PMT recording the light from the measurement volume with the laser beam, but no jet dye, present. The dark signal provided an indication of the noise of the detection system, while the laser signal determined the lowest possible background level. The laser signal differed from the dark signal because of the presence of small amounts of fluorescent contaminants in the reservoir water, possibly oil. The amount of light at the laser frequency which made it through the cut-off filter was negligible compared to this background fluorescence contribution.

The background level was initially intended to be subtracted from the jet fluorescence signal, accounting for the background. However, it was discovered from the earliest experiments that the lowest recorded signal levels during a run never actually achieved this value, by about 1% of the run's mean. This was attributed to the fact that the background signal is primarily background fluorescence of contaminants in the water in the absence of dye, but can additionally include scattered fluorescence. When the dye is not present, the fluorescence is so weak that scattering adds little. During a run, however, there is considerable fluorescence in the

vicinity of the measuring point, and scattering may contribute. The offset used for the data was therefore determined from the lowest values measured during the run. This relies on a need that the zero concentration level is attained at some point during the run. At the lower Reynolds numbers, the characteristic upward-turned shape of the pdf at zero concentration made this a simple task. For higher Re , it was feared that no such baseline would be available, if little or no reservoir fluid reached the centerline. However, there were always a few points delineating the lower values of the pdf (sometimes only tens of points per million), that yielded zero values consistent with the values obtained from lower Reynolds number runs, under similar conditions. The data were offset using these lowest observed values, as a first order correction to a roughly 1% systematic shift of the mean.

B.6 Reynolds number calibration

In the Phase I measurements, the Reynolds number was calibrated during each run. The movement of the fluid level, visible inside the clear plenum, was timed with a stopwatch between two marks located a known distance apart. The volume flux through the nozzle could then be calculated, allowing the velocity to be determined. The first mark was sufficiently low to avoid any transients in the jet start-up. In the Phase II experiments, the plenum was not clear, and the micrometer had to be calibrated in advance. For Phase IIa, at three supply pressures and over a range of micrometer settings, the jet was started, permitted to develop, and a container was used to collect the emerging jet fluid for a fixed amount of time. Once again, the velocity was then calculated from this volume flux measurement. The resulting Reynolds numbers were plotted as a function of micrometer setting, and the points were least-squares fit with a fifth-order polynomial. The micrometer settings corresponding to desired Reynolds numbers were then estimated using this

fit.

In Phase IIb, no micrometer was used. The jet was calibrated as in Phase IIa, but at fixed initial supply pressures.

B.7 Jet start-up

At the end of the Phase IIa measurements, the jet start-up was investigated for possible oscillations. A pressure transducer with roughly a 100 Hz frequency response was plumbed into the jet driving gas supply line, both upstream and downstream of the sonic metering valve. No oscillations were observed, but it was discovered that the pressure rise downstream of the micrometer, and therefore the jet start-up, was slower than previously suspected. It was decided to remove the micrometer altogether, and the driving system was converted into a blow-down configuration. Two type A gas cylinders were used as a supply manifold, and were connected to the plenum through a gas-actuated valve. The resulting improvement is shown in Fig. B.2.

The square-root of the pressure trace is included for the micrometer case, since, as can be seen from Bernoulli's equation, $u_0 \propto p(t)^{1/2}$. The micrometer configuration, it is seen, took a significant time to attain a fixed percentage of the final pressure, while the no-micrometer case was very close to ideal. For the micrometer case shown, the time to attain 95% of the final pressure was about 8% of the total run time. It is estimated that the Phase IIa runs varied in Reynolds number by about 5% over the majority of the run.

This velocity variation did not influence the results, since the statistics typically depend logarithmically on Reynolds number. Nevertheless, the Phase IIb measure-

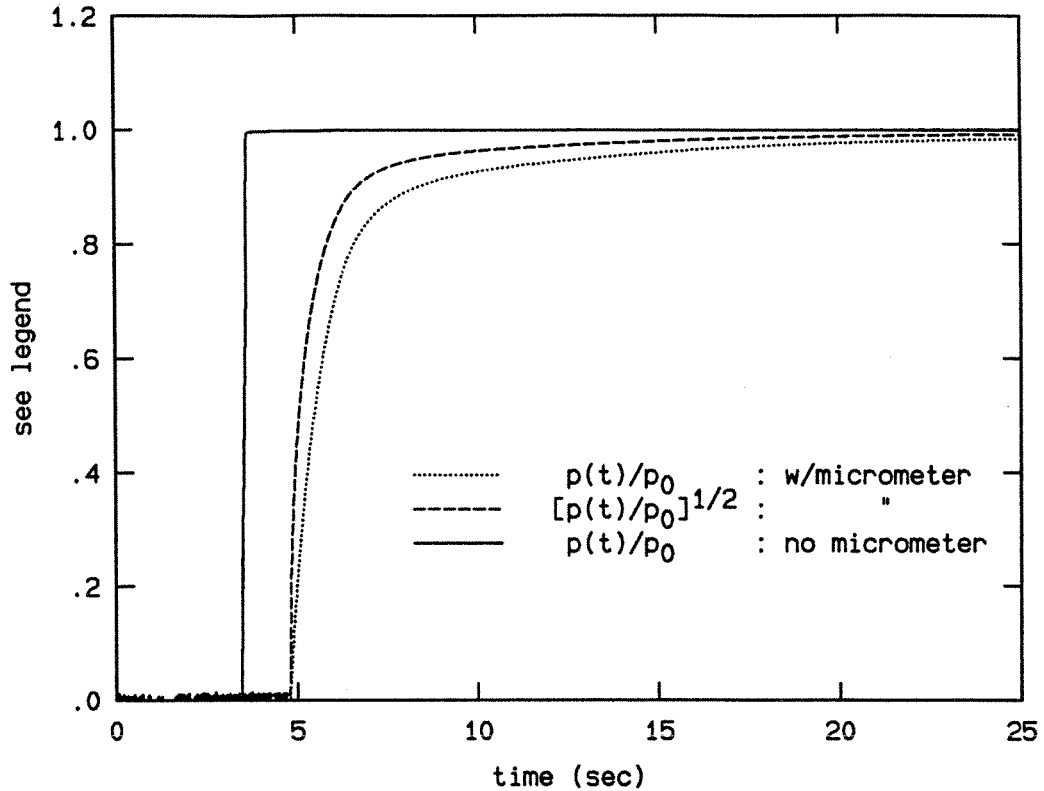


Fig. B.2 Jet plenum pressure histories, with and without micrometer. $Re \sim 50,000$. Pressure nondimensionalized by maximum of run. The two cases start at arbitrary times. Noise before start is accentuated by the square root.

ments were all conducted with the blow-down configuration, partly because there was some concern over whether the time profile of the velocity during start-up could perhaps be influencing the jet behavior. However, a new restriction was encountered with the blow-down supply, because the manifold pressure dropped over the course of the run, causing a velocity decay (rather than a velocity increase). The effect was greatest at the lowest Re , amounting to about a 10% decline at $Re = 12,500$, 7% at 17,600, and so on, down to about 2% at 102,000. These variations were accepted in favor of a close-to-ideal start-up.

Evidence to support the claim of velocity insensitivity is included in Fig. C.1

below. There, (compensated) power spectra are shown for $x/d = 100$, Phase IIa measurements, in which the jet had a slow start-up (as in Fig. B.2) and was slightly accelerating throughout the run, and $x/d = 305$, Phase IIb measurements, with a fast start-up and small deceleration during the run. The collapse of the different cases is noteworthy. It is concluded that neither the start-up variations (examined here) nor the velocity variations produced a significant change in the measured statistics of the scalar field.

B.8 Signal acquisition

Runs began by opening the solenoid on the plenum gas supply line, initiating the jet flow. The jet development was monitored visually, and when it had developed to a point at least one or two local jet diameters past the measuring station, data acquisition was started. Records were routinely checked for behavior (e.g., a systematic trend in the mean) which might indicate contamination of the run from proximity to the jet head, and none was found.

For the Phase I measurements, a 12-bit A/D board was used, as mentioned in Chapter 2, and the data were stored in memory as they were collected. At the time, this limited the number of data points per run to slightly over 1 million. The Phase II measurements, except those at $x/d = 170$, utilized a 16-bit A/D board, and the data were written directly to disk. This placed a limitation on the data acquisition frequency of 50 kHz, but removed any storage limitations on the run record lengths. Records of over 8 million points were acquired in this manner. For the $x/d = 170$ runs, a 12-bit board was once again used (writing to memory) for its capability to operate up to 100 kHz. With twice as much memory as before, about 2 million points were recorded.

B.9 A/D converter calibration

In the Phase I measurements, the data were corrected for A/D converter bin size irregularities by calibrating the converter (see also Dowling, Sec. E.3). A signal generator was used to provide an accurate triangle wave signal which spanned the voltage range of the A/D board, at a frequency that was low in comparison to the data acquisition frequency. A data record consisting of an integral number of cycles from the triangle wave was collected after each jet run, of sufficient length to assure that each A/D integer value was realized over 100 times. A pdf was constructed from the resulting values. The normalized heights of each pdf bin represented the actual A/D bin widths. A look-up table was generated from this information and used to correct the nonuniformities. This correction involves conversion of the integer values produced by the A/D converter to real numbers, and during this process, each datum point was randomly assigned to a value within its proper bin.

The calibration procedure was considered unnecessary for the Phase II measurements, and was not utilized.

B.10 Noise and Wiener filtering

By conducting runs with different dye concentrations and the same amplification settings, and also with different amplifications but the same dye concentration, it was determined that the noise floor of the spectra resulted from the first (transimpedance) stage of amplification. The noise characteristics of the same photomultiplier detection system used in these experiments are discussed in Dowling, et al. (1989).

Careful consideration has been given to the reduction of noise in these mea-

surements. As has been described elsewhere (Dowling 1988, Dowling, et al. 1989, and Miller & Dimotakis 1991a), Wiener filter techniques (Wiener 1949, and Press, et al., 1986) were used in processing the data. Given the power spectrum of a noisy signal and the power spectrum of the noise in the absence of the signal, the Wiener filter recovers the noise-free signal by minimizing the expected mean-squared error between the filtered signal and the “true” noise-free signal. In practice, this is done by subtracting a model noise spectrum from the data power spectrum, and computing the inverse Fourier transform of the result. This yields a filter kernel in the time domain, which is convolved with the data to obtain the noise-free approximation. A demonstration of the effectiveness of the Wiener filter is shown in Fig. B.3, in which the unfiltered (raw) spectrum and the Wiener-filtered spectrum are compared.

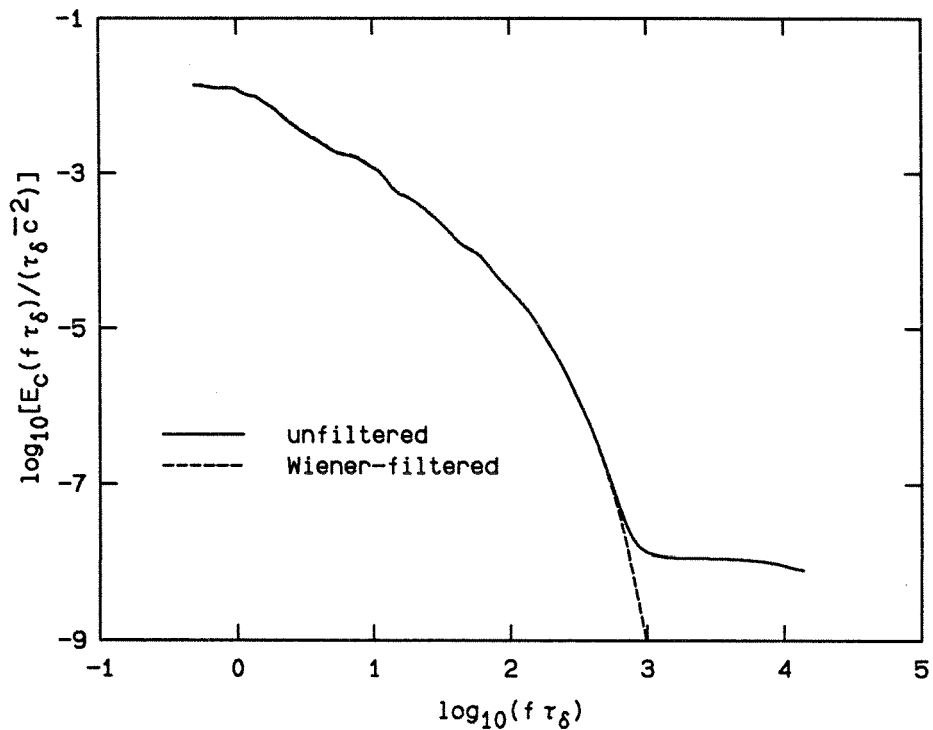


Fig. B.3 Demonstration of Wiener filter. Phase I data: $Re = 2940$, $x/d = 100$.

B.11 Power spectral density estimation

All of the power spectra used in this thesis were computed using a power spectral density program developed by Paul Dimotakis over the past ten years, or so, named PSD. The program computes power spectra of data files by means of FFT methods, and incorporates Hanning windowing, contiguous record overlapping, and parabolic detrending, among other features. Records of up to 2^{17} points can be accommodated. Straight-line fits to the spectra are possible, between selected frequency limits. This option was used to determine the average spectral slopes and the inertial range slopes of Chapter 5. The program also provides third-octave ($\simeq 1/10$ decade) filtering to smooth the computed spectra, yielding 20 points per decade in the smoothed curves. This feature was used for all the spectra in this thesis, not as much for smoothing purposes, but to reduce the number of points to a manageable level for plotting (note that $2^{16} = 65536$). The smoothed spectra were later differentiated using centered three-point differencing, to produce the spectral slope curves.

APPENDIX C

Microscales and resolution

This appendix discusses some of the various fluid-dynamical microscales and estimates their sizes for these high Schmidt number turbulent jets. The issue of resolution is then addressed, starting with a description of the three types: spatial, temporal, and signal-to-noise ratio (SNR). Experimental results are used to determine the resolution limits of these experiments. A method to compensate for spatial resolution limitations is described and implemented. The spatial resolution of these measurements is typically $100\ \mu\text{m}$ or better after compensation, and the SNR is determined to be the limiting factor of resolution for most of the data. Some discussion of whether particular findings are sensitive or insensitive to resolution is included. In conclusion, some observations regarding the smallest scales and the continuum approximation are made.

The issue of resolution for these measurements was previously discussed in Miller & Dimotakis (1991a,b), where some of the following discussion first appeared.

C.1 Description of microscales

Before describing the resolution of these measurements, an overview of the fluid-dynamical scales of interest is in order.

Following G. I. Taylor (1935), the total mean kinetic energy dissipation rate ε of a (large Re) turbulent flow must scale with the inviscid parameters of the flow, i.e., the flow large scale δ and velocity difference ΔU , so that

$$\varepsilon = \frac{(\Delta U)^2}{\delta/\Delta U}. \quad (\text{C.1})$$

Kolmogorov (1941) suggested this relation could be extended, for *isotropic and homogeneous* flow, to scales smaller than δ but larger than the scale at which the associated Reynolds number,

$$Re_\lambda = \frac{u_\lambda \lambda}{\nu} \approx 1. \quad (\text{C.2})$$

Eqs. C.1 and C.2 yield the Kolmogorov length scale λ_K ,

$$\lambda_K \equiv \left(\frac{\nu^3}{\varepsilon} \right)^{\frac{1}{4}}. \quad (\text{C.3})$$

The Kolmogorov scale is thus a scale associated with the smallest velocity fluctuations in the flow, assuming the flow is homogeneous and isotropic, and ignoring variation in the dissipation rate.

Using the result of Friehe et al. (1971) for the kinetic energy dissipation rate ε on the centerline of a turbulent jet (cf. Dowling & Dimotakis 1990), i.e.,

$$\varepsilon = 48 \frac{u_0^3}{d} \left(\frac{x - x_0}{d} \right)^{-4}, \quad (\text{C.4})$$

the Kolmogorov scales for these measurements,

$$\lambda_K = 0.38(x - x_0) Re^{-3/4}, \quad (\text{C.5})$$

are found to range from roughly $17 \mu\text{m}$ to about 0.7 mm . Note the dependence of λ_K on x (neglecting the small virtual origin x_0 of these measurements). It implies that an increase in resolution (relative to the fluid-dynamical scales) is achieved by moving farther from the jet exit.

By similarity arguments, the velocity field spatial scale where the action of viscosity will become important, say, λ_ν , will be some multiple of λ_K . Normalized energy spectra are found to break from a constant power-law at a wavenumber k_ν such that $k_\nu \lambda_K \approx 1/8$ (e.g. Chapman 1979). This yields an estimate of (cf. Miller & Dimotakis 1991b)

$$\lambda_\nu = \frac{\pi}{k_\nu} \sim 25 \lambda_K , \quad (\text{C.6})$$

i.e., to resolve the roll-off of the *velocity* spectrum, a scale ~ 25 times λ_K needs to be resolved.

While the Kolmogorov scale represents the smallest *velocity* scale in the flow, the smallest expected *scalar* diffusion scale λ_B is smaller yet by a factor of $Sc^{1/2}$ (Batchelor 1959), i.e.,

$$\lambda_B \equiv \frac{\lambda_K}{\sqrt{Sc}} . \quad (\text{C.7})$$

Adopting the diffusion coefficient for fluorescein reported in Ware, et al. (1983), of $5.2 \times 10^{-6} \text{ cm}^2/\text{sec}$, the calculated Schmidt number for dilute fluorescein in water is slightly less than 1900. This implies a scalar diffusion scale

$$\lambda_D \sim 25 \lambda_B \quad (\text{C.8})$$

that is roughly $25/43$, or 0.58 , times the Kolmogorov scale.

Finally, a third scale, the Taylor microscale λ_T , is also significant. The Taylor scale is of interest in the jet because it is analogous to an “internal boundary layer” in its scaling, as pointed out by Philip Saffman. The entrainment process in the jet

involves engulfment of tongues of fluid near the rear of the large-scale structures, and it appears these incursions scale like Taylor-scaling (Miller & Dimotakis 1990).

The Taylor scale can be calculated from its definition,

$$\lambda_T = \sqrt{\frac{15\nu}{\varepsilon}} u'_1, \quad (\text{C.9})$$

where u'_1 is the rms of (one component of) the velocity. Once again, using Eq. C.1 for ε and Eq. A.2 for u_{cl} , assuming a jet full angle of 23° , and $u'_1/u_{cl} \approx 0.25$ (cf. Wygnanski & Fiedler 1969), the relation

$$\lambda_T \approx 2\delta Re^{-1/2}, \quad (\text{C.10})$$

is obtained for the turbulent jet. Similarly, an expression for the jet Taylor Reynolds number,

$$Re_T \approx 1.4 Re^{1/2}, \quad (\text{C.11})$$

can be derived.

C.2 Resolution

There are three resolution requirements on these measurements: spatial, temporal, and signal-to-noise ratio (SNR). Close to the nozzle exit (i.e., $x/d = 100$), spatial resolution was the more restrictive of the three, and was primarily determined by the dimensions of the laser beam (its diameter) in two dimensions, and the width of the slit on the PMT in the third dimension. It is important to note that, for any measurements conducted at the same x/d (and same Phase of the experiment), any fixed resolution scale is *independent of* Re when passage times are non-dimensionalized by τ_δ .

The temporal resolution of the measurements was determined by the data acquisition rate, which was always more than twice the frequency of the Butterworth filter. If a spectrum is temporally resolution limited, its shape is unaffected, but the high-frequency end is truncated. The SNR resolution was limited by the noise floor of the electronics. For the smallest x/d , highest Re cases, the resolution limit was temporal (because the data acquisition rate was constrained when writing to disk), while after compensation for spatial resolution limitations (described below), the other runs were generally SNR resolution limited.

As detailed in Appendix B, the visual width of the laser beam waist was measured with a cathetometer. In Phase I, the measured diameter was about $80\ \mu\text{m}$, and in Phase IIa, $60\ \mu\text{m}$, decreasing to about $40\ \mu\text{m}$ in Phase IIb. It was desired to somehow estimate the resolution of the measurements in the presence of the jet, with the correct dye concentration present in the sampling volume. The addition of the dye can affect the index of refraction of the water, particularly at higher concentrations. Since an index gradient can bend the beam, altering the beam propagation, this would tend to smear the focus of the beam and alter the focal point location. To address these concerns, two runs were conducted under identical circumstances, but with dye concentrations that differed by a factor of four. The power spectra of the two concentration records were examined, and no discernable difference was found. It is concluded that the dilute dye concentrations used had no significant influence on the laser beam propagation.

The spatial resolution was examined by changing the width of the slit in front of the PMT by a factor of two. There was a definite change in the spectra; the spectrum using the smaller slit extended just a bit further than the other at high frequency. That is the behavior expected if the measurement is spatial-resolution limited, the resolution limit acting as a single-pole filter. Having *two* of these measurements,

however, allows the poles locations to be determined, and their effects compensated for, in the following way (suggested by Paul Dimotakis).

The two runs were conducted under the same conditions, and it is assumed that their “true,” spatially resolved spectra $E(\omega)$ are the same, but that the measured spectra $E_{\text{meas}}(\omega)$ have different spatial resolutions. The effect of a spatial resolution limitation is to multiply the true spectrum with a single-pole filter, whose transfer function $|H(\omega)|^2$ is

$$|H(\omega)|^2 = \frac{1}{1 + (\omega\tau)^2} , \quad (\text{C.12})$$

where τ is the pole location. This yields the measured spectrum E_{meas} , i.e.,

$$E_{\text{meas}}(\omega) \equiv |H(\omega)|^2 E(\omega) . \quad (\text{C.13})$$

One of the measured spectra is presumed to be affected by a single pole filter located at τ_1 , the other by a pole located at τ_2 . Dividing the two spectra, the result

$$\frac{|H_1(\omega)|^2}{|H_2(\omega)|^2} = \frac{1 + (\omega\tau_2)^2}{1 + (\omega\tau_1)^2} , \quad (\text{C.14})$$

is obtained. The measured spectra were divided in this manner and a fit was made to Eq. C.14 to determine the pole locations τ_1 and τ_2 . The power spectra were then compensated, by dividing them by their respective estimated filter transfer functions. The final result is demonstrated in Fig. C.1. Compensated and un-compensated spectra of both slit sizes are shown, with an $x/d = 305$ spectrum for comparison. Recall that the farther x/d locations have larger fluid-dynamical scales, making the relative resolution proportionately better. The near-perfect agreement between the compensated $x/d = 100$ spectra and the $x/d = 305$ spectrum, to almost $\log_{10}(f\tau_\delta) = 3.0$, is noteworthy.

The equivalent scales of the pole locations at $x/d = 100$ are $100 \mu\text{m}$ and $67 \mu\text{m}$, comparable to the estimated diameter of the laser beam. The same procedure was

used to correct the spatial resolution of the Phase IIa, $x/d = 305$ spectra, using two runs with different slits at that location. The poles at $x/d = 305$ were determined to be about $39 \mu\text{m}$ and $25 \mu\text{m}$. The values smaller than the waist diameter at 305 reflect the fact that that spatial resolution is not the primary limitation of resolution for those spectra, but rather, the SNR is. From the spectral slope results of Chapter 5, it is shown that the spectra of the $x/d = 305$ runs are unaffected by resolution until $\log_{10}(f\tau_\delta) \approx 2.8$, and the $x/d = 100$ runs until $\log_{10}(f\tau_\delta) \approx 2.6$. The Phase IIb, $x/d = 170$ and 295, and Phase I runs did not include both slits, so the compensation was not possible directly, and was not attempted by other means.

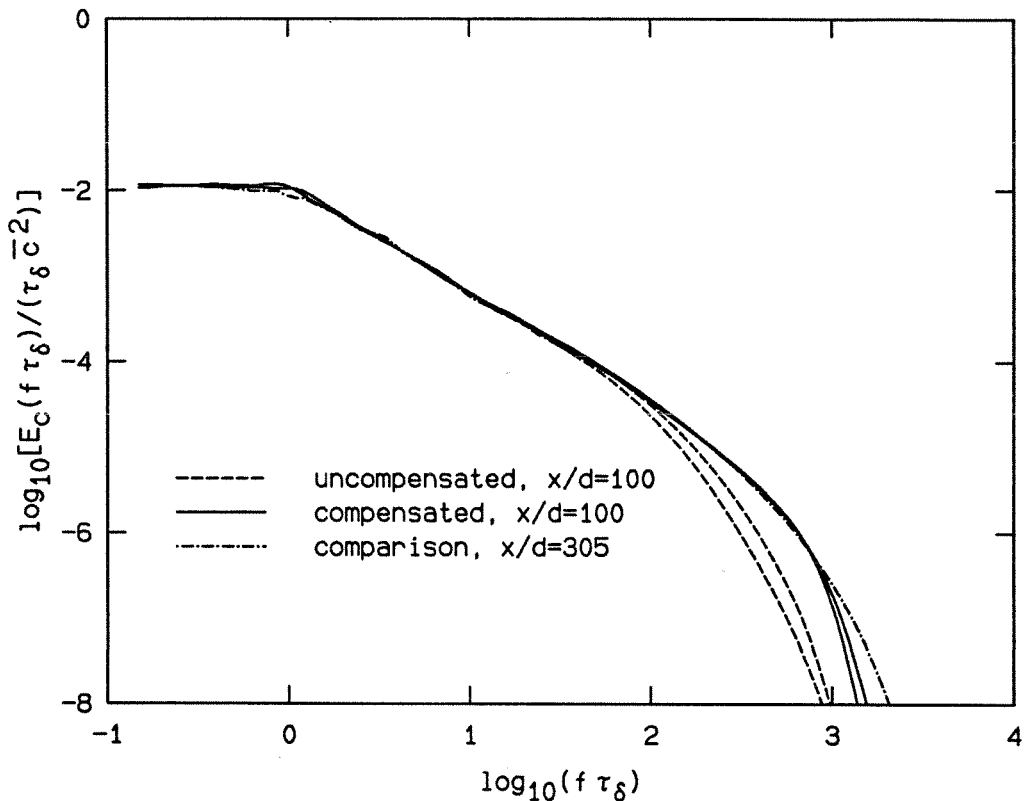


Fig. C.1 The two spectra used to calculate the poles at $x/d = 100$ and $Re = 12,500$, with a similar run at $x/d = 305$ ($Re = 12,000$) for comparison.

To summarize, direct measurements of the laser beam diameters, in combina-

tion with calculations of the spatial resolution poles from the data, indicate that the effective spatial resolution of these measurements is about 100 to 40 μm , *before* compensation. After compensation, the spatial resolution was no longer the primary resolution limitation. With the exception of the fastest $x/d = 100$ Reynolds numbers (for which temporal resolution was limiting), SNR resolution became the constraint. The spectra are considered resolved until at least 2.6 to 2.8 in $\log_{10}(f\tau_\delta)$ units.

C.3 The extent of resolution's influence

Many of the quantities considered in this thesis are insensitive to the effects of resolution. The mean concentration is certainly unaffected, along with any relatively large-scale features (basically any spectral information which is not located at the highest frequencies). Virtually all of the analysis of Chapter 3 falls under this category.

Also insensitive are integral measures, such as the average spectral slopes and the total scalar variance. An analysis of the sensitivity of the variance to resolution appears in Miller & Dimotakis (1991b). They found that the variance is relatively *insensitive* to resolution. The jet spectrum, as shown in Chapter 4, steepens as the Reynolds number increases, which causes the bulk of the contribution of the variance to occur near the large scales (cf. also Chapter 3). This conclusion also implies that the jet concentration pdf's are somewhat insensitive to resolution, since the second moment of the pdf yields the variance. While the variance does not determine the pdf shape, it is a constraint.

Basically, the only quantities examined in this thesis which are sensitive to resolution are those that emphasize the smallest scales of the flow. The spectra

used for these purposes were treated very carefully, using runs which were free of any quirks (as detected by any of the diagnostic quantities examined), compensating independently to correct any spatial resolution filtering which may have been present, and then checking for consistency. The location of the spectral roll-off is the most sensitive feature to the effects of low-pass filtering. At $Re = 3,000$, the calculated Kolmogorov scale is 0.73 millimeters, and the corresponding Batchelor scale, about $17 \mu\text{m}$. If the spectral roll-off of the Batchelor scale is expected at $\lambda_{\mathcal{D}}$, it is necessary to resolve $\log_{10}(f\tau_{\delta}) \approx 2.9$ to observe it. Since this is just on the borderline of the measurement's resolution, the run provides virtually fully-resolved data, down to $\lambda_{\mathcal{D}}$.

C.4 A comment on the continuum approximation

We are accustomed, particularly in the case of simple subsonic, atmospheric pressure flows, to think of the continuum approximation as a sound one. However, consider the following. The limit found for establishment of specific similarity in the jet with axial location (e.g., Dowling & Dimotakis 1990, and Dowling 1988) is approximately $x/d = 20$. Under the highest Reynolds number conducted in the course of these experiments, the calculated Kolmogorov scale, at $x/d = 20$, is $3.4 \mu\text{m}$, and the Batchelor scale, 770 \AA ! This is only a factor of 200 larger than the inter-molecular spacing of water, and roughly a factor of 20, or so, larger than the molecular dimensions of the fluorescein molecule used as the passive scalar. It would not be surprising to expect the influence of this bound to be felt at least a decade larger in size, suggesting that these microscales, as estimated from Eqs. C.5 and C.7, have the potential to feel the influence of the discreteness of molecules.

It should be noted that the current Schmidt number of approximately 1900,

and the maximum Reynolds number of 102,000, are by no means limiting values for these parameters in achievable flows. Also, the nozzle diameter can be reduced, reducing the large scale dimensions at $x/d = 20$ and further decreasing these scales in proportion. Even if the current diameter is retained, the Batchelor scale attains a value of 50 \AA , comparable to the fluorescein size, at a Reynolds number of 1.5×10^6 . While there are practical difficulties in generating this flow in the laboratory, it is not prohibited on principle.

APPENDIX D

Jet growth rate pictures

A separate experimental set-up was used to acquire shadowgraphic images of the jet to measure its growth rate. A cold water-alcohol mixture (typically 0-5° C) was used for the jet fluid. The addition of an appropriate amount of alcohol to the cold water permitted the jet fluid density to be very closely matched to the density of the room-temperature reservoir fluid while maintaining the difference in the indices of refraction which produces the shadowgraph effect. The experimental configuration used is shown in Fig. D.1. An Oriel white-light source was used that consisted of a small 100 W bulb (in front of a parabolic reflector) and a collimating lens. The lens was adjusted so the illumination from the lamp was slowly diverging. A large mirror increased the light path by folding it into the available space, decreasing the required divergence of the light to illuminate the full jet. The light passed through the tank's large glass windows, and the resulting shadowgraph image was projected onto a large rear-projection screen. High-speed Kodak TMax black-and-white film was used with small f-stop settings to freeze most of the flow-field image.

This arrangement worked quite well, clearly visualizing the jet, with one difficulty. The size of the area to be imaged did not permit the use of a collimated light source, and the diverging light had to be used. This caused a bright region to appear in the jet image at the location corresponding to looking directly at the source. While the eye could make adjustments for this nonuniformity when viewing the image in real-time, the variation prevented adequate photography under the

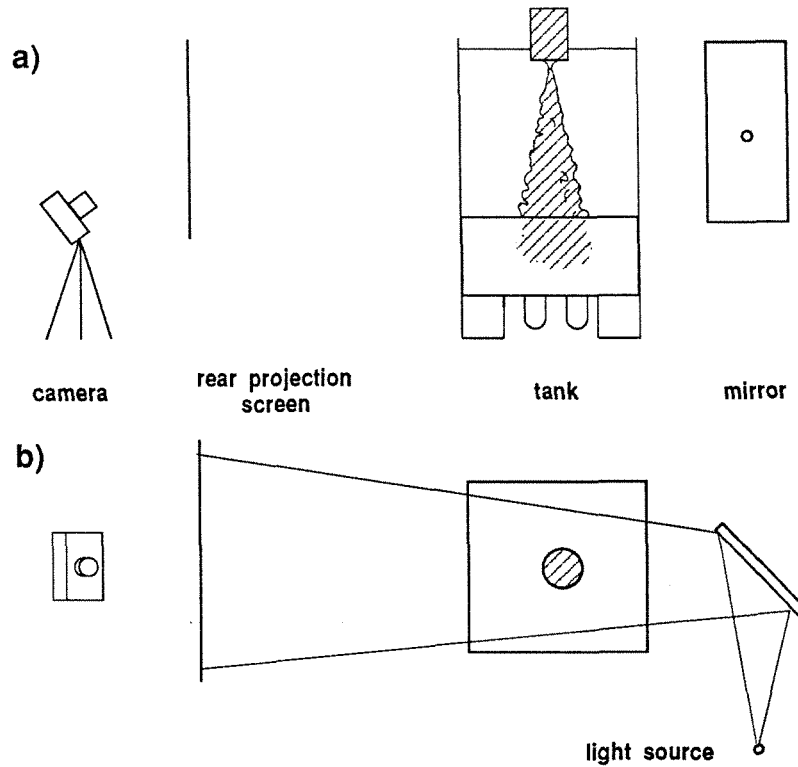


Fig. D.1 Shadowgraph set-up: a) Side view, b) Top view.

low-light conditions. The solution used was to photograph the screen at an angle, from a location which put the line-of-sight to the light source off the screen. This introduced two new difficulties. Since the variation in illumination was roughly circular (centered on the light source), if viewed at a sufficient angle, it appeared as an almost uniform gradient across the screen. In addition, the angle of the photography introduced distortion to the pictures, the “keystone effect,” from the perspective of viewing the rear-projection screen at an angle.

While it might at first seem that one problem was traded for two, the two new difficulties could both be addressed in the photographic printing process. To remove the keystone effect, the photographic paper was mounted on an inclined table at the correct angle to reverse the original distortion. The intensity variations, since

they appeared as an almost linear gradient, were dodged (printed by blocking some of the image) to equalize the illumination quite well on the resulting prints. This custom printing was performed by Harry Hamaguchi of GALCIT.

Shadowgraphy was selected for the jet imaging because of several advantages it holds over laser-induced fluorescence in this application. If LIF was utilized for this task, the options would include either planar or flood illumination, and either a frozen image or a long-time exposure. Since these photographs were intended to determine the growth rate of the jet, which involves locating its edge (some suitably defined boundary), we recognized that planar imaging would not provide as good an indication (because of local fluctuations) as an integrated side view image. In particular, the shadowgraphy is particularly sensitive to normal gradients, precisely what occurs at the edge of the jet when imaged from the side, and less sensitive to parallel gradients, such as when viewing the jet through its axis. A long-time exposure using PLIF would emphasize the center of the jet because of the jet concentration profile, which resembles a Gaussian in the mean. It would also measure a different quantity if the instantaneous and time-averaged extent of the jet were different (from some unsteady behavior, for instance). Because the strongest shadowgraphy signals are produced by very localized gradients, the shadowgraph exposures were kept short to avoid washing out such features and also to freeze the majority of the jet's image. Flood-illuminated LIF would suffer from low fluorescence (because of the three-dimensional laser beam expansion required) and has even stronger relative intensity at the jet center and lower at the edge than PLIF because of the projection of the jet cone. For these reasons, time-resolved shadowgraphy was chosen for the jet growth rate pictures.

A sample shadowgraph photograph of a Phase I, $Re \approx 21,000$ jet is included as Fig. D.2. The tip of the nozzle extension can just barely be seen at the top of

the picture.

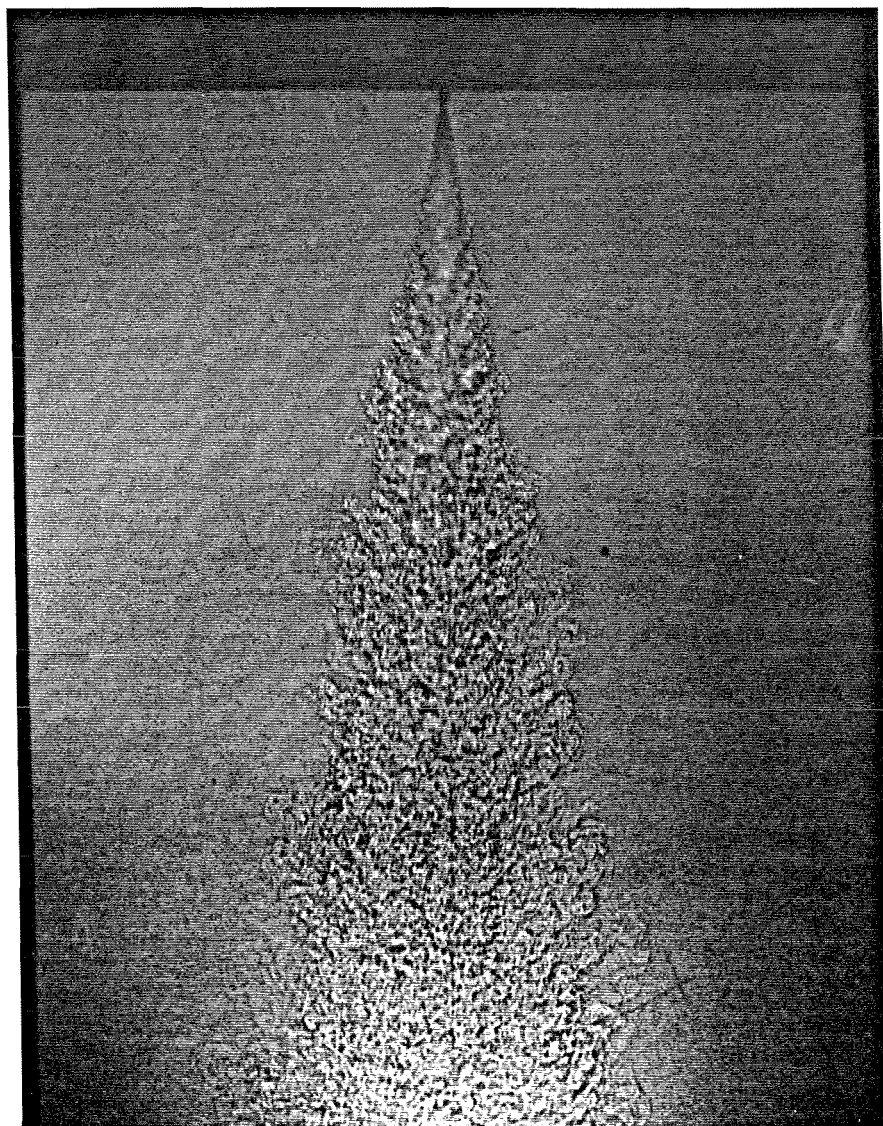


Fig. D.2 Shadowgraphic image of the (Phase I) jet. $Re \approx 21,000$. The nozzle is at top, and the flow is from top to bottom. The picture includes approximately $0 < x/d < 200$.

The geometry of the jet boundaries was determined with the aid of a computer program. The picture was taped to a digitizing pad and reference points were read off the photo, establishing the coordinates. A clear, straight-edged piece of transparent material was used to locate one edge of the jet. Five positions along this straight edge were then digitized. The process was repeated for the other side of the jet, and the resulting values were written into a file. The file was read by a program that fit straight lines to each set of five points, and calculated the jet full angle α , inclination, and virtual origin. No significant jet inclination was found. The virtual origin was less than a couple of nozzle diameters, and the jet full width was about 23° in most cases. This value was used to calculate $\delta(x)$, the local jet width, from the relation

$$\delta(x) \equiv 2x \tan(\alpha/2) \approx 0.407x . \quad (\text{D.1})$$

The resulting values were used throughout this thesis.

References

- BATCHELOR, G. K. [1959] "Small-scale variation of convected quantities like temperature in turbulent fluid. Part 1. General discussion and the case of small conductivity," *J. Fluid Mech.* **5**, 113–133.
- BROADWELL, J. E. [1982] "A Model of Turbulent Diffusion Flames and Nitric Oxide Generation. Part I," TRW Document No. 38515-6001-UT-00, EERC Final Report, PO No. 18889.
- BROADWELL, J. E. [1987] "A Model for Reactions in Turbulent Jets: Effects of Reynolds, Schmidt, and Damköhler Numbers," US-France Workshop on Turbulent Reactive Flows (Rouen, France), 7–10 July 1987. Published: *Turbulent Reactive Flows*, (eds. R. Borghi and S. N. B. Murthy, *Lecture Notes in Engineering* **40**, Springer-Verlag New York Inc., 1989), 257–277.
- BROADWELL, J. E. and BREIDENTHAL, R. E. [1982] "A simple model of mixing and chemical reaction in a turbulent shear layer," *J. Fluid Mech.* **125**, 397–410.
- BROADWELL, J. E. and MUNGAL, M. G. [1991] "Large-scale structures and molecular mixing," *Phys. Fluids A* **3**(5), 1193–1206.
- CHAPMAN, D. R. [1979] "Computational Aerodynamics Development and Outlook," *AIAA J.* **17**(12), 1293–1313.
- CHEN, C. J. and RODI, W. [1980] *Vertical Turbulent Buoyant Jets. A Review of*

Experimental Data (Pergammon Press, Oxford).

DAHM, W. J. A. [1985] *Experiments on Entrainment, Mixing and Chemical Reactions in Turbulent Jets at Large Schmidt Numbers*, Ph.D. thesis, California Institute of Technology.

DAHM, W. J. A. and DIMOTAKIS, P. E. [1985] "Measurements of Entrainment and Mixing in Turbulent Jets," *AIAA 23rd Aerospace Sciences Meeting*, 14-17 January 1985 (Reno, Nevada), AIAA-85-0056, *AIAA J.* **25**(9), 1216-1223 (1987).

DAHM, W. J. A. and DIMOTAKIS, P. E. [1990] "Large Schmidt number mixing of a conserved scalar in the self-similar far field of turbulent jets," *J. Fluid Mech.* **217**, 299-330.

DAHM, W. J. A., DIMOTAKIS, P. E. and BROADWELL, J. E. [1984] "Non-premixed turbulent jet flames," *AIAA 22nd Aerospace Sciences Meeting* (Reno, Nevada), AIAA Paper No. 84-0369.

DIMOTAKIS, P. E. [1987] "Turbulent shear layer mixing with fast chemical reactions," US-France Workshop on Turbulent Reactive Flows (Rouen, France), 7-10 July 1987. Published: *Turbulent Reactive Flows*, (eds. R. Borghi and S. N. B. Murthy, *Lecture Notes in Engineering* **40**, Springer-Verlag New York Inc., 1989), 417-485.

DIMOTAKIS, P. E. and MILLER, P. L. [1990] "Some consequences of the boundedness of scalar fluctuations," *Phys. Fluids A* **2**(11), 1919-1920.

DIMOTAKIS, P. E., MIAKE-LYE, R. C. and PAPANTONIOU, D. A. [1983] "Structure and Dynamics of Round Turbulent Jets," *Fluid Dynamics Trans.*, **11**, 47-76.

DOWLING, D. R. [1988] *Mixing in Gas Phase Turbulent Jets*, Ph.D. thesis, California Institute of Technology.

DOWLING, D. R. and DIMOTAKIS, P. E. [1990] "Similarity of the concentration field of gas-phase turbulent jets," *J. Fluid Mech.* **218**, 109.

DOWLING, D. R., LANG, D. B. and DIMOTAKIS, P. E. [1989] "An Improved Laser-Rayleigh Scattering Photodetection System," *Exp. in Fluids* **7**(7), 435-440.

FISCHER, H. B., LIST, E. J., KOH, R. C. Y., IMBERGER, J. and BROOKS, N. H. [1979] *Mixing in Inland and Coastal Waters* (Academic Press).

FRIEHE, C. A., VAN ATTA, C. W. and GIBSON, C. H. [1971] "Jet turbulence: Dissipation rate measurements and correlations," AGARD *Turbulent Shear Flows* CP-93, 18.1-7.

HOTTEL, H. C. [1952] "Burning in Laminar and Turbulent Fuel Jets," 4th (International) Symposium on Combustion (Williams and Wilkins, Baltimore, 1953), 97-113.

KERSTEIN, A. R. [1990] "Linear-eddy modelling of turbulent transport. Part 3. Mixing and differential molecular diffusion in round jets," *J. Fluid Mech.* **216**, 411-435.

KOLMOGOROV, A. N. [1941] "Local Structure of Turbulence in an Incompressible Viscous Fluid at Very High Reynolds Numbers," *Dokl. Akad. Nauk SSSR* **30**, 299. Reprinted in: *Usp. Fiz. Nauk* **93**, 476-481 (1967). Translated into English in: *Sov. Phys. Usp.* **10**(6), 734-736 (1968).

- KOOCHESFAHANI, M. M. and DIMOTAKIS, P. E. [1986] "Mixing and chemical reactions in a turbulent liquid mixing layer," *J. Fluid Mech.* **170**, 83–112.
- KRISTMANSON, D. and DANKWERTS, P. V. [1961] "Studies in Turbulent Mixing — I. Dilution of a Jet," *Chem. Eng. Sci.* **16**, 267–277.
- MILLER, P. L. and DIMOTAKIS, P. E. [1990] "Taylor-scale Features in the Turbulent Jet," *Bull. Am. Phys. Soc.* **35**(10), 2302.
- MILLER, P. L. and DIMOTAKIS, P. E. [1991a] "Stochastic geometric properties of scalar interfaces in turbulent jets," *Phys. Fluids A* **3**(1), 168–177.
- MILLER, P. L. and DIMOTAKIS, P. E. [1991b] "Reynolds number dependence of scalar fluctuations in a high Schmidt number turbulent jet," *Phys. Fluids A* **3**(5), 1156–1163.
- MONIN, A. S. and YAGLOM, A. M. [1975] *Statistical Fluid Mechanics: Mechanics of Turbulence II* (Ed. J. Lumley, MIT Press).
- MORSE, P. M. [1969] *Thermal Physics* (Benjamin/Cummings).
- MUNGAL, M. G. and DIMOTAKIS, P. E. [1984] "Mixing and combustion with low heat release in a turbulent mixing layer," *J. Fluid Mech.* **148**, 349–382.
- PAPANICOLAOU, P. N. and LIST, E. J. [1987] "Statistical and Spectral Properties of the Tracer Concentration in Round Buoyant Jets," *Int. J. Heat Mass Transfer* **30**(10), 2059–2071.
- PAPANICOLAOU, P. N. and LIST, E. J. [1988] "Investigations of round turbulent buoyant jets," *J. Fluid Mech.* **195**, 341–391.

- PAPOULIS, A. [1984] *Probability, Statistics and Stochastic Processes* (2nd ed., McGraw-Hill).
- PARSONS, R. [1959] *Handbook of Electrochemical Constants* (Butterworths Scientific Publications, London).
- PRESS, W. H., FLANNERY, B. P., TEUKOLSKY, A. A. and VETTERLING, W. T. [1986] *Numerical Recipes. The Art of Scientific Computing*. (Cambridge Univ. Press).
- RICOU, F. P. and SPALDING, D. B. [1961] "Measurements of entrainment by axisymmetrical turbulent jets," *J. Fluid Mech.* **11**, 21–32.
- TAYLOR, G. I. [1935] "Statistical theory of turbulence," *Proc. Roy. Soc.* **A151**, 421.
- WARE, B. R., CYR, D., GORTI, S. and LANNI, F. [1983] In: *Measurement of Suspended Particles by Quasi-elastic Light Scattering* (Wiley, New York, pp. 255–289).
- WEDDELL, D. [1941] *Turbulent Mixing in Gas Flames*, Ph.D. thesis, Massachusetts Institute of Technology.
- WIENER, N. [1949] *Extrapolation, Interpolation and Smoothing of Stationary Time Series* (Wiley, New York).
- WILSON, R. A. M. and DANKWERTS, P. V. [1964] "Studies in Turbulent Mixing – II. A Hot-Air Jet," *Chem. Eng. Sci.* **19**, 885–895.

WYGNANSKI, I. and FIEDLER, H. E. [1969] "Some measurements in the self-preserving jet," *J. Fluid Mech.* **38**, 577-612.